

THEORETICAL INVESTIGATIONS OF TERASCALE PHYSICS

by

WEI GONG

A DISSERTATION

Presented to the Department of Physics
and the Graduate School of the University of Oregon
in partial fulfillment of the requirements
for the degree of
Doctor of Philosophy

September 2009

University of Oregon Graduate School

Confirmation of Approval and Acceptance of Dissertation prepared by:

Wei Gong

Title:

"Theoretical Investigations of Terascale Physics"

This dissertation has been accepted and approved in partial fulfillment of the requirements for the Doctor of Philosophy degree in the Department of Physics by:

Stephen Hsu, Chairperson, Physics
Graham Kribs, Member, Physics
David Strom, Member, Physics
Davison Soper, Member, Physics
Marina Guenza, Outside Member, Chemistry

and Richard Linton, Vice President for Research and Graduate Studies/Dean of the Graduate School for the University of Oregon.

September 5, 2009

Original approval signatures are on file with the Graduate School and the University of Oregon Libraries.

An Abstract of the Dissertation of

Wei Gong for the degree of Doctor of Philosophy
in the Department of Physics to be taken September 2009

Title: THEORETICAL INVESTIGATIONS OF TERASCALE PHYSICS

Approved:

Dr. Davison E. Soper

In this dissertation, three different topics related to terascale physics are explored.

First, a new method is suggested to match next-to-leading order (NLO) scattering matrix elements with parton showers. This method is based on the original approach which adds primary parton splittings in Born-level Feynman graphs in order to remove several types of infrared divergent subtractions from the NLO calculation. The original splitting functions are modified so that parton showering has a less severe effect on the jet structure of the generated events.

We also examine the Large Hadron Collider phenomenology of quantum black holes in models of TeV scale gravity. Based on a few minimal assumptions, such as the conservation of color charges, interesting signatures are identified that should be readily visible above the Standard Model background. The detailed phenomenology depends heavily on whether one requires a Lorentz invariant, low-energy effective field theory description of black hole processes.

Finally, in the calculation of cross sections in high energy collisions at NLO, one option is to perform all of the integrations, including the virtual loop integration, by Monte Carlo numerical integration. A new method is developed to perform the loop integration directly, without introducing Feynman parameters, after suitably

deforming the integration contour. Our example is the N -photon scattering amplitude with a massless electron loop. Results for six photons and eight photons are reported.

CURRICULUM VITAE

NAME OF AUTHOR: Wei Gong

PLACE OF BIRTH: Chengdu, Sichuan, China

DATE OF BIRTH: June, 1981

GRADUATE AND UNDERGRADUATE SCHOOLS ATTENDED:

University of Oregon, Eugene, Oregon, USA

University of Science and Technology of China, Hefei, China

DEGREES AWARDED:

Doctor of Philosophy in Physics, 2009, University of Oregon

Bachelor of Science in Physics, 2004, University of Science and
Technology of China

AREAS OF SPECIAL INTEREST:

Standard Model phenomenology

Monte Carlo algorithms

PROFESSIONAL EXPERIENCE:

Research assistant, Institute of Theoretical Science, University of
Oregon, 2005–2009

Teaching assistant, Dept. of Physics, University of Oregon, 2004–2009

PUBLICATIONS:

Wei Gong, Zoltan Nagy, and Davison E. Soper, “Direct numerical integration of one-loop Feynman diagrams for N-photon amplitudes”, Phys. Rev. D79:033005 (2009).

Xavier Calmet, Wei Gong, and Stephen D.H. Hsu, “Colorful quantum black holes at the LHC”, Phys. Lett. B668:20-23 (2008).

ACKNOWLEDGMENTS

I would like to thank my advisor Professor Davison Soper, who has always been there to help me to study as a scientist and to grow as an individual. Thank you for your constant encouragement, support and guidance. I have benefited so much from being your student for four years, and there are not enough words for me to express my gratitude. I would also like to thank Professor Stephen Hsu for countless helpful discussions during our collaborative research, and for his incisive thoughts and expertise outside the academic field which eventually enabled me to have the opportunity to launch my career in the business world. I want to acknowledge and thank Professor Graham Kribs, Professor Nilendra Deshpande and Dr. Xavier Calmet as well, for their helpful hints and advice along my way of pursuing the doctorate degree.

I want to thank my peers in the Institute of Theoretical Science, David Reeb, Ricky Fok, Tuhin Roy, and my former officemate Andrew Cook. I have learned so much from the many discussions with you. I also want to thank all the other faculty members, students and staff of the Department of Physics – you always make me feel at home although I am thousands miles away from where I came from. I wish you well in all that you do.

I am extremely fortunate to have a wonderful and caring family. To my mom, Jun Miao, my dad, Xiangjin Gong, and grandparents, aunts, uncles and cousins – thank you all for your love and support for so many years. I would not be able to achieve anything in my life without your belief in me.

And at last, but not in the least, I want to thank the most important person in my life, the sweetest person in the world, my lovely wife, Lei. You are my partner,

my best friend, and so much more. I can never thank you enough for all that you have done for me. I love you from the bottom of my heart.

To my wife – Lei Zhang – you keep my dream alive.

TABLE OF CONTENTS

Chapter	Page
I. INTRODUCTION	1
II. NLO CALCULATION AND PARTON SHOWERS	3
2.1 Introduction	3
2.2 Event Generator	4
2.3 Pure NLO Program	9
2.4 Parton Evolution	14
2.4.1 Introduction	14
2.4.2 Splitting Functions	15
2.4.3 Parton Evolution	29
2.4.4 Implementation	37
2.5 Adding Parton Showers	40
2.5.1 Motivation	40
2.5.2 Implementation	46
2.5.3 Numerical Tests	56
2.5.4 Manipulation of Splitting Functions	60
2.6 Event Shape Variables	64
2.6.1 Jet Algorithms	65
2.6.2 Thrust-Related Variables	65
2.6.3 C-Parameter	69
2.6.4 Sphericity	70
2.6.5 Energy-Energy Correlation Function	72
2.7 Numerical Results	74
2.7.1 Validating Numerical Results	74
2.7.2 Numerical Convergence	92
III. COLORFUL QUANTUM BLACK HOLES	98
3.1 Introduction	98

Chapter	Page
3.2 Extra Dimensions	99
3.2.1 Kaluza-Klein Theory	99
3.2.2 The Hierarchy Problem	100
3.3 Black Hole Formation at the LHC	105
3.3.1 Initial-State Radiation and PDFs	106
3.3.2 Inelasticity	108
3.3.3 Semi-Classic Black Holes	110
3.4 Quantum Black Holes and Cross Sections	118
3.4.1 What Is a Quantum Black Hole	118
3.4.2 Inclusive Cross Sections	119
3.4.3 Conservation of Gauge Charges	120
3.4.4 Individual Decay Channels	124
3.4.5 Cross Sections	126
3.5 Conclusions	129
IV. DIRECT NUMERICAL INTEGRATION	131
4.1 Introduction	131
4.2 Contour Deformation	137
4.2.1 Generic Form	137
4.2.2 Geometric Configuration	140
4.2.3 Double Parton Scattering	144
4.2.4 Deformation in All Four Regions	146
4.2.5 Notations for Cones	151
4.2.6 The Coefficients for $2 \leq A \leq N - 2$	151
4.2.7 The Coefficients for $A = 1$	155
4.2.8 The Coefficients for $A = N$	157
4.2.9 Size of the Deformation	157
4.3 Numerical Results	164
4.3.1 $N = 6$	166
4.3.2 $N = 8$	169
4.4 Conclusion	171
V. CONCLUSION	173
BIBLIOGRAPHY	174

LIST OF FIGURES

Figure	Page
2.1 Jet mass distribution	11
2.2 Cancellation between infrared divergences	12
2.3 Jet mass distribution by PYTHIA	13
2.4 Kinematics of timelike parton branching	15
2.5 Gluon splitting into gluons	17
2.6 Gluon splitting into quark-antiquark	20
2.7 Quark splitting into gluon and quark	23
2.8 Illustration of the evolution operator	34
2.9 NLO graphs that contributes to divergences	40
2.10 Cut propagators	41
2.11 Shower propagator	45
2.12 Deleting cut NLO graphs	45
2.13 Proposal function	51
2.14 Validating NLO calculation with showers	57
2.15 Jet mass distribution in the full NLO+PS+Had calculation	59
2.16 Distribution of jet masses	59
2.17 Three jet fraction	60
2.18 Three jet fraction with a modified splitting function	63
2.19 Thrust for pure NLO (91 GeV)	75

Figure	Page
2.20 Thrust for pure NLO (35 GeV)	76
2.21 Thrust with old splitting functions (91 GeV)	76
2.22 Thrust with old splitting functions (35 GeV)	77
2.23 Thrust with modified splitting functions (91 GeV)	77
2.24 Thrust with modified splitting functions (35 GeV)	78
2.25 C-Parameter for pure NLO (91 GeV)	78
2.26 C-Parameter for pure NLO (35 GeV)	79
2.27 C-Parameter with old splitting functions (91 GeV)	79
2.28 C-Parameter with old splitting functions (35 GeV)	80
2.29 C-Parameter with modified splitting functions (91 GeV)	80
2.30 C-Parameter with modified splitting functions (35 GeV)	81
2.31 Heavy Jet Mass for pure NLO (91 GeV)	81
2.32 Heavy Jet Mass for pure NLO (35 GeV)	82
2.33 Heavy Jet Mass with old splitting functions (91 GeV)	82
2.34 Heavy Jet Mass with old splitting functions (35 GeV)	83
2.35 Heavy Jet Mass with modified splitting functions (91 GeV)	84
2.36 Heavy Jet Mass with modified splitting functions (35 GeV)	84
2.37 Total Jet Broadening for pure NLO (91 GeV)	85
2.38 Total Jet Broadening for pure NLO (35 GeV)	85
2.39 Total Jet Broadening with old splitting functions (91 GeV)	86
2.40 Total Jet Broadening with old splitting functions (35 GeV)	86
2.41 Total Jet Broadening with modified splitting functions (91 GeV)	87

Figure	Page
2.42 Total Jet Broadening with modified splitting functions (35 GeV)	88
2.43 Wide Jet Broadening for pure NLO (91 GeV)	88
2.44 Wide Jet Broadening for pure NLO (35 GeV)	89
2.45 Wide Jet Broadening with old splitting functions (91 GeV)	89
2.46 Wide Jet Broadening with old splitting functions (35 GeV)	90
2.47 Wide Jet Broadening with modified splitting functions (91 GeV)	90
2.48 Wide Jet Broadening with modified splitting functions (35 GeV)	91
3.1 Protons forming a black hole	106
3.2 Number of final-state particles	114
3.3 An extra-dimensional black hole emits to brane and bulk modes	117
4.1 Feynman diagram for the N-photon amplitude	133
4.2 Kinematics for the N-photon amplitude, illustrated for N=8	141
4.3 Kinematics for the N-photon amplitude	142
4.4 Double parton scattering	145
4.5 Numerical results for six photon scattering amplitudes	168
4.6 Results for the Feynman parameter representation	169
4.7 Numerical results for the eight photon amplitude	170

LIST OF TABLES

Table		Page
2.1	Polarization dependence of collinear branching $g \rightarrow gg$	19
2.2	Polarization dependence of the branching $g \rightarrow q\bar{q}$	22
2.3	Polarization dependence of the branching $q \rightarrow qg$	25
2.4	Jet algorithms	66
2.5	Values of the shape variables	71
3.1	Cross-sections for the production of black holes	126
3.2	Possible final states in quantum black hole decay	129

CHAPTER I

INTRODUCTION

The Large Hadron Collider (LHC) has been built in Geneva, Switzerland, which will enable us to probe the fundamental building blocks of our universe at a unprecedented energy scale. In this collider, protons beams will be smashed together at a center-of-mass energy of 14 tera electron volts (TeV). In such a regime, it is believed by many that new physics beyond the Standard Model will emerge. A large number of theoretical models have been developed to resolve some open problems that remain in the Standard Model, and those new theories can predict what new could possibly come out of the LHC. For example, some suggest there are extra dimensions in addition to the ordinary 4 spacetime dimensions, which might lower the fundamental scale of gravity and give rise to the production of mini black holes. In this dissertation, we will discuss the phenomenology of such black holes whose size is even smaller than that of a proton.

Many experiments need to be performed at the LHC to test the validity of those new physics theories. Any of such theories will be strongly supported if some of its unique signatures can be identified above the Standard Model background. As a result, it is important for us to improve both the accuracy and efficiency of numerical calculations based on the Standard Model, so that interesting signatures for Terascale physics could more easily be observed. For this purpose, we will investigate two other topics in this dissertation. One of them is about matching next-to-leading order (NLO) scattering matrix elements with parton showers using primary splittings, and the other is about the direct numerical integration of virtual loop Feynman diagram with multiple external legs.

This dissertation will first introduce our method to match NLO calculation with parton showers. Following that, we will cover the phenomenology of quantum black holes at the LHC. Finally, the direct numerical integration of virtual loop graphs will be discussed.

CHAPTER II

NLO CALCULATION AND PARTON SHOWERS

2.1 Introduction

Perturbation theory is one of the most powerful tools when it comes to predicting various aspects of possible outcome of elementary particle experiments. Monte Carlo (MC) event generators have been built as an application of the perturbation theory of the standard model of elementary particle physics. They can produce final-state events according to fundamental theories like Quantum Electro Dynamics (QED) and Quantum Chromo Dynamics (QCD). People can match the simulated events with realistic events from lab experiments by comparing properties like cross sections, event shape, and other observables. Through tuning those input parameters in the standard model, for example, the strong coupling constant α_S , people are able to find out how good the match can be, and thus evaluate the theories behind the particle model. Specifically, when strong interactions are involved, MC event generators can be created based upon perturbative QCD calculation. But we can not carry out sensible perturbative calculations of QCD unless there is large momentum transfer or short-distance interaction. The reason is in order to make perturbation theory work properly, the strong coupling constant has to be small because the results are usually expanded in powers of $\alpha_S(Q)$. And for a non-Abelian theory, QCD, the strong coupling constant will decrease as the energy scale Q of the process increases. This phenomena is known as “asymptotic freedom”. Approximately speaking, it would make sense for people to use the perturbative approach to tackle problems with strong interactions only when Q is much bigger than 1 GeV. People

can also choose to measure only “infrared-safe” observables to exclude most of the low scale effects like hadronization. On the other hand, those well accepted MC event generators today can only do leading-order calculations, and contributions from higher order perturbative terms can make those generators heavily depend on the input renormalization scale of the programs. It will be necessary to include the next-to-leading order terms or even higher order effects in the event generator so that one can deal with more advanced experiments like those in the upcoming Large Hadron Collider (LHC). I have done a project that focuses on how to match parton showers to pure next-to-leading Order (NLO) computations, which is the key to developing a MC event generator accurate to NLO in QCD.

2.2 Event Generator

People usually make up observables to describe the shape of events. For example, F can be a function of final-state momenta, and we use the following formula to calculate an observable based upon this function [1],

$$\sigma[F] = \sum_n \frac{1}{n!} \int d\vec{p}_1 \cdots d\vec{p}_n \frac{d\sigma}{d\vec{p}_1 \cdots d\vec{p}_n} \times F_n(\vec{p}_1, \cdots, \vec{p}_n). \quad (2.1)$$

In the above expression, \vec{p}_i is the final-state momentum, $d\sigma/d\vec{p}_1 \cdots d\vec{p}_n$ is the cross section to make n massless partons. For the purpose of this article, all n partons are treated as identical when defining the cross section and therefore we divide by a factor of $n!$, because we can intentionally construct function F to be independent of flavor and color of final-state partons, and symmetric under interchange of any of parton momenta.

F also needs to be infrared-safe as well, but what exactly is the so-called “infrared-safety”? If a certain function F meets the criteria mentioned above, and if in the limit where two partons become collinear, or one becomes soft, it also has the following property [2]:

$$F_{n+1}(\vec{p}_1, \vec{p}_2, \cdots, (1-\lambda)\vec{p}_n, \lambda\vec{p}_n) = F_n(\vec{p}_1, \vec{p}_2, \cdots, \vec{p}_n), \quad (2.2)$$

then this function is infrared safe.

There are a few reasons for people to use infrared safe observables to probe processes like $e^+e^- \rightarrow \text{hadrons}$. One of them is that a lot of long distance effects cannot be calculated accurately. For example, there is no model in which final-state partons can evolve through the stage of hadronization numerically, because at this low energy scale, as predicted by non-Abelian gauge theory, the strong coupling constant α_S has become so big that perturbation theory breaks down. Thus in current QCD event generators, hadronization can only be realized with the help of various phenomenological models, and those models can introduce systematic errors, with their sizes not clearly known. However, compared to the hard part of the scattering process, two interacting particles during the hadronization stage can be treated as being either collinear with each other or one being soft. Therefore, a well-constructed infrared safe observable can measure the hard scattering matrix elements precisely, while being very insensitive to uncertainties brought by our choice of hadronization models.

Another reason for us to stick to infrared safe observables is, when people use equation (2.1) to calculate $\sigma[F]$, there are infrared divergences which will cancel between terms with difference number of partons. In order to make sure the cancellation works correctly, functions of difference parton numbers have to be related in the way set by equation (2.2).

It should be helpful to briefly show the origin of those divergence present in the infrared region. Let us take quark splitting into a quark-gluon pair as an example. Assume that the two daughter partons are both on-shell. For the daughter quark, this means $q^2 = m^2$; and for the daughter gluon, this means $p^2 = 0$. If there is no quark flavor change during the splitting, and assuming $|\vec{q}| = zE_q$ where $0 < z < 1$,

then the denominator of the mother quark's propagator would be

$$\begin{aligned}
 (q + p)^2 - m^2 &= (q^2 - m^2) + p^2 + 2(p \cdot q) \\
 &= 2(p \cdot q) \\
 &= 2E_p E_q (1 - z \cos \theta) ,
 \end{aligned} \tag{2.3}$$

where θ is the angle between two daughter partons. For the numerator factor of this same propagator, it turns out to contain a factor of θ in the collinear limit. Then apparently, at high energy when $z \rightarrow 1$, the squared matrix element including this splitting process is approximated by

$$|M|^2 \sim \left(\frac{\theta}{E_p E_q \theta^2} \right)^2 \tag{2.4}$$

when $\theta \rightarrow 0$. Then, the cross section

$$\begin{aligned}
 \sigma &\sim \int \frac{E_p^2 dE_p d \cos \theta d\phi}{E_p} \left(\frac{\theta}{E_p E_q \theta^2} \right)^2 \\
 &\sim \int \frac{dE_p}{E_p} \int \frac{d\theta^2}{\theta^2}
 \end{aligned} \tag{2.5}$$

can apparently become divergent as the two daughter partons go collinear or the gluon gets very soft. However, if we include another graph of the same order, but with a virtual loop in place of the splitting, then the infrared singularity that appeared above would be cancelled by another singularity provided by this newly added graph.

Now I will start to explain how to use a typical event generator to calculate such an observable. Usually, many events will pop out of the event generator, with a certain weight factor w_i assigned to each event, which plays the role of the cross section of events with the corresponding final-state momentum configuration. However, some event generators would sometimes give negative weights [2]. The observable will be calculated in the way given below:

$$\sigma[F] = \frac{1}{N} \sum_{i=1}^N w_i F \left(p_1^{\{i\}}, p_2^{\{i\}}, \dots, p_n^{\{i\}} \right) . \tag{2.6}$$

N is the total number of events generated. Alternatively, some other event generators assign the same weights, for example, $w_i = 1$ to all events, and in that case the probability of a certain event being generated will be equal to the probability of the same event being found in real world, predicted by the theories and models incorporated in the event generator.

In order to understand the advantage and disadvantage of using Monte Carlo event generators for the purpose of calculating observables of various QCD processes, it is necessary to compare it with other methods. The simplest way of doing such calculation is to write down the perturbative expansion of the observable in powers of α_S . Assuming the hardest part of the process starts at α_S^B , then

$$\sigma[F] = C_0[F]\alpha_S^B + C_1[F]\alpha_S^{B+1} + C_2[F]\alpha_S^{B+2} + \dots . \quad (2.7)$$

Programs have been developed that can calculate the coefficients for the first two terms for a variety of observables. In some cases, those programs can even calculate to the next-to-next-to-leading order. A famous example is the Monte Carlo matrix element evaluation program *EVENT2* [3]. Generally speaking, since most programs of this kind involve next-to-leading order calculations, the theoretical uncertainty brought by higher order terms can be limited to only $\sim 10\%$, which is pleasant. However, for measurements that are sensitive to final state structures, this purely perturbative way of computation would run into trouble because they can only give sensible answers to event-shape variables based on evaluating very few final state partons, while in the real world, there are many more particles present in the final state, in the form of hadrons, leptons, photons, etc., not partons. Plus, long distance effects like initial-state radiation (ISR) and final-state hadronization are completely ignored here, and thus the prediction given in this way would deviate seriously away from the true results through measuring real physical final-state particles.

The benefit of Monte Carlo event generators is now very obvious. They can produce a list of final-state physical particles along with detailed information of those particles, like momentum, which actually make up of the final state of the real

collision. Then one can apply detector simulations to the outcome of event generators and study any possible departure of lab detector from measurements given by ideal detector.

However, this very feature of a typical Monte Carlo event generator, which makes the above study possible, also causes problems. The hadronization model ([4][5][6]) utilized by event generators is far from being called an exact description of what happens in the realistic hadronizing process. It is only a phenomenological model which can combine final state partons in a certain way into hadrons similar to what we see in the experiments. Fortunately, as what was pointed out earlier in this thesis, hadronization only involves splittings and recombinations whose virtualities are much smaller compared to the short-distance reaction which only appears in the scattering matrix elements and the first few steps of parton showers. As a result, if we carefully choose our measurement functions to be infrared safe, then the limitation that comes with this unphysical hadronization model would not make a big problem.

The real issue is about the scattering matrix elements that are taken into account by most contemporary Monte Carlo event generators. Only LO Feynman diagrams are considered when those programs are dealing with the short-distance physics. The consequence is, due to throwing away higher order terms beyond the leading order in the perturbative expansion of differential cross section of QCD jet production, large systematic uncertainty [7] is brought into the simulation results from calculations based on virtual events generated by those programs. This is because the size of NLO terms and beyond are very considerable although α_S is small at large momentum transfer. In fact, corrections from terms other than pure LO terms can be up to $\sim 50\%$ of the lowest order results. And by putting NLO effects into consideration, the estimated errors can sharply drop down to around 10% of the results. Naturally, the analysis above has led to many efforts to match NLO Monte Carlo event generators to NLO perturbative calculations, so that our calculation could be accurate to the α_S^{B+1} terms in the perturbative expansion, where B has been defined in Eq. (2.7).

2.3 Pure NLO Program

Most pure NLO programs we have right now, adopt a mechanism of calculation very similar to LO Monte Carlo event generators. Specifically, NLO programs generate lists of final-state partons by evaluating both LO and NLO Feynman graphs, and provide information of those partons, including momenta, flavors, colors, etc. If we name a certain final state as f_i , observables will be calculated in the style [1] we are familiar with:

$$\sigma[F] = \frac{1}{N} \sum_{i=1}^N w_i F(\{f_i\}) . \quad (2.8)$$

Unlike LO Monte Carlo event generators which usually set all their weight factors to be always 1, NLO programs can generate both positive and negative weights for different final states f_i , and those weights cannot be explained anymore as the probabilities of various events being generated by pure NLO calculation. It is not hard to understand why negative weights would appear if we are aware of the fact that NLO programs do real quantum calculations, and a certain weight is derived by multiplying one matrix element with the complex conjugate of another matrix element. Thus the real part of the complex number that represents the weight could be either positive or negative. But we should not really treat the appearance of negative weights as a big disaster, because computers have no trouble at all adding positive and negative numbers all together.

Let us take the reaction $e^+e^- \rightarrow hadrons$ as an example. Since NLO programs calculate all LO and NLO Feynman diagrams that have at least 3 partons in the final state, the results for various cross sections should now be accurate to the first two terms of equation (2.7) if we restrict ourselves to measuring cross sections for ‘3-jet’ infrared safe variables, which only give nonzero values to events that have at least 3 partons in the final state. This is a success if we consider the fact that LO Monte Carlo event generators can only be accurate to the first term of equation (2.7).

Unfortunately, typical NLO programs have serious defects as well. Events have only 3 or 4 partons in the final state because only hard interactions are taken into

account in the calculation. Splitting in the infrared region, also known as ‘parton showering’, and the stage of hadronization are completely ignored. Therefore, the events cannot be directly fed into a detector simulator.

What is more disappointing is that events given by pure NLO programs can not give sensible results to certain calculations. The 3-jet cross section σ_3 is a ‘3-jet’ infrared observable. According to the analysis given above, pure NLO programs can calculate this quantity to the second order in the perturbative expansion. Now we introduce another quantity, jet mass M , which is defined as [8]:

$$M = \left(\sum_i p_i \right)^2, \quad (2.9)$$

where the summation is taken among all partons inside one of the jets in the final state. Apparently we would have

$$\sigma_3 = \int dM \frac{d\sigma_3}{dM}, \quad (2.10)$$

and everything is satisfactory if our only concern is the total ‘3-jet’ cross section. But in practice, the differential cross section $d\sigma_3/dM$ is also of enormous value because it can tell us what is the fraction of the ‘3-jet’ events whose jet widths share a certain pattern. Information like this is very important because detectors would react differently to jets with different widths. And in order to reconstruct the real final states based on measurements done by detectors, people need to know what exactly happens when detectors deal with jets with different widths. Figure 2.1 provided by [9] is a plot that displays the distribution of the normalized jet mass distribution $\sigma_3^{-1}d\sigma_3/dM$ versus jet mass M , calculated from a pure NLO program. Obviously, the distribution is behaving strangely in the region where the invariant jet mass is very small. The differential cross section goes up rapidly as the jet mass goes down toward zero, and suddenly drops to a very ‘big’ negative value represented by the leftmost bin, which is completely unphysical. However, if one carefully adds the areas of those bins together, they would find out it is a result for the total 3-jet cross

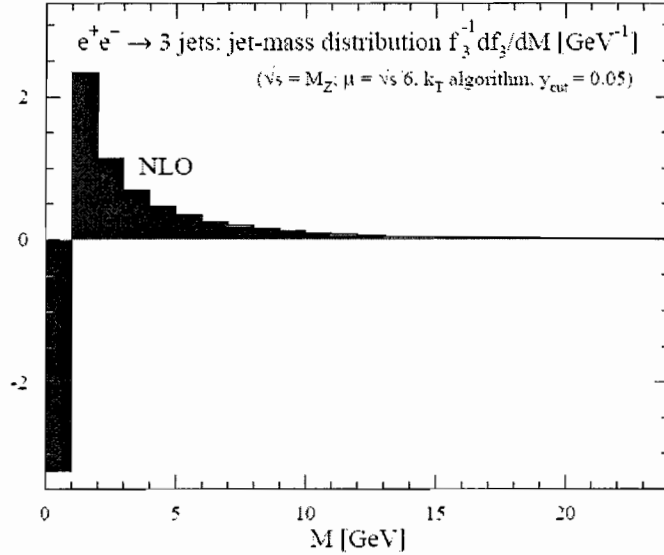


FIGURE 2.1: Jet mass distribution in 3-jet events, calculated at next-to-leading order. This figure is provided by [9].

section accurate to the next-to-leading order. One can easily conclude that, there is something wrong about the way we calculate the jet mass distribution when one of the jets contains two collinear final-state partons.

As mentioned before, a pure NLO program would only generate a list of 3 or 4 partons which constitute the final state. When those partons are reconstructed to form 3 jets using a certain jet-finding algorithm, only the jet that has two partons can give nonzero jet mass, $(p_i + p_j)^2$, while the other two jets have zero jet masses because they are separately formed by only 1 parton, and when final state partons are on mass shell, their invariant masses are treated as zero, if the program is working under the assumption all partons are massless. Thus the small jet mass region in fact corresponds to the region where the 2 partons in the heaviest jet become collinear, or one becomes soft, and only the collinear situation will be discussed for now. Naively one would think things should be fine in that region because in NLO calculation, the infrared singularity of the Feynman diagram with collinear splitting should be

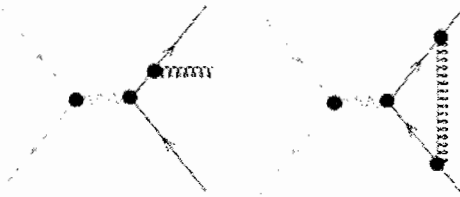


FIGURE 2.2: Cancellation between infrared divergences.

cancelled by a counter-term provided by a similar diagram but with the splitting replaced by a virtual loop. But the truth is that events generated by calculating virtual loop diagrams would enter different bins of M . Since there is no collinear splitting during the calculation of such diagrams, there could be only 3 partons in the final state of one event like this, along with a negative weight, as we have already argued. And 3-parton events apparently have zero jet mass, and thus will always contribute to the leftmost bin on the M axis, while its positive counter-term sit in another bin that represents a small jet mass.

In fact, because of this absence of singularity cancellation in a certain bin near zero, the measurement carried out in Figure 2.1, $\sigma_3^{-1}d\sigma_3/dM$, will theoretically diverge $\sim \log M/M$, while a negative delta function, $-\delta(0)$, would appear in the bin of $M = 0$. Not surprisingly, since those troublesome singularities can cancel each other if we add areas in all bins together, the prediction of the total 3-jet cross section would be accurate to the next-to-leading order.

On the other hand, if instead a LO Monte Carlo generator is used in this case as shown in Figure 2.3 [9], the simulation results would make much more sense, thanks to the parton showering algorithms that treat two opposite singular diagrams as one single event going through collinear or soft splitting and thus successfully get rid of the divergences scattered around in the case of using pure NLO programs by suppressing the singularities with a Sudakov factor. From here, one would be naturally motivated to merging the parton shower algorithm with a pure NLO program, and to expect

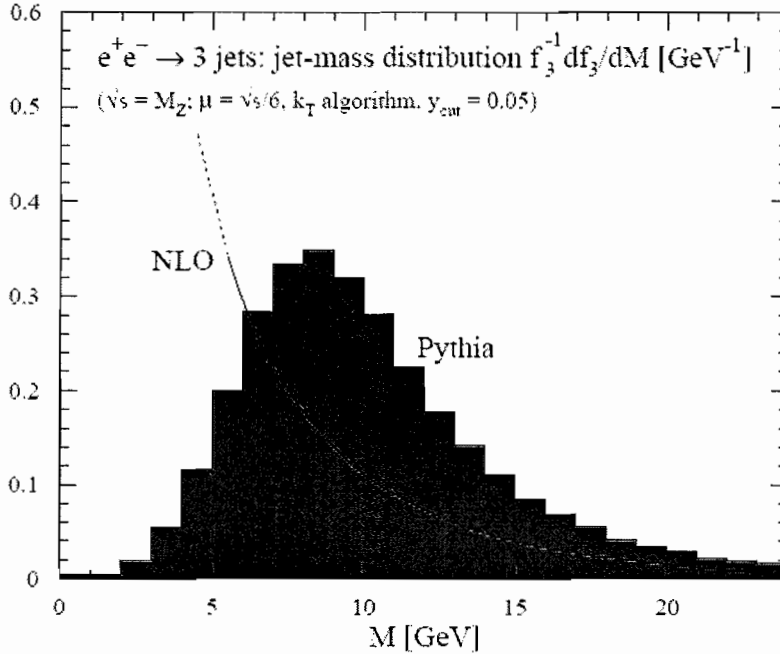


FIGURE 2.3: Jet mass distribution in 3-jet events, calculated by PYTHIA. This figure is provided by [9].

that the resulting event generator can help measure observables that are somehow sensitive to the structure of the final state, like $\sigma_3^{-1} d\sigma/dM$, while still able to maintain the next-to-leading order accuracy. We need to match the LO parton showers to NLO matrix elements very carefully because parton splittings at the interface are very close to the hardest interaction where $\gamma/Z_0 \rightarrow q\bar{q}$. It involves important short-distance effects, and would have a considerable impact on what one can get out of the final states even if only infrared safe measurements are carried out. There are a couple of issues that need to be taken care of. First of all, the virtuality scale of the first splitting should be bigger than subsequent splittings, required by the assumptions people have taken to make the approximations of parton showering work. It will be the topic of the next section. In fact not only the transverse momentum scale of the first splittings, but also other matters associated with the pure NLO final state

partons like flavor, color, etc., should also be translated carefully to the language of parton showering. Secondly, when the LO diagrams are combined with the first stage of showering and one also includes pure NLO graphs, some short-distance effects that used to be calculated by hard NLO matrix elements have now also been included in some of the first splittings. So efforts must be made to avoid possible double counting as well.

2.4 Parton Evolution

2.4.1 Introduction

Today perturbative calculations in QCD have only been performed to next-to-leading order in most cases. The computation involved if we go to higher fixed order would approximately increase factorially, and this probably cannot be solved anytime soon. Meanwhile the effects of a portion of all higher order terms could be enhanced in certain region of the phase space, and need to be taken into account if one wants to avoid unphysical divergences and get sensible theoretical predictions throughout the entire kinematic region of final-state particles. So instead of calculating endless higher order Feynman graphs accurately, an algorithm called “parton showering” has been developed to sum over certain kinds of terms approximately to all orders in the phase space region where they become important. This algorithm usually deals with interactions with a virtuality scale $t > t_0$, and t_0 is a infrared cut-off scale which are usually taken to be of order 1 GeV. Beyond this cut-off scale non-perturbative effects would get more important and thus can not be neglected anymore. Often people would use a phenomenological hadronization model to take over from here. Those two algorithms together could then coexist perfectly together in a numerical program, known as Monte Carlo event generator.

In this section, brief calculations will be given to illustrate what a typical showering algorithm is, starting with introducing parton splitting functions in the

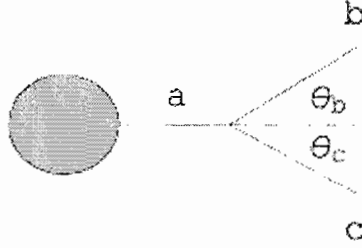


FIGURE 2.4: Kinematics of timelike parton branching.

collinear limit. The procedures provided in [10] will be followed in this thesis when deriving parton splitting functions. The shower structure will then be built and implemented into a Monte Carlo program. Soft singularities will also be discussed but most details will be put aside, because it is not the focus of this research. Strictly speaking, parton shower usually refers to both initial state radiation and final state evolution; however, I will restrict myself to final state showers.

2.4.2 Splitting Functions

Figure 2.4 shows the kinematics of a certain diagram that describes parton splitting. The assumption we are making here is that compared to mother parton a 's virtuality t , both daughter partons b and c can be approximately treated as on-shell. Moreover, we assume the virtuality t of the mother parton corresponds to a small splitting angle $\theta_{bc} \ll 1$, so that we will only talk about collinear splitting here:

$$t \equiv p_a^2 \gg p_b^2, p_c^2. \quad (2.11)$$

Due to momentum conservation at the branching vertex, we have both

$$z \equiv \frac{E_b}{E_a} = 1 - \frac{E_c}{E_a} \quad (2.12)$$

and

$$\begin{aligned}
t &= (p_b + p_c)^2 \\
&= 2E_b E_c (1 - \cos \theta_{bc}) \\
&\approx E_b E_c \theta_{bc}^2 \\
&= z(1-z) E_a^2 \theta_{bc}^2
\end{aligned} \tag{2.13}$$

z is known as the energy fraction. In the last equation, small angle approximation has been applied thanks to the fact that parton a is only slightly off-shell. It is not hard to see that t is always positive if Eq.(2.11) is satisfied, and such a process is given the name ‘time-like branching’. Before proceeding, the relations between different angles in the splitting also need to be worked out. In the plane defined by this splitting, applying momentum conservation, together with the small angle and on-shell approximation $|\vec{p}| \approx E$ for parton b and c , the following can be derived:

$$E_b \sin \theta_b = E_c \sin \theta_c \Rightarrow \frac{\theta_b}{\theta_c} \approx \frac{1-z}{z} . \tag{2.14}$$

As a result,

$$\theta_{bc} = \frac{1}{E_a} \sqrt{\frac{t}{z(1-z)}} = \frac{\theta_b}{1-z} = \frac{\theta_c}{z} . \tag{2.15}$$

Now let us start calculating some specific time-like branching diagrams. To start with, let all three partons a, b, c be gluons. According to the Feynman rule for the triple-gluon vertex,

$$V_{ggg} = igf^{ABC} \varepsilon_a^\alpha \varepsilon_b^\beta \varepsilon_c^\gamma \left[g_{\alpha\beta} (p_a - p_b)_\gamma + g_{\beta\gamma} (p_b - p_c)_\alpha + g_{\gamma\alpha} (p_c - p_a)_\beta \right] , \tag{2.16}$$

where α, β, γ are Dirac indices; A, B, C are indices of $SU(3)$ gauge group’s generators; a, b, c are parton indices; ε_i^μ is the polarization vector for gluon i ; f^{ABC} is the structure constant of the *Lie algebra* of the gauge group. In addition, all three momenta will be defined as outgoing, and that leads to $-p_a = p_b + p_c$. Now that all three gluons are almost on shell, considering the Ward Identity for non-Abelian gauge theories,

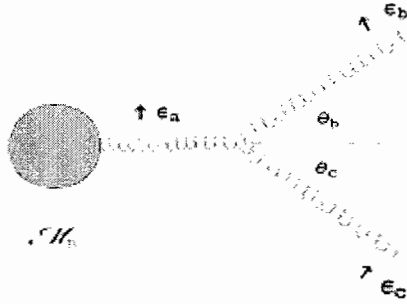


FIGURE 2.5: One gluon splitting into two other gluons.

only diagrams with all on-shell particles purely transversely polarized will survive the calculation of cross section, implying $\varepsilon_i \cdot p_i = 0$. Given all above, the triple-gluon vertex becomes

$$V_{ggg} = -2igf^{ABC} [(\varepsilon_a \cdot \varepsilon_b)(\varepsilon_c \cdot p_b) - (\varepsilon_b \cdot \varepsilon_c)(\varepsilon_a \cdot p_b) - (\varepsilon_c \cdot \varepsilon_a)(\varepsilon_b \cdot p_c)] . \quad (2.17)$$

Before the expression for V_{ggg} can be further simplified, the dot products of polarization factors and parton momenta have to be worked out. It would turn out to be convenient to use the plane defined by the splitting, and call those polarization vectors lying on the plane ε_i^{in} , and those perpendicular to the plane ε_i^{out} . ε_i^{in} and ε_i^{out} are also known as plane polarization states. A typical polarization vector would look like this:

$$\varepsilon_i^{in} = (0, 1, 0, 0) . \quad (2.18)$$

They are unit vectors, with only space components nonzero, and have to satisfy the general condition $\varepsilon_i \cdot p_i = 0$. Thanks to the small angle approximation, all three ε_i^{in} can point along approximately the same direction. All three ε_i^{out} can point along the same direction as well, and thus one would have:

$$\begin{aligned} \varepsilon_i^{in} \cdot \varepsilon_j^{in} &= \varepsilon_i^{out} \cdot \varepsilon_j^{out} = -1 \\ \varepsilon_i^{in} \cdot \varepsilon_j^{out} &= \varepsilon_i^{out} \cdot p_j = 0 . \end{aligned} \quad (2.19)$$

As for other products that appeared in Eq.(2.17), if one only keeps terms linear in θ_b and θ_c , and ignores all higher order terms, the following expressions can be derived:

$$\begin{aligned}\varepsilon_a^{in} \cdot p_b &= -E_b \theta_b = -z(1-z) E_a \theta_{bc} \\ \varepsilon_b^{in} \cdot p_c &= -E_c \theta_{bc} = (1-z) E_a \theta_{bc} \\ \varepsilon_c^{in} \cdot p_b &= -E_b \theta_{bc} = -z E_a \theta_{bc} .\end{aligned}\tag{2.20}$$

Now in Figure 2.4 let us call the shaded blob part of the diagram A_β , which needs one more factor of polarization vector before it becomes an independent matrix element, M_n . Define V_α by $V_{gg} = V_\alpha \varepsilon_a^\alpha$, and then write down the entire diagram, M_{n+1} , as follows:

$$M_{n+1} = A_\beta \frac{g^{\beta\alpha}}{t} V_\alpha = A_\beta \frac{\sum_{\text{polarizations}} \varepsilon^\beta \varepsilon^{\alpha*}}{t} V_\alpha = \sum_{\text{polarizations}} \frac{1}{t} V_{gg} M_n ,\tag{2.21}$$

and only the term with purely transverse ε^α in the summation over all polarization states would survive when adding all diagrams together, because non-physical polarized terms would get cancelled out by various diagrams like those with ghost particles. The completeness relation $g^{\mu\nu} = \sum_{\text{polarizations}} \varepsilon^\mu \varepsilon^{\nu*}$ has been used. Thus by putting Eq.(2.13), (2.17), (2.19) and (2.20) together, sum over all colors one could get

$$|M_{n+1}|^2 \sim \frac{4g^2}{t} C_A F(z; \varepsilon_a, \varepsilon_b, \varepsilon_c) |M_n|^2 ,\tag{2.22}$$

where $C_A = f^{ABC} f^{ABC} = 3$ is the color factor; values of function $F(z; \varepsilon_a, \varepsilon_b, \varepsilon_c)$ for different configurations of plane polarizations are given in Table 2.1. Combinations of plane polarization states that are missing from Table 2.1 are forbidden. Now if one sum up F over all allowed polarizations of final state particles b and c , and average over the polarizations of the mother parton a , following equation would be derived:

$$\hat{P}_{gg}(z) \equiv C_A \langle F \rangle = C_A [(1-z)/z + z/(1-z) + z(1-z)].\tag{2.23}$$

$\hat{P}_{gg}(z)$ is the so-called unregularized gluon splitting function related to the corresponding *Altarelli-Parisi* kernel [11].

TABLE 2.1: Polarization dependence of collinear branching $g \rightarrow gg$

ε_a	ε_b	ε_c	$F(z; \varepsilon_a, \varepsilon_b, \varepsilon_c)$
in	in	in	$(1-z)/z + z/(1-z) + z(1-z)$
in	out	out	$z(1-z)$
out	in	out	$(1-z)/z$
out	out	in	$z/(1-z)$

Before starting the discussion of other types of parton branching, it is worthwhile to stop and dig into the current case of branching a bit more. One can easily make the observation based on Table 2.1 that the splitting function would become divergent when the daughter gluon polarized in the plane of branching is soft. It is then natural to go on and ask what kind of correlation it would be between the plane of branching and the polarization of the mother parton. Let us call the angle ϕ between parton a 's polarization vector and the plane of branching, and then

$$\varepsilon_a = \cos \phi \varepsilon_a^{in} + \sin \phi \varepsilon_a^{out} , \quad (2.24)$$

therefore this time the splitting function

$$F_\phi \sim \sum_{\varepsilon_{b,c}} |\cos \phi M(\varepsilon_a^{in}, \varepsilon_b, \varepsilon_c) + \sin \phi M(\varepsilon_a^{out}, \varepsilon_b, \varepsilon_c)|^2$$

$$= \cos^2 \phi [|M(\varepsilon_a^{in}, \varepsilon_b^{in}, \varepsilon_c^{in})|^2 + |M(\varepsilon_a^{in}, \varepsilon_b^{out}, \varepsilon_c^{out})|^2] + \quad (2.25)$$

$$\sin^2 \phi [|M(\varepsilon_a^{out}, \varepsilon_b^{in}, \varepsilon_c^{out})|^2 + |M(\varepsilon_a^{out}, \varepsilon_b^{out}, \varepsilon_c^{in})|^2]$$

$$= \cos^2 \phi \left[\frac{1-z}{z} + \frac{1}{1-z} + 2z(1-z) \right] + \sin^2 \phi \left[\frac{1-z}{z} + \frac{1}{1-z} \right]$$

$$= \frac{1-z}{z} + \frac{1}{1-z} + z(1-z) + z(1-z) \cos 2\phi , \quad (2.26)$$

and notice there are no cross terms as $M^*(\varepsilon_a^{in}, \varepsilon_b, \varepsilon_c) M(\varepsilon_a^{out}, \varepsilon_b, \varepsilon_c)$ in the above calculation. That is because each matrix element appearing in the above equation includes nothing more than a single splitting vertex and is hence purely imaginary. Any cross term will therefore be exactly cancelled out by its complex conjugate term. Apparently, in Eq.(2.25), the first three terms in the last line give exactly the

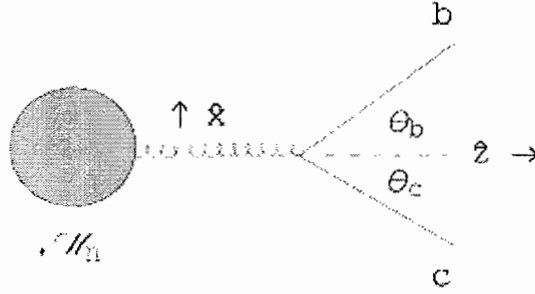


FIGURE 2.6: One gluon splitting into a quark-antiquark pair.

unpolarized result, while the last term represents the correlation, and it favors the situation where the mother gluon is polarized in the plane of branching. However, it is a very weak correlation: it can only be at most $1/9$ of the unpolarized contribution.

Now we can move on to talking about another type of parton splitting, $g \rightarrow q\bar{q}$. This time, the Feynman rule for the splitting vertex becomes

$$V_{gq\bar{q}} = -ig\bar{u}_b t^A \gamma_\mu \varepsilon_a^\mu v_c. \quad (2.27)$$

a, b and c are just names of three partons, not color indices. t^A is the generator of the Lie algebra of $SU(3)$ gauge group, with A as its generator index. \bar{u}_b and v_c are spinors of the quark and antiquark of certain colors, and they have both color and Dirac indices, which are left implicit in the above equation. Again, we have made use of the completeness relation for the $g^{\mu\nu}$ factor that appears in the numerator of the gluon propagator, $g^{\mu\nu} = \sum_{\text{polarizations}} \varepsilon^\mu \varepsilon^\nu$. And in the limit of collinear branching, only purely terms with purely transverse polarization vectors will survive the summation over different polarizations. Thus in Eq.(2.27), ε_a is chosen to be purely transverse.

To write down quark and antiquark spinors, a specific representation of the Lorentz group has to be determined first. Let us choose ([12])

$$\gamma^0 = \begin{pmatrix} 1 & 0 \\ 0 & -1 \end{pmatrix}, \quad \gamma^i = \begin{pmatrix} 1 & \sigma^i \\ -\sigma^i & 0 \end{pmatrix}. \quad (2.28)$$

In the above definition the matrix elements themselves are 2×2 matrices, and σ^i are Pauli matrices. Since we again work in the limit of collinear splitting, where gluon a travels towards $+z$, and $x - z$ is the plane of branching, then space momenta of quark b and c would only have small x components, and hence it makes a small angle approximation possible. Here the helicity eigenstates of quark and antiquark spinors to the first order in deviation angles will be given without proof in the representation ([12]),

$$\begin{aligned}
u_b^+ &= \sqrt{E_b} \begin{pmatrix} 1 \\ \frac{1}{2}\theta_b \\ 1 \\ \frac{1}{2}\theta_b \end{pmatrix}, & u_b^- &= \sqrt{E_b} \begin{pmatrix} -\frac{1}{2}\theta_b \\ 1 \\ -\frac{1}{2}\theta_b \\ 1 \end{pmatrix}, \\
v_c^+ &= i\sqrt{E_c} \begin{pmatrix} -\frac{1}{2}\theta_c \\ -1 \\ \frac{1}{2}\theta_c \\ 1 \end{pmatrix}, & v_c^- &= i\sqrt{E_c} \begin{pmatrix} -1 \\ \frac{1}{2}\theta_c \\ -1 \\ \frac{1}{2}\theta_c \end{pmatrix}.
\end{aligned} \tag{2.29}$$

Let us calculate the vertex $V_{gq\bar{q}}$ using one pair of the above helicity eigenvectors, which will determine the branching probability later.

$$\begin{aligned}
V_{gq\bar{q}} &\sim \bar{u}_b^- \gamma_\mu \varepsilon_a^{in,\mu} v_c^+ \\
&\sim \sqrt{E_b E_c} (\theta_b - \theta_c) \\
&= \sqrt{z(1-z)} E_a \theta_a \cdot (1-2z) \\
&= (1-2z) \sqrt{t}.
\end{aligned} \tag{2.30}$$

From here the whole matrix element can again be expressed as the product of the matrix element before the splitting and a vertex factor representing the branching ratio in a classic sense,

$$|\mathcal{M}_{n+1}|^2 \sim \frac{4g^2}{t} T_R F(z; \varepsilon_a, \lambda_b, \lambda_c) |\mathcal{M}_n|^2. \tag{2.31}$$

TABLE 2.2: Polarization dependence of the branching $g \rightarrow q\bar{q}$.

ε_a	λ_b	λ_c	$F(z; \varepsilon_a, \lambda_b, \lambda_c)$
in	\pm	\mp	$(1 - 2z)^2$
out	\pm	\mp	1

Details of derivation of the above equation is neglected since they are pretty similar to the $g \rightarrow gg$ case, except this time λ_i is used to represent the helicity eigenvalues, $\pm \frac{1}{2}$. Also a different color factor shows up, $T_R = \text{Tr}(t^A t^A) / 8$, which is actually a byproduct of summing over different colors of final state quarks and antiquarks and averaging over the generator index of the mother gluon, and this summation is left implicit in Eq.(2.31). The values of function F of different combinations of gluon polarizations and quark-antiquark helicities are given in Table 2.2. Other polarization configurations are not shown in the table because their function F vanishes due to the fact that quark-gluon coupling does not violate the helicity conservation implied by its own vector nature. There is no soft divergence associated with this type of splitting, and after summing over all helicity configurations of final states and taking the average of different gluon a polarizations,

$$\hat{P}_{q\bar{q}} \equiv T_R \langle F \rangle = T_R [z^2 + (1 - z)^2] . \quad (2.32)$$

If mother parton a is polarized in the plane of branching, the squared complete matrix element will vanish. In other words, the classic statistical possibility for this branching to happen is zero. This fact suggests a much stronger correlation between the polarization of parton a and the plane of splitting, unlike the case where $g \rightarrow gg$. The general splitting function F_ϕ can now be written down as

$$\begin{aligned} F_\phi &\sim \sum_{\lambda_{b,c}} |\cos \phi \mathcal{M}(\varepsilon_a^{in}, \lambda_b, \lambda_c) + \sin \phi \mathcal{M}(\varepsilon_a^{out}, \lambda_b, \lambda_c)| \\ &= 2 [\cos^2 \phi (1 - 2z)^2 + \sin^2 \phi] \\ &= 2 [z^2 + (1 - z)^2 - 2z(1 - z) \cos 2\phi] . \end{aligned} \quad (2.33)$$

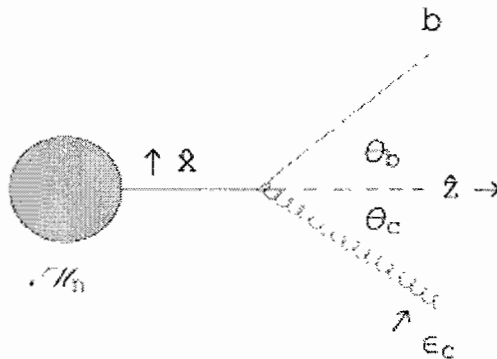


FIGURE 2.7: One quark splitting into a gluon and another quark.

The correlation term can reach its maximum again at $z = 1/2$, however, this time it could be as big as the unpolarized contribution when a is polarized in the plane of splitting. Note that there are still no cross terms such as $\mathcal{M}^*(\epsilon_a^{\text{in}}) \mathcal{M}(\epsilon_a^{\text{out}})$ in the final expression. In this case such terms are all purely imaginary, and will get cancelled out by their own complex conjugate terms during the calculation.

There is one more type of $1 \rightarrow 2$ parton splitting, $q \rightarrow qg$, or similarly, $\bar{q} \rightarrow \bar{q}g$. Once again, the Feynman rule of the quark-gluon-gluon vertex will be used to calculate the branching ratio later. Only quark splitting will be discussed here, and the case of antiquark splitting can be worked out in the same way introduced below. Assume a is the mother quark, b is the daughter quark and c is the daughter gluon, and then

$$V_{qgq} = -ig\bar{u}_a t^C \gamma_\mu \epsilon_c^\mu u_b. \quad (2.34)$$

When calculating the whole Feynman graph, which includes the quark splitting vertex, the numerator of quark a 's propagator, $(\gamma_\mu p_a^\mu + m)$, can be expressed as the sum of products of quark spinors over all spins, $\sum_s u^s \bar{u}^s$. It can be worked out straightforwardly by choosing a specific representation for the Lorentz symmetry group. This is basically how V_{qgq} acquire the factor of \bar{u}_a . And the rest of the big diagram will get the other factor in each term of the sum over spin states and

becomes a complete matrix element. But only when the quark virtuality is much smaller compared to the hard scattering scale can one justify the above treatments on quark a 's propagator, because strictly speaking, only on-shell fermions can be written down as states of definite helicities. So again one can work with the small angle approximation, and the eigenstates of different polarizations are

$$\begin{aligned}
u_a^+ &= \sqrt{E_a} \begin{pmatrix} 1 \\ 0 \\ 1 \\ 0 \end{pmatrix}, & u_a^- &= \sqrt{E_a} \begin{pmatrix} 0 \\ 1 \\ 0 \\ -1 \end{pmatrix}, \\
u_b^+ &= \sqrt{E_b} \begin{pmatrix} 1 \\ \frac{1}{2}\theta_b \\ 1 \\ \frac{1}{2}\theta_b \end{pmatrix}, & u_b^- &= \sqrt{E_b} \begin{pmatrix} -\frac{1}{2}\theta_b \\ 1 \\ \frac{1}{2}\theta_b \\ -1 \end{pmatrix}, \\
\varepsilon_c^{in} &= \begin{pmatrix} 0 \\ 1 \\ 0 \\ \theta_c \end{pmatrix}, & \varepsilon_c^{out} &= \begin{pmatrix} 0 \\ 0 \\ 1 \\ 0 \end{pmatrix},
\end{aligned} \tag{2.35}$$

but only accurate to the first order in splitting angles. The \pm here only represent the signs of helicities. As an example, let us calculate the vertex function when both quark a and b have positive definite helicities, and gluon c is transversely polarized in the plane of branching,

$$\begin{aligned}
\bar{u}_a^+ \gamma_\mu \varepsilon_c^{in, \mu} u_b^+ &= -\sqrt{E_a E_b} (2\theta_c + \theta_b) \\
&= -E_a \theta_{bc} \sqrt{z(1-z)} \cdot \frac{1+z}{\sqrt{1-z}} \\
&= -\sqrt{t} \cdot \frac{1+z}{\sqrt{1-z}},
\end{aligned} \tag{2.36}$$

and terms beyond the first order in splitting angles have again been neglected. After multiplying the whole diagram with its own complex conjugate, we also need to sum

TABLE 2.3: Polarization dependence of the branching $q \rightarrow qg$.

λ_a	λ_b	ε_c	$F(z; \lambda_a, \lambda_b, \varepsilon_c)$
\pm	\pm	in	$(1+z)^2/(1-z)$
\pm	\pm	out	$1-z$

over different colors of final-state quark b and the generator index of c , and average over the colors of a , because realistic detectors can not differentiate one color from another one when they respond to a certain event, and can not tell which color the mother quark has either. The following can then be shown:

$$|\mathcal{M}_{n+1}|^2 = \frac{4g^2}{t} C_F F(z; \lambda_a, \lambda_b, \varepsilon_c) |\mathcal{M}_n|^2 . \quad (2.37)$$

Another color factor appears, $C_F = \text{Tr}(t^C t^C)/3 = 4/3$. This can be worked out by looking into the properties of the representation we are using of the $SU(3)$ gauge group. Values of the polarization dependent function F are given in Table 2.3. Combinations of polarizations that are absent from Table 2.3 are forbidden because they do not obey the conservation of angular momentum implied by the vector nature of the quark-gluon coupling.(?) Actually their functions F would simply vanish if being calculated. One can sum F over polarizations of the final states, average over spins of the initial states, and get the *unregularized quark splitting function*,

$$\hat{P}_{qq}(z) \equiv C_F \langle F \rangle = C_F \frac{1+z^2}{1-z} . \quad (2.38)$$

According to Table 2.3, the polarized splitting function would diverge when then gluon polarizes in the plane of branching and becomes soft, $(1-z) \rightarrow 0$. On the other hand, there is no infrared singularity at all when the gluon polarization vector is normal to the plane of splitting. The above two facts together suggest the existence of correlation between the polarization of the daughter gluon and the plane of splitting, and the exact form of the correlation can be worked out again by using the method introduced earlier in this article. If the angle between the polarization vector ε_c and

the plane of branching is defined to be ϕ , then

$$\begin{aligned}
 F_\phi &\sim \frac{1}{2} \sum_{\lambda_{a,b}} \left| \cos \phi \mathcal{M}(z; \lambda_a, \lambda_b, \varepsilon_c^{in}) + \sin \phi \mathcal{M}(z; \lambda_a, \lambda_b, \varepsilon_c^{out}) \right|^2 \\
 &= \cos^2 \phi \frac{(1+z)^2}{1-z} + \sin^2 \phi (1-z) \\
 &= \frac{1+z^2}{1-z} + \frac{2z}{1-z} \cos 2\phi.
 \end{aligned} \tag{2.39}$$

In the first line of Eq.(2.39), there is a factor of $1/2$ in front of the sum over spins of both quarks because a is not in the final state, and therefore one should take the average over its spin states. Similar to what have been shown in the first two types of parton splitting, the first term represents the unpolarized splitting, and the second term is the correlation.

Up until now, having discussed the gluon polarization angle correlation of all three types of parton branching, one can come to several conclusions. In the collision process of $e^+e^- \rightarrow q\bar{q}$, when a gluon is emitted from one of the very first two quarks, it would tend to be polarized in the plane of splitting. When this gluon itself splits again, the plane of branching is more likely to be perpendicular to the mother gluon's polarization factor. The hardest two jets in the realistic final state of this process usually follow the directions of the two quarks out of the primary interaction vertex, while the softest two jets follow the directions of the produced quarks or gluons. If we temporarily put aside the triple gluon vertex, and assume QCD is described by an Abelian gauge theory, and then measure the angle between the plane of the hardest two jets and the plane of the softest two jets, we would be able to find out a distribution of cross section peaked at 90° of this angle, which is named as the Bengtsson-Zerwas angle. But the truth is, the maximum of this distribution appear around the Bengtsson-Zerwas angle being 60° , and the curve of distribution is much flatter than what an Abelian gauge theory would predict it to be. The experiment of measuring Bengtsson-Zerwas has certainly ruled out the possibility of QCD being constructed as an Abelian gauge theory. But if putting the triple gluon vertex back

in, as required by the non-Abelian, $SU(3)$ gauge theory, and taking into account the fact that $g \rightarrow gg$ is dominant in QCD, one could give a theoretical prediction which match the experimental data of measuring the Bengtsson-Zerwas angle extremely well.

It is worthwhile to determine the relation between the differential cross section of a certain QCD process, σ_n , and the differential cross section of the same process with one final state parton going slightly off-shell and splitting into two more partons, σ_{n+1} . To begin with, the cross section without the splitting is expressed as

$$d\sigma_n = \mathcal{F} |\mathcal{M}_n|^2 d\Phi_n, \quad (2.40)$$

where \mathcal{F} is the initial-state flux, same for both σ_n and σ_{n+1} , and $d\Phi_n$ is the group of final-state phase space integration variables,

$$d\Phi_n = \frac{d^3\vec{p}_1}{2(2\pi)^3 E_1} \cdots \frac{d^3\vec{p}_a}{2(2\pi)^3 E_a} \cdots \frac{d^3\vec{p}_n}{2(2\pi)^3 E_n}. \quad (2.41)$$

Assume now parton a splits into two other partons b and c , then the integration variables would become

$$d\Phi_{n+1} = \frac{d^3\vec{p}_1}{2(2\pi)^3 E_1} \cdots \frac{d^3\vec{p}_b}{2(2\pi)^3 E_b} \frac{d^3\vec{p}_c}{2(2\pi)^3 E_c} \cdots \frac{d^3\vec{p}_n}{2(2\pi)^3 E_n}. \quad (2.42)$$

Apply the energy and momentum conservation, $\vec{p}_a = \vec{p}_b + \vec{p}_c$ and $E_a = E_b + E_c$, one can multiply several identity integrals with $d\Phi_{n+1}$ in the small angle approximation, which are listed below:

$$\begin{aligned} 1 &= \int \delta(\vec{p}_a - \vec{p}_b - \vec{p}_c) d^3\vec{p}_a, & 1 &= \int \delta(t - E_b E_c \theta^2) dt, \\ 1 &= \int \delta\left(z - \frac{E_b}{E_a}\right) dz. \end{aligned} \quad (2.43)$$

The last two integrals are suggested by the kinematics we have been using throughout the derivation of various parton splitting functions. Consequently the integration variable $d^3\vec{p}_c$ in Φ_{n+1} can be replaced by $d^3\vec{p}_a$ by carry out the integral of $d^3\vec{p}_c$, and

the factor of energy E_c in the denominator can also be replaced by $E_a(1-z)$. By doing the above operations $d\Phi_{n+1}$ can be transformed to

$$\begin{aligned}
d\Phi_{n+1} &= d\Phi_n \int \frac{d^3\vec{p}_b}{2(2\pi)^3 E_b} dt \frac{dz}{1-z} \delta(t - E_b E_c \theta^2) \delta\left(z - \frac{E_b}{E_a}\right) \\
&= d\Phi_n \frac{1}{2(2\pi)^3} \int E_b dE_b \theta_b d\theta_b d\phi dt \frac{dz}{1-z} \delta(t - E_b E_c \theta^2) \cdot \\
&\quad \cdot \delta\left(z - \frac{E_b}{E_a}\right) \\
&= d\Phi_n \frac{1}{4(2\pi)^3} dt dz d\phi .
\end{aligned} \tag{2.44}$$

The third line of the last equation is derived by carrying out the integral over dE_b and $d\theta_b$. And note that $d^3\vec{p}_b = E_b^2 \theta_b dE_b d\theta_b d\phi$ is only true when $\theta_b \ll 1$. Now we are fully equipped to write down

$$\begin{aligned}
d\sigma_{n+1} &= \mathcal{F} |\mathcal{M}_{n+1}|^2 d\Phi_{n+1} \\
&= \mathcal{F} \frac{4g^2}{t} CF |\mathcal{M}_n|^2 d\Phi_n \frac{1}{4(2\pi)^3} dt dz d\phi \\
&= d\sigma_n \frac{dt}{t} dz \frac{d\phi}{2\pi} \frac{\alpha_S}{2\pi} CF .
\end{aligned} \tag{2.45}$$

C and F here are the corresponding color factor and polarized z-distribution function, and the strong coupling constant $\alpha_S = g^2/(4\pi)$. One can integrate out the azimuthal angle ϕ to further simplify this equation:

$$\int \frac{d\phi}{2\pi} CF = \hat{P}_{ba}(z) , \tag{2.46}$$

and $\hat{P}_{ba}(z)$ is the splitting function of the studied branching process, and hence one can write down

$$d\sigma_{n+1} = d\sigma_n \frac{dt}{t} dz \frac{\alpha_S}{2\pi} \hat{P}_{ba}(z) . \tag{2.47}$$

Discussion about space-like branching will be omitted here, since it is only related to Initial-State Radiation(ISR), which is not the concern of this thesis.

2.4.3 Parton Evolution

Processes like $e^+e^- \rightarrow \text{hadrons}$ typically have many particles in the final states, and apparently a big number of hadrons cannot be evolved directly from just 3 or 4 partons produced by the hardest interaction. Some important intermediate steps have to be studied before one can even start to talk about the stage of hadronization. Especially if one wants to build a Monte Carlo event generator that can both be accurate to the next-to-leading order and give physical final-state particles, one would have to figure out an approach to make many more partons out of the very few quarks and gluons that can be produced by a pure NLO program, so that the hadronization model can be started with a large enough number of partons. Unfortunately, when summing over all necessary Feynman graphs that can give rise to many final state partons, it is very difficult to take virtual graphs into account properly. However, one can make use of the splitting functions that have been just introduced to make up a model where very few partons could repeatedly split into more partons, with branching ratios given by classical statistics.

To begin with, let us study a simplified model suggested in [13] where only one type of massless scalar particles can be produced by the e^+e^- collision and only this same kind of particles would be involved in the formation of hadrons that can be finally detected by lab equipments. Many details of interactions among those scalar particles are not the major concerns here either, but collinear divergences similar to those in QCD process can still be present if one specifies the properties of the scalar particles in a certain way, for example, it can have an interaction term of ϕ^3 , and lives in a space with six dimensions. Anyway, the cross section to measure a certain infrared-safe observable F can still be written down as

$$\sigma [F] = \sum_m \frac{1}{m!} \int [d\{p\}_m] |\mathcal{M}(\{p\}_m)|^2 F(\{p\}_m) , \quad (2.48)$$

and the integrations are defined as

$$\int [d\{p\}_m] \equiv \left\{ \prod_{i=1}^m \int \frac{d^6 p_i}{(2\pi)^6} \delta(p_i^2) \right\} (2\pi)^2 \delta\left(P_0 - \sum_{i=1}^m p_i\right), \quad (2.49)$$

which can put all final state momenta on shell with the factors $\delta(p_i^2)$, and force the momentum being conserved throughout the collision, with $P_0 = (\sqrt{s}, \vec{0})$. $\mathcal{M}(\{p\}_m)$ as before is the matrix element to produce m partons with momentum configuration $\{p\}_m$, and $F(\{p\}_m)$ gives the value of the measurement of such a set of partons.

Now since people have big trouble calculating all those matrix elements, we will use a function $\rho(\{p\}_m)$ to stand for an approximated cross section of having m partons in the final state, and use it to replace the factor of squared matrix element in Eq.(2.48). The function ρ will be derived by using small angle approximation on particles with small virtualities splitting into two collinear particles. Basically, the cross sections of all processes with more than two or three final-state particles will be calculated by multiplying $\mathcal{M}(\{p\}_{n=2 \text{ or } 3})$ with the classical total probability of branching the first n particles to m particles in the end. Since the branching probabilities that have been discussed earlier have no explicit time dependence, then time would not be a good variable to control the particle evolution process. However, those probabilities depend on the virtualities of the involved splitting, and thus one can invent another variable t that is directly related to the virtuality to play to role of ‘time’. For now we want this new variable t to have the property that at the beginning of the evolution, which is also the product of the hardest interaction, t is equal to zero; and the particles would stop splitting when t reaches a certain cutoff value t_f . To satisfy the above conditions, in QCD, one can define

$$t \equiv \log \frac{q_0^2}{q^2}, \quad (2.50)$$

where q_0^2 describes the virtualities of the hardest quarks and gluons given by the hard matrix elements, and q^2 is the virtuality of the current splitting. This way, at the beginning of the evolution, the ‘shower time’ is tuned to be zero; and as the time-like branchings move on, the virtuality scales would drop, while the corresponding

“shower time” would increase until it hits the cutoff value. But for the purpose of the discussion here where the interaction only involves one type of massless scalar particles, there is another way to define the variable t . In the splitting $l \rightarrow i + j$ we can choose

$$t \equiv \log \frac{Q_0^2}{2p_i \cdot p_j} \quad (2.51)$$

where Q_0^2 is the virtuality scale at which the shower starts.

Now if at a certain stage of ‘shower time’ t of the parton evolution we write down the cross section of having m particles with momenta $\{p\}_m$ as $\rho(\{p\}_m, t)$, then the total cross section of present ‘shower time’ can be expressed in terms of function ρ ,

$$\sigma_T(t) = \sum_m \frac{1}{m!} \int [d\{p\}_m] \rho(\{p\}_m, t) . \quad (2.52)$$

More generally, if the measurement function is not just equal to 1, at the cutoff “shower time” t_f , one would instead have

$$\sigma[F] = \sum_m \frac{1}{m!} \int [d\{p\}_m] \rho(\{p\}_m, t_f) F(\{p\}_m) . \quad (2.53)$$

Before we proceed, it will be helpful to set up a formalism (adapted from [13]) now for the discussion later. Define a certain vector space of functions, where a certain state $|G(t)\rangle$ (or $\langle G(t)|$) corresponds to a group of functions at a chosen t , which describes the same property of an event regardless of its momentum configuration. For example, $\langle F|$ corresponds to the collection of functions $F(\{p\}_m)$ (we drop the argument t because measurement functions are generally independent of t), and the state $|\rho(t)\rangle$ corresponds to the collection of cross sections $\rho(\{p\}_m, t)$ at a certain “shower time” t . Furthermore, the inner product of the vector space can be defined to be

$$\langle A|B\rangle \equiv \sum_m \frac{1}{m!} \int [d\{p\}_m] A(\{p\}_m) B(\{p\}_m) . \quad (2.54)$$

Define a complete set of orthogonal basis vectors $|\{p\}_n\rangle$ such that they would have the following property:

$$\langle \{p\}_n | \rho(t) \rangle = \rho(\{p\}_n, t) , \quad (2.55)$$

with the completeness relation

$$1 = \sum_m \frac{1}{m!} \int [d\{p\}_m] |\{p\}_m\rangle \langle\{p\}_m| . \quad (2.56)$$

Obviously, any measurement function F can correspond to a vector $\langle F|$, and thus the cross section of the observable at the final stage would be

$$\sigma [F] = \langle F|\rho(t_f) \rangle . \quad (2.57)$$

There is a special state which corresponds to a function that gives all final state the same value, 1, and let us name that state $\langle 1|$ whose inner product with the state $|\rho(t)\rangle$ gives us the total cross section at a certain stage

$$\sigma_T = \langle 1|\rho(t) \rangle . \quad (2.58)$$

A non-trivial example of $\langle F|$ is $\langle N > 5|$, and it corresponds to any function that returns 1 for events with more than 5 final state particles and returns 0 otherwise. Therefore,

$$\sigma_{N>5} = \langle N > 5|\rho(t) \rangle \quad (2.59)$$

would be the cross section of having at least 5 partons in the final state at t .

By now, the problem of figuring out how the final state partons evolve has become the task of studying the ‘shower time’ evolution operator that acts on the state $|\rho(t)\rangle$. Typically one would start with a defined number of particles. For example, if we pick an initial state $|\rho(0)\rangle$ such that the event has only 2 particles at $t = 0$, then we would have $\langle\{p\}_2|\rho(0)\rangle \neq 0$ but $\langle\{p\}_m|\rho(0)\rangle = 0$ for any $m > 2$. Obviously, $\langle\{p\}_2|\rho(0)\rangle$ is the Born level cross section. After evolving this state to the cut-off scale t_f , we would obtain the final state $|\rho(t_f)\rangle$, which we can use to calculate the final-state cross section at that scale.

Define the evolution operator to be $\mathcal{U}(t, t')$, and

$$|\rho(t)\rangle = \mathcal{U}(t, t') |\rho(t')\rangle . \quad (2.60)$$

It could also have the group composition property,

$$\mathcal{U}(t_3, t_1) = \mathcal{U}(t_3, t_2) \cdot \mathcal{U}(t_2, t_1) . \quad (2.61)$$

Intuitively thinking, if such operator acts on a certain state, the effects should be either some particles in that state split into more particles, or nothing happens at all. Then a reasonable guess would be the evolution operator consists of two parts, one would leave the state untouched with a certain probability, and another make the state become another state by making particles fragment, also with some probability. Let us look at the latter part first. For this purpose, an infinitesimal generator of evolution, $\mathcal{H}(t)$, is needed. At the lowest order, when it acts on an arbitrary state, $\mathcal{H}(t) |\rho(t)\rangle$, it makes one particle l in the original state split into two other particles, with momenta \hat{p}_l and \hat{p}_{m+1} respectively. In this model involving only one type of massless scalar particles, the matrix element after the splitting is

$$\mathcal{M}(\{p\}_{m+1}) \approx \mathcal{M}(\{p\}_m) \cdot \frac{g}{2\hat{p}_l \cdot \hat{p}_{m+1}} , \quad (2.62)$$

where g is the coupling constant of the interaction. But in order to make the above equation approximately right, one condition has to be satisfied that the splitting happens in the collinear limit, because only when the splitting is nearly collinear can one find a momentum $p_l \approx \hat{p}_l + \hat{l}_{m+1}$ while nevertheless on shell, $p_l^2 = 0$, which would not change the momentum configuration in the smaller diagram much. In fact the approximated factorization of the bigger diagram \mathcal{M}_{m+1} is the key to developing an algorithm of parton showers. For a statistical splitting function, one needs to square the quantum amplitudes above. For QCD, the splitting function at a certain scale of hardness or virtuality has already been worked out in the previous sections. The projection of the state $|\rho(t)\rangle$ on to the basis vector $|\{p\}_{m+1}\rangle$ after the operation of the Hamiltonian $\mathcal{H}(t)$, or in other words, the cross section $\rho(\{p\}_{m+1}, t)$ of the final state, is now approximately a sum of the cross sections of m final state particles

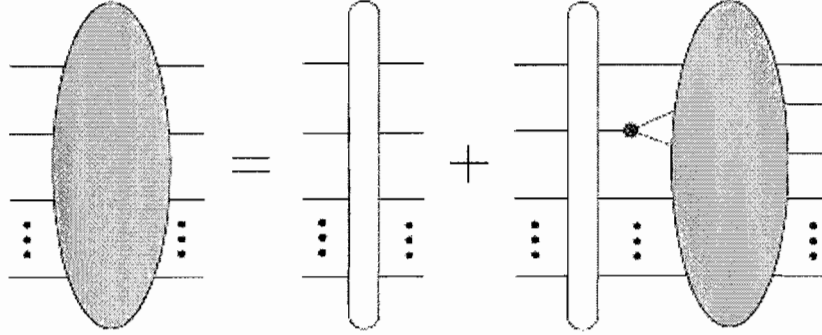


FIGURE 2.8: Illustration of the effects of evolution operator. This figure is provided by [13].

multiplied by probabilities for different particles to split:

$$(\{p\}_{m+1} | \mathcal{H}(t) | \rho) \approx \sum_l \delta \left(t - \log \frac{Q_0^2}{2\hat{p}_l \cdot \hat{p}_{m+1}} \right) \left(\frac{g}{2\hat{p}_l \cdot \hat{p}_{m+1}} \right)^2 (\{p\}_m | \rho) . \quad (2.63)$$

The δ function has been inserted which shows the evolution is at ‘shower time’ t . And now the choice of t here in this model seems quite natural based on the form of the statistical splitting function.

The other part of the evolution operator $\mathcal{U}(t', t)$ that leaves the particle number and momentum configuration of any state unchanged can be written as $\mathcal{N}(t', t)$. It should also have the group composition property

$$\mathcal{N}(t_3, t_1) = \mathcal{N}(t_3, t_2) \cdot \mathcal{N}(t_2, t_1) . \quad (2.64)$$

Other than that, when it acts on the basis vectors, the resulting states are still the same basis vectors, but could have a new multiplicative constant, or one could say, the basis vectors are in fact this no-change operator’s eigenvectors,

$$\mathcal{N}(t', t) |\{p\}_m) = \Delta(t', t; \{p\}_m) |\{p\}_m) . \quad (2.65)$$

The physical meaning of the eigenvalue will be given later.

It is time to write down the complete form of the statistical evolution operator,

$$\mathcal{U}(t_3, t_1) = \mathcal{N}(t_3, t_1) + \int_{t_1}^{t_3} dt_2 \mathcal{U}(t_3, t_2) \mathcal{H}(t_2) \mathcal{N}(t_2, t_1) , \quad (2.66)$$

which can be interpreted in the following way, as briefly mentioned earlier: when the evolution operator \mathcal{U} acts on a statistical state, it will either evolve the state without any splitting during the entire period of ‘shower time’ from $t_1 \rightarrow t_3$, or evolve it without splitting for a while, and at some point t_2 make some particle in the state split, and then after the splitting evolve it normally with or without splitting to t_3 . However, neither the probability of an arbitrary state evolving without any splitting nor the probability of the state splitting at least once during the evolution is clear in the above equation.

To find out about the probabilities of different ways of evolution, one can study the quantity $(1|\mathcal{U}(t', t)|\rho(t))$, the total cross section after the parton evolution. A sensible convention would be the one in which the total cross section of any studied process remain the same throughout the evolution, thus

$$\sigma_T = (1|\rho(t)) = (1|\mathcal{U}(t', t)|\rho(t)) , \quad (2.67)$$

and since the above relation is true for any state $|\rho\rangle$, the only possibility is the evolution operator always has the property that

$$(1|\mathcal{U}(t', t) \equiv (1| . \quad (2.68)$$

As a result, if one multiply the state $|\rho(t_1)\rangle$ to the right and $(1|$ to the left on both sides of the Eq.(2.66),

$$\begin{aligned} (1|\mathcal{U}(t_3, t_1)|\rho(t_1)) &= (1|\mathcal{N}(t_3, t_1)|\rho(t_1)) + \\ &\quad + \int_{t_1}^{t_3} dt_2 (1|\mathcal{U}(t_3, t_2)\mathcal{H}(t_2)\mathcal{N}(t_2, t_1)|\rho(t_1)) \\ \Downarrow \\ \sigma_T(t_3) &= \sum_m \frac{1}{m!} \int [d\{p\}_m] \left[\Delta(t_3, t_1; \{p\}_m) \rho(\{p\}_m, t_1) \right] + \\ &\quad + \sum_m \frac{1}{m!} \int [d\{p\}_m] \left[\int_{t_1}^{t_3} dt_2 (1|\mathcal{H}(t_2)|\{p\}_m) \Delta(t_2, t_1; \{p\}_m) \rho(\{p\}_m, t_1) \right] , \end{aligned} \quad (2.69)$$

and based upon the last equation from a classic statistical point of view, one should interpret $(1|\mathcal{H}(t)|\{p\}_m)$ as the total probability for one of the particles in state $\{p\}_m$ splitting at ‘shower time’ t . And $\Delta(t', t; \{p\}_m)$ should be explained as the probability for the state to evolve from $t \rightarrow t'$ without splitting at all, known as the *Sudakov factor*. By using the fact that total cross section does not change as the state of partons develop, one can equate Eq. (2.69) to the expression for total cross section defined in Eq. (2.52) at time t_1 in terms of $\rho(\{p\}_m, t_1)$, and get

$$1 = \Delta(t_3, t_1; \{p\}_m) + \int_{t_1}^{t_3} dt_2 (1|\mathcal{H}(t_2)|\{p\}_m) \Delta(t_2, t_1; \{p\}_m) . \quad (2.70)$$

By taking the derivative of the last equation with respect to t_3 , one could get

$$\frac{d}{dt_3} \Delta(t_3, t_1; \{p\}_m) = - (1|\mathcal{H}(t_3)|\{p\}_m) \Delta(t_3, t_1; \{p\}_m) , \quad (2.71)$$

and solving this equation gives us

$$\Delta(t_3, t_1; \{p\}_m) = \exp\left(-\int_{t_1}^{t_3} dt_2 (1|\mathcal{H}(t_2)|\{p\}_m)\right) . \quad (2.72)$$

Now come back to Eq. (2.69) again. Until now, one might still think at a given hardness scale, the probability of one particle splitting in the state $|\{p\}_m\rangle$ is $(1|\mathcal{H}(t)|\{p\}_m)$, the counterpart of which in LO QCD calculation is the sum of splitting functions \hat{P}_{gg} , \hat{P}_{qg} and \hat{P}_{gq} over all particles that could split in the same state. However, Eq. (2.69) implies the actual probability of splitting is in fact the Sudakov exponential factor times the appropriate splitting function. Strictly speaking,

$$P(t_2) \equiv F(t_2) \cdot \exp\left(-\int_{t_1}^{t_2} F(\tau) d\tau\right) . \quad (2.73)$$

Many parton splitting functions are singular when the branching is collinear, and it seems to endanger the whole picture of parton fragmentation. But the Sudakov exponential could successfully suppress parton splitting in the infrared region, and hence solves the potential problem of unphysical singular behavior.

2.4.4 Implementation

Having introduced the formulation of parton evolution, one can start asking the question of how to write a computer program to simulate the parton splitting process. Here we will first talk about the general idea of a branching algorithm, and then elaborate on some much more sophisticated methods that have been used by BEOWULF [14].

2.4.4.1 Generating Splitting Info Based on Given Distributions

Given the initial conditions including the hardness scales and momentum fractions of the first few partons, the first step is to make use of the Sudakov exponential to get the right hardness scale of the next possible branching [10]. As we already know, $\Delta(t_2, t_1)$ tells about the probability of a parton not to split between the two hardness scales t_1 and t_2 , and is always a number between 0 and 1. If we get the shower time t_1 for the initial parton by translating from the hardness scale, and want to find out what value t_2 should take, we could let the program to generate a uniformly distributed random number $\mathcal{R} \in (0, 1)$, and then solve the equation below for t_2 :

$$\Delta(t_2, t_1) = \mathcal{R} . \tag{2.74}$$

The resulting t_2 can be translated back to a hardness scale where the next splitting will be taking place. But would t_2 have the correct distribution in that way? Take an arbitrary R , and assume $t_2(R)$ is the solution to Eq (2.74). Apparently the probability $p(\mathcal{R})$ of generating a random number smaller than \mathcal{R} would just be \mathcal{R} itself, and hence the probability for the solution t_2 to be bigger than $t_2(\mathcal{R})$ will also be \mathcal{R} . In other words, the probability for the algorithm not to split a parton between t_1 and $t_2(\mathcal{R})$ is exactly $\Delta(t_2(\mathcal{R}), t_1)$, just as what Sudakov exponential is defined to represent.

Once we have acquired the hardness scale of the next branching, we still have to generate the momentum fraction x of the daughter partons with respect to the mother

parton. Eq (2.47) implies $(\alpha_S/2\pi)\hat{P}(z)$ should be the appropriately normalized probability density for the initial parton of momentum p to split into two other partons that have momenta xp and $(1-x)p$ respectively. Similar to what we have done to generate the right splitting scales, a different and totally independent random number \mathcal{R}' , which can again be equally possible be any real number between 0 and 1, is going to be fed into the following equation:

$$\mathcal{R}' = \frac{\int_{\epsilon}^x dz \frac{\alpha_S}{2\pi} \hat{P}(z)}{\int_{\epsilon}^{1-\epsilon} dz \frac{\alpha_S}{2\pi} \hat{P}(z)}, \quad (2.75)$$

where the integration start from an infinitesimal positive number ϵ instead of 0 because $\hat{P}(z)$ could be singular at $z = 0$ or $z = 1$. If we always choose x to be the solution of the above equation, we will end up with the distribution of momentum fraction suggested by those Alterelli-Parisi splitting functions.

2.4.4.2 Rejection Sampling

In practice given a distribution of shower time, or virtuality, suppressed by a Sudakov exponential, it is usually difficult to solve Eq (2.74) either numerically or by hand, due to a complicated integral in the exponent. As a consequence, BEOWULF makes use of an technique called *Rejection Sampling* [15] to generate splitting virtualities only indirectly. The simplest algorithm of this type was first found by John von Neumann, and it requires the capability of generating random numbers according to a proposed “blanket” distribution. For example, in order to generate x from a wanted distribution, $p(x)$, one needs an appropriate sampling distribution, $g(x)$, for which one can straightforwardly solve a corresponding equation similar to Eq (2.74). This instrumental distribution also has to satisfy another condition that there should exist a constant $M > 1$ for which $f(x) < Mg(x)$. The algorithm is as follows:

- (1) Sample x from $g(x)$ and u from a uniform distribution in $[0, 1]$;

(2) See if $u < f(x)/Mg(x)$ is true:

a) If true, accept x as a successfully sampled point;

b) If false, reject x and repeat the algorithm from step (1).

Random points selected by the above algorithm will have the right distribution $f(x)$, and this can be proved using a graphical argument called *the envelope principle*. It says when points are sampled from $g(x)$, they can fill the area under the curve $Mg(x)$. By accepting and rejecting points according to the inequality $u < f(x)/Mg(x)$, the selected points should be able to uniformly occupy a sub-area which is right under the curve $f(x)$, or in other words, those points have been sampled according to the distribution $f(x)$.

In BEOWULF, a more complicated version of Rejection Sampling is used when generating the virtualities of splittings, which will be discussed later, together with a technique to produce the splitting angle and momentum fractions of daughter partons without solving the awkward Eq (2.75).

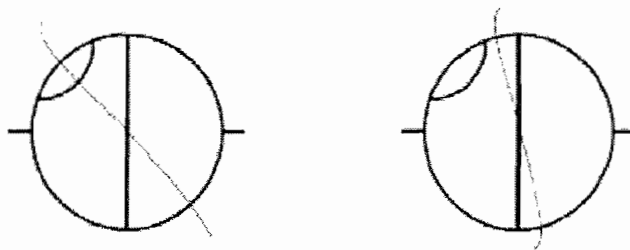


FIGURE 2.9: Example: a pair of NLO graphs that contributes to unphysical divergences in the prediction of some observables. This figure is provided by [2].

2.5 Adding Parton Showers

2.5.1 Motivation

To simplify the problem, we can choose to calculate 3-jet observables that describe the final states of a certain scattering process. Since those observables will almost always vanish for events with only 2 jets, we just need to take account of all LO and NLO Feynman graphs that have either 3 or 4 partons in the final state, so that the calculations of 3-jet observables can be carried on to the next-to-leading order. To remind ourselves of what went wrong with the pure NLO calculation, we can take a look at the two graphs in Fig. 2.9. Both graphs have infrared divergences, but since those divergences can always cancel each other, there would be no problem when one calculates the total cross section. However, things can become messy when differential cross sections are considered. Every time a typical pure NLO Monte Carlo program process a Feynman graph, it will eventually generate a corresponding event based on the momentum flow in that same graph, along with a weight given by the value of the cut diagram. So the two graphs in Fig. 2.9 will give two groups of events, one with 3 partons in the final state and the other with 4 partons. When calculating differential cross sections, events from different groups will probably be categorized into different bins of some observable, and a situation like this will endanger the

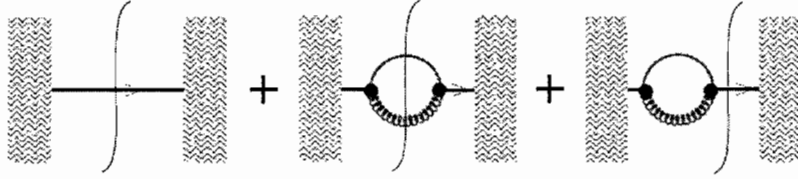


FIGURE 2.10: Three types of cut propagators in the case of a quark splitting into another quark and a gluon. This figure is provided by [2].

cancellation of infrared divergences between events from different groups, which will manifest itself as the weights of events.

The detailed analysis provided in the last paragraph also suggest a way of solving the problem [2]. If we can somehow generate a single event with the effects of both graphs in Fig. 2.9 included in a single weight accompanying this event, the cancellation of infrared divergences would be able to work properly even if we are dealing with differential cross sections. Any detail of the solution will depend on the calculation of those Feynman diagrams we are interested, so it is worthwhile to take a look at which part of those graphs are responsible for the infrared divergences and how exactly the cancellation works out. The explanation will follow the recipe given by [2].

Fig. 2.10 displays three different types of cut propagators, and those wavy lines near the propagators represent the remaining parts of the Feynman diagrams plus measurement functions. We will see very soon that they are combined to describe how a quark or anti-quark would split into another quark and a gluon. The first diagram has the Born level cut propagator, and its amplitude can be derived by straight forward use of Feynman rules:

$$\mathcal{I}[\text{Born}] = \int \frac{d\vec{q}}{2|\vec{q}|} \text{Tr} \{ \not{q} R_0 \} , \quad (2.76)$$

where q is the on-shell momentum of the cut quark propagator, and R_0 denotes factors of the rest of the diagram and measurement functions.

The second diagram has a virtual loop, and both loop momenta are put on shell. The cut propagator of this kind is called a cut self-energy diagram, with the value of the whole Feynman graph given by

$$\mathcal{I}[\text{real}] = \int \frac{d\vec{q}}{2|\vec{q}|} \text{Tr} \left\{ \int_0^\infty \frac{d\bar{q}^2}{\bar{q}^2} \int_0^1 dx \int_{-\pi}^\pi \frac{d\phi}{2\pi} \frac{\alpha_s}{2\pi} \mathcal{M}_{g/q}(\bar{q}^2, x, \phi) R(\bar{q}^2, x, \phi) \right\}. \quad (2.77)$$

In the above expression, there are integrations over a set of coordinates, $\{\bar{q}^2, x, \phi\}$, of the loop momentum. We will first define all those three variables. If we use \vec{k}_+ and \vec{k}_- to represent the 3-momentum of the gluon and the quark after the splitting separately, we would have $\vec{k}_+ + \vec{k}_- = \vec{q}$. The virtuality of the splitting \bar{q}^2 , and the momentum fraction of the gluon after the splitting are defined as

$$\begin{aligned} \sqrt{1 + \bar{q}^2/|\vec{q}|^2} &= \left(|\vec{k}_+| + |\vec{k}_-| \right) / |\vec{q}| \\ 2x - 1 &= \left(|\vec{k}_+| - |\vec{k}_-| \right) / |\vec{q}|. \end{aligned} \quad (2.78)$$

Obviously $\bar{q}^2 > 0$ and $0 < x < 1$. The third coordinate ϕ is defined to be the angle between \vec{k}_+ and \vec{q} . The function $(2\pi)\mathcal{M}_{g/q}(\bar{q}^2, x, \phi)$ is calculated by using Feynman rules in the Coulomb gauge, and it has an interesting infrared limit:

$$\frac{\alpha_s}{2\pi} \mathcal{M}_{g/q}(\bar{q}^2, x, \phi) \longrightarrow \frac{\alpha_s}{2\pi} \not{q} \hat{P}_{g/q}(x) \quad \text{as } \bar{q}^2 \rightarrow 0. \quad (2.79)$$

It is not difficult to convince ourselves that $\hat{P}_{g/q}$ here should in fact be the same function that has already been defined in Eq. (2.38), except we name that function as \hat{P}_{qq} over there, and also the argument there is z , the momentum fraction of the quark, instead of what we are using here, x , the momentum fraction of the gluon. So by replacing z with $(1-x)$ in Eq. (2.38) one could get the Altarelli-Parisi kernel of the unregularized quark splitting function

$$\hat{P}_{g/q}(x) = C_F \frac{1 + (1-x)^2}{x}. \quad (2.80)$$

Meanwhile, if normalization is chosen properly, the function $R(\bar{q}^2, x, \phi)$ should have the infrared behavior as shown below:

$$R(\bar{q}^2, x, \phi) \longrightarrow R_0 \quad \text{as } \bar{q}^2 \rightarrow 0. \quad (2.81)$$

The third Feynman graph in Fig. 2.10 also has a virtual loop, but this time only the momentum of the quark before the splitting is put on shell. Again we can derive the amplitude of this virtual self-energy graph from Feynman rules:

$$\mathcal{I}[\text{virtual}] = \int \frac{d\vec{q}}{2|\vec{q}|} \text{Tr} \left\{ - \int_0^\infty \frac{d\vec{q}^2}{\vec{q}^2} \int_0^1 dx \int_{-\pi}^\pi \frac{d\phi}{2\pi} \frac{\alpha_s}{2\pi} \mathcal{P}_{g/q}(\vec{q}^2, x) \not{q} R_0 \right\}, \quad (2.82)$$

where the function $(\alpha_s/2\pi) \mathcal{P}(\vec{q}^2, x)$ has a similar infrared limit as the cut self-energy function,

$$\frac{\alpha_s}{2\pi} \mathcal{P}_{g/q}(\vec{q}^2, x) \longrightarrow \frac{\alpha_s}{2\pi} \hat{P}_{g/q}(x) \quad \text{as } \vec{q}^2 \rightarrow 0. \quad (2.83)$$

Since in the infrared region both $\mathcal{M}_{g/q}$ and $\mathcal{P}_{g/q}$ approach some function independent of the virtuality, the integrals over \vec{q}^2 in $\mathcal{I}[\text{real}]$ and $\mathcal{I}[\text{virtual}]$ will produce logarithmic divergences. But note those integrals have opposite signs in front of them, which makes the sum of all 3 amplitudes free of infrared singularities. However, as we mentioned earlier, events coming from graph 2 and 3 might go into different bins because their amplitudes are coupled to different measurement functions. To compress all information from Fig. 2.10 into one single event, we first sum over different amplitudes:

$$\begin{aligned} \mathcal{I}[\text{Born}] + \mathcal{I}[\text{real}] + \mathcal{I}[\text{virtual}] = \int \frac{d\vec{q}}{2|\vec{q}|} \text{Tr} \left\{ \not{q} R_0 + \int_0^\infty \frac{d\vec{q}^2}{\vec{q}^2} \int_0^1 dx \int_{-\pi}^\pi \frac{d\phi}{2\pi} \right. \\ \left. \left[\frac{\alpha_s}{2\pi} \mathcal{M}_{g/q}(\vec{q}^2, x, \phi) R(\vec{q}^2, x, \phi) - \frac{\alpha_s}{2\pi} \mathcal{P}_{g/q}(\vec{q}^2, x) \not{q} R_0 \right] \right\}. \end{aligned} \quad (2.84)$$

To proceed, one can identify the cut self-energy function $\mathcal{M}_{g/q}(\vec{q}^2, x, \phi)$ as the probability density for a quark to split into another quark and a gluon. And if the first and the third term in Eq.(2.84) are grouped together, with $\not{q} R_0$ factored out, which describes the rest of the graph and measurement functions, apparently the probability density of the quark evolving without splitting can be found to be $\left(1 - \frac{\alpha_s}{2\pi} \mathcal{P}_{g/q}(\vec{q}^2, x)\right)$. If exponentiating this second probability density, one can end up with a Sudakov factor, with $\frac{\alpha_s}{2\pi} \mathcal{P}_{g/q}(\vec{q}^2, x)$ as the exponent. We can follow the spirit of classical statistics and write down a function which might hopefully include

the effects of all three types of cut quark propagators. Analogous to Eq.(2.73), one can write down

$$\begin{aligned} \mathcal{I}[\text{shower}] = \int \frac{d\vec{q}}{2|\vec{q}|} \text{Tr} \left\{ \int_0^\infty \frac{d\vec{q}^2}{\vec{q}^2} \int_0^1 dx \int_{-\pi}^\pi \frac{d\phi}{2\pi} \frac{\alpha_s}{2\pi} \mathcal{M}_{g/q}(\vec{q}^2, x, \phi) R(\vec{q}^2, x, \phi) \right. \\ \left. \cdot \exp \left(- \int_{\vec{q}^2}^\infty \frac{d\vec{l}^2}{\vec{l}^2} \int_0^1 dz \frac{\alpha_s}{2\pi} \mathcal{P}_{g/q}(\vec{l}^2, z) \right) \right\}. \end{aligned} \quad (2.85)$$

By carefully expanding $\mathcal{I}[\text{shower}]$ in powers of α_s , one can actually prove

$$\mathcal{I}[\text{shower}] = \mathcal{I}[\text{Born}] + \mathcal{I}[\text{real}] + \mathcal{I}[\text{virtual}] + \mathcal{O}(\alpha_s^2), \quad (2.86)$$

and since for now it is only necessary to maintain the NLO accuracy, we are free to replace the right-hand side of the above equation in any pure NLO program with this new shower amplitude according to some specific procedures, which only has one type of measurement function. The motivation for doing this has been elaborated at the beginning of this section. We can also develop an analog for the cut propagator. Similarly, the functions involved will approach Altarelli-Parisi splitting functions in the infrared limit.

To actually incorporate the above idea into a typical pure NLO program, one needs to first generate 3 partons according to appropriate distributions calculated from Born level Feynman graphs. The 3 partons will further split into 6 partons. The momentum distribution and virtuality scale of this process, called primary splitting, should be governed by the cut self-energy function $\mathcal{M}(\vec{q}^2, x, \phi)$ and the Sudakov factor with the virtual self-energy function in the exponent, respectively. Meanwhile, we should carefully avoid including the same NLO effects in the final-state measurements twice, through replacing each pair of $(\mathcal{I}[\text{real}] + \mathcal{I}[\text{virtual}])$ by 0 when calculating next-to-leading order cut graphs. An example of this procedure is given for one of the Born graph in Fig 2.11 and Fig 2.12, and Fig 2.12 specifically shows the corresponding NLO graphs that have to be turned off after adding the primary showers.

In practice, one might want to use something slightly different from $\mathcal{I}[\text{shower}]$. Since the factorization of parton branching vertex from the rest of a Feynman diagram

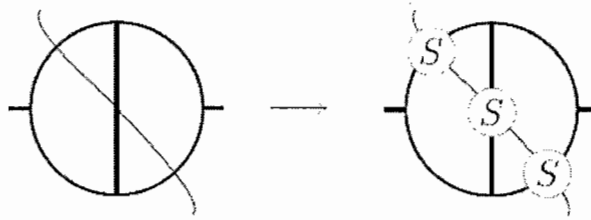


FIGURE 2.11: Replacing cut born propagator with a shower propagator. This figure is provided by [2].

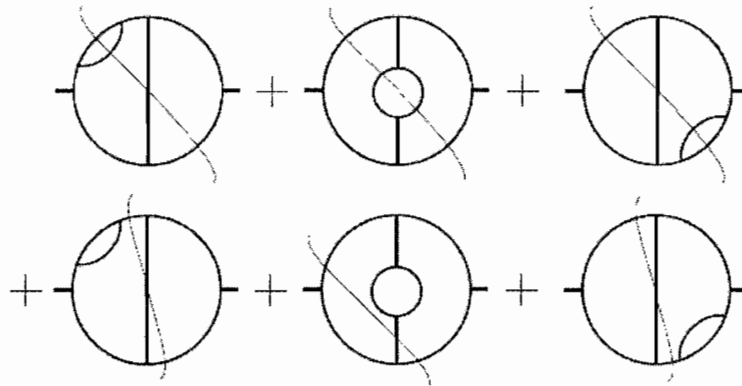


FIGURE 2.12: Deleting redundant cut NLO graphs due to the use of shower functions. This figure is provided by [2].

is a good approximation only in the collinear region, it makes more sense if we cut off parton splitting at a certain small scale so that the assumption of factorization will not be violated when the program is processing primary showers, and put back whatever pieces that have been missing from the modified shower algorithm, in the form of ordinary cut α_s^2 propagators. In detail, one can rewrite $\mathcal{I}[\text{shower}]$ as

$$\begin{aligned} \mathcal{I}[\text{shower}, \lambda_V] = \int \frac{d\vec{q}}{2|\vec{q}|} \text{Tr} \left\{ \int_0^{\lambda_V \bar{q}^2} \frac{d\bar{q}^2}{\bar{q}^2} \int_0^1 dx \int_{-\pi}^{\pi} \frac{d\phi}{2\pi} \frac{\alpha_s}{2\pi} \mathcal{M}_{g/q}(\bar{q}^2, x, \phi) \right. \\ \left. \cdot R(\bar{q}^2, x, \phi) \exp \left(- \int_{\bar{q}^2}^{\infty} \frac{d\bar{l}^2}{\bar{l}^2} \int_0^1 dz \frac{\alpha_s}{2\pi} \mathcal{P}_{g/q}(\bar{l}^2, z) \right) \right\}, \end{aligned} \quad (2.87)$$

where $\lambda_V \bar{q}^2$ becomes the upper limit of the integration over the virtuality \bar{q}^2 of the primary splitting instead of ∞ in the original definition, and thus we would have a corresponding leftover NLO piece to calculate, too:

$$\begin{aligned} \mathcal{I}[\text{real}, \lambda_V] = \int \frac{d\vec{q}}{2|\vec{q}|} \text{Tr} \left\{ \int_{\lambda_V \bar{q}^2}^{\infty} \frac{d\bar{q}^2}{\bar{q}^2} \int_0^1 dx \int_{-\pi}^{\pi} \frac{d\phi}{2\pi} \frac{\alpha_s}{2\pi} \mathcal{M}_{g/q}(\bar{q}^2, x, \phi) \right. \\ \left. \cdot R(\bar{q}^2, x, \phi) \right\}. \end{aligned} \quad (2.88)$$

It can be easily proved the NLO accuracy will be intact if we include both $\mathcal{I}[\text{shower}, \lambda_V]$ and $\mathcal{I}[\text{real}, \lambda_V]$ when modifying the primary shower algorithms.

2.5.2 Implementation

In original BEOWULF, a slightly different shower function is used to split Born graph partons [2]. For example, a gluon is split into two other partons according to

$$\begin{aligned} \tilde{\mathcal{I}}[\text{shower}, \lambda_V] = \int \frac{d\vec{q}}{2|\vec{q}|} \text{Tr} \left\{ \int_0^{\lambda_V \bar{q}^2} \frac{d\bar{q}^2}{\bar{q}^2} \int_0^1 dx \int_{-\pi}^{\pi} \frac{d\phi}{2\pi} \frac{\alpha_s}{2\pi} \tilde{\mathcal{M}}_g^{\mu\nu}(\bar{q}^2, x, \phi) \right. \\ \left. \cdot R_{\mu\nu}(\bar{q}^2, x, \phi) \exp \left(- \int_{\bar{q}^2}^{\infty} \frac{d\bar{l}^2}{\bar{l}^2} \int_0^1 dz \frac{\alpha_s}{2\pi} \mathcal{P}_g(\bar{l}^2, z) \right) \right\}, \end{aligned} \quad (2.89)$$

where the trace is taken over Lorentz indices now, unlike the quark splitting case. In order to preserve the NLO accuracy of the calculation, in addition to replacing $\mathcal{I}[\text{Born}]$ with $\tilde{\mathcal{I}}[\text{shower}, \lambda_V]$, one also has to replace $\mathcal{I}[\text{real}]$ and $\mathcal{I}[\text{virtual}]$ by

\mathcal{I} [real, λ_V] plus an infrared piece

$$\mathcal{I}[\text{subtraction}, \lambda_V] = \int \frac{d\vec{q}}{2|\vec{q}|} \text{Tr} \left\{ \int_0^{\lambda_V \bar{q}^2} \frac{d\bar{q}^2}{\bar{q}^2} \int_0^1 dx \int_{-\pi}^{\pi} \frac{d\phi}{2\pi} \frac{\alpha_s}{2\pi} R_{\mu\nu}(\bar{q}^2, x, \phi) \right. \\ \left. \cdot \left[\mathcal{M}_g^{\mu\nu}(\bar{q}^2, x, \phi) - \widetilde{\mathcal{M}}_g^{\mu\nu}(\bar{q}^2, x, \phi) \right] \right\}. \quad (2.90)$$

$\mathcal{M}_g^{\mu\nu}$ is the one-loop real gluon self-energy function calculated in Coulomb gauge, and the loop could be either a gluon loop, or a quark loop running over all possible flavors. In detail, it is a sum of four tensors [7],

$$\mathcal{M}_g^{\mu\nu} = \frac{\alpha_s}{4\pi} \frac{1}{1+\Delta} \times \left\{ N_{TT} D(\mathcal{Q}, \vec{q})^{\mu\nu} \right. \\ \left. + N_{tt} \left[\frac{l_T^\mu l_T^\nu}{l_T^2} - \frac{1}{2} D(\mathcal{Q}, \vec{q})^{\mu\nu} \right] + \frac{\bar{q}^2}{Q^2} N_{EE} n^\mu n^\nu \right. \\ \left. + N_{Et} \frac{\vec{q} \cdot n}{(1+\Delta) Q^2} (l_T^\mu n^\nu + n^\mu l_T^\nu) \right\}, \quad (2.91)$$

where $1/(1+\Delta)$ is a normalization factor ($\Delta \equiv \sqrt{1+\bar{q}^2/Q^2} - 1$), coefficients N_{TT} , N_{tt} , N_{EE} and N_{Et} are functions of virtuality \bar{q}^2 and momentum fraction x , and the tensor $D(\mathcal{Q}, \vec{q})^{\mu\nu}$ is the numerator of a bare on-shell gluon propagator with momentum (\mathcal{Q}, \vec{q}) , of which in the convention used here the only nonzero components are $D(\mathcal{Q}, \vec{q})^{ij} = \delta^{ij}$ with $i, j \in \{1, 2\}$. Among those coefficients, N_{tt} and N_{Et} are of less interest to us because they will vanish after integrating over angles; N_{EE} will not be written down here, either, since we are just interested in the $\bar{q}^2 \rightarrow 0$ limit, for which the reason will be given later. Now if we take this infrared limit, while ignoring the coefficients mentioned above, we can obtain something similar to Eq. (2.79),

$$\mathcal{M}_g^{\mu\nu} \longrightarrow D(q)^{\mu\nu} \frac{\alpha_s}{2\pi} \left\{ \frac{1}{2} \hat{P}_{g/g}(x) + N_F \hat{P}_{q/g}(x) \right\}, \quad (2.92)$$

where $\hat{P}_{g/g}$ and $\hat{P}_{q/g}$ are the one loop parton evolution kernels as defined in Sec. 2.4.2. So the real gluon self-energy function we just gave does have the right behavior when $\bar{q}^2 \rightarrow 0$.

However, a different function $\widetilde{\mathcal{M}}_g^{\mu\nu}$ has been chosen to split the Born-level partons, and one can obtain this function by replacing N_{TT} with the simplified one-loop virtual

gluon self-energy function $\mathcal{P}_g(\bar{q}^2, x)$ (the exact form is given in [7]), and replacing N_{EE} with 0 in the real gluon self-energy function, as defined in Eq. (2.91). Based on the explicit form of the virtual gluon self-energy function one can prove the following to be true:

$$\mathcal{P}_g(0, x) = \frac{1}{2}\hat{P}_{g/g}(x) + N_F\hat{P}_{q/g}(x) . \quad (2.93)$$

We will argue now the newly defined $\widetilde{\mathcal{M}}_g^{\mu\nu}$ is indeed a good candidate as a gluon splitting function. First of all, as implied by Eq. (2.90), which is a contribution from the NLO leftover piece, the two subtracting terms are coupled with the same measurement function. In pure NLO calculation, we also have a similar NLO subtraction, but there different terms are associated with different final states and thus when one needs to calculate differential cross sections, the infrared cancellation will not be able to work properly in a single bin. This problem has already been demonstrated in Fig 2.1. Secondly, by construction the remaining NLO contribution after we split Born-level partons using $\widetilde{\mathcal{M}}_g^{\mu\nu}$ is free of infrared divergences. Furthermore, the new splitting function satisfies the probability conservation. If one let the measurement function to be 1, then $\widetilde{\mathcal{I}}[\text{shower}, \lambda_V]$ of Eq. (2.89) gives the total cross section. In this case $R_{\mu\nu}$ only depends on the virtuality \bar{q}^2 , and after integrating over the angle ϕ we could obtain the probability density of gluon splitting to be

$$\sim \int_0^1 dx \frac{\alpha_s}{2\pi} \frac{1}{\bar{q}^2} \mathcal{P}_g(\bar{q}^2, x) \exp\left(-\int_{\bar{q}^2}^{\infty} \frac{d\bar{l}^2}{\bar{l}^2} \int_0^1 dz \frac{\alpha_s}{2\pi} \mathcal{P}_g(\bar{l}^2, z)\right) , \quad (2.94)$$

similar to Eq. (2.73).

Later we will see it is extremely difficult to generate splitting virtualities according to the probability density given in last paragraph. In BEOWULF a standard Rejection Sampling method is used, which is more sophisticated than the method discussed earlier in this thesis. In Coulomb gauge, one can analytically calculate the virtual

gluon self-energy function. We use the following notations [2] for convenience:

$$\begin{aligned}
D_x &= \bar{q}^2 / |\bar{q}|^2 + 4x(1-x) , \\
D_\mu &= \bar{q}^2 / \mu_{\text{mod}}^2 + 1 , \\
D_1 &= \bar{q}^2 / |\bar{q}|^2 + 1 ,
\end{aligned} \tag{2.95}$$

where μ is the $\overline{\text{MS}}$ renormalization scale, and

$$\mu_{\text{mod}}^2 \equiv \min(\mu^2, |\bar{q}|^2) . \tag{2.96}$$

For gluon splitting to a quark and antiquark, one finds [2]

$$\begin{aligned}
\mathcal{P}_{q/g}(\bar{q}^2, x) &= \frac{1}{2D_\mu} \{1 - 2x(1-x)\} + \frac{1}{2D_\mu^2} \frac{\bar{q}^2}{\mu_{\text{mod}}^2} \left\{ 2 - \frac{16}{3}x(1-x) \right. \\
&\quad \left. + \log(\mu^2 / \mu_{\text{mod}}^2) [1 - 2x(1-x)] \right\} .
\end{aligned} \tag{2.97}$$

For gluon splitting to two gluons, one finds

$$\begin{aligned}
\mathcal{P}_{g/g}(\bar{q}^2, x) &= \frac{C_A}{D_\mu} \{3x(1-x) - 1\} + \frac{C_A}{D_\mu^2} \frac{\bar{q}^2}{\mu_{\text{mod}}^2} \left\{ 7x(1-x) - 2 \right. \\
&\quad \left. + \log(\mu^2 / \mu_{\text{mod}}^2) [3x(1-x) - 1] \right\} \\
&\quad + \frac{12C_A}{D_x} x(1-x) \{1 - 2x(1-x)\} \\
&\quad + \frac{16C_A}{D_x^2} x(1-x) \{1 - 4x(1-x) + 4[x(1-x)]^2\}
\end{aligned} \tag{2.98}$$

The virtual gluon self-energy function is

$$\mathcal{P}_g(\bar{q}^2, x) = \mathcal{P}_{g/g}(\bar{q}^2, x) + N_F \mathcal{P}_{q/g}(\bar{q}^2, x) . \tag{2.99}$$

In Eq. (2.94), the integration of P_g over momentum fractions is straightforward to calculate, and it will be called P_{true} from now:

$$\begin{aligned}
P_{\text{true}}(\bar{q}^2) &\equiv \int_0^1 \mathcal{P}_g(\bar{q}^2, x) dx \\
&= \frac{1}{18} \frac{1}{D_\mu} (2N_F - 3C_A) \left(3 + \frac{8\bar{q}^2}{\mu_{\text{mod}}^2} \right. \\
&\quad \left. + 3 \log(\mu^2/\mu_{\text{mod}}^2) \frac{\bar{q}^2}{\mu_{\text{mod}}^2} \right) \\
&\quad - \frac{C_A}{6} \frac{1}{D_1} \left(5 + \frac{2\bar{q}^2}{\bar{q}^2} \right) \left(4 + \frac{3\bar{q}^2}{\bar{q}^2} \right) \\
&\quad + \frac{C_A}{4} \frac{1}{D_1^{3/2}} \left(2 + \frac{\bar{q}^2}{\bar{q}^2} \right) \log \left(\frac{\sqrt{D_1} + 1}{\sqrt{D_1} - 1} \right) \left(4 \right. \\
&\quad \left. + \frac{5\bar{q}^2}{\bar{q}^2} + 2 \left(\frac{\bar{q}^2}{\bar{q}^2} \right)^2 \right). \tag{2.100}
\end{aligned}$$

An auxiliary distribution is necessary to perform the Rejection Sampling algorithm, and for this purpose BEOWULF makes up

$$P_{\text{approx}} \equiv \begin{cases} b/\mu_{\text{mod}}^2 + 2C_A \log(\mu_{\text{mod}}^2/\bar{q}^2) & \text{if } \bar{q}^2 < \mu_{\text{mod}}^2 \\ b/\bar{q}^2 & \text{if } \bar{q}^2 \geq \mu_{\text{mod}}^2 \end{cases} \tag{2.101}$$

where b is defined as

$$b \equiv 1.1 \times \left[\frac{6C_A |\bar{q}|^2}{5} + \frac{\mu_{\text{mod}}^2}{18} (2N_F - 3C_A) \left(8 + 3 \log \left(\frac{\mu^2}{\mu_{\text{mod}}^2} \right) \right) \right], \tag{2.102}$$

and first sample points according to the probability density

$$Q_{\text{approx}}(\bar{q}^2, \infty) \equiv \frac{\alpha_s}{2\pi} \frac{1}{\bar{q}^2} P_{\text{approx}}(\bar{q}^2) \exp \left(- \int_{\bar{q}^2}^{\infty} \frac{d\bar{l}^2}{\bar{l}^2} \frac{\alpha_s}{2\pi} P_{\text{approx}}(\bar{l}^2) \right), \tag{2.103}$$

where the second argument of function Q_{approx} is the upper limit of the integral in the exponent of the above equation. The algorithm used to get \bar{q}^2 from Q_{true} is to use a series of probability densities which can be easily obtained by modifying only the upper limit of the integration in the exponential of Eq. (2.103) to be a variable \bar{p}^2 . The procedure of sampling and rejecting is as follows:

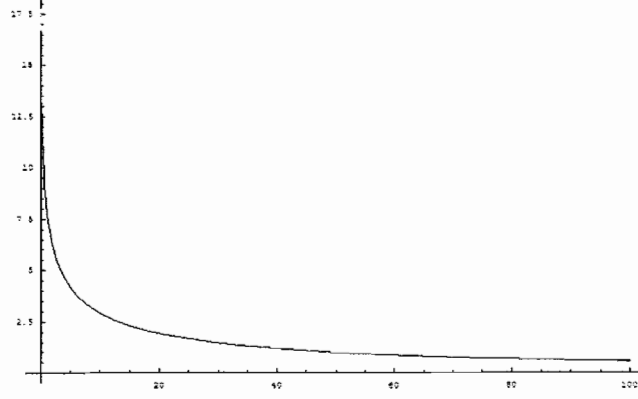


FIGURE 2.13: The virtual gluon self-energy function is plotted as the black line, and the proposal function P_{approx} is plotted as the gray line.

- (1) Sample a new random variable x from $Q_{\text{approx}}(x, \bar{k}^2)$ and u from a uniform distribution in $[0, 1]$;
- (2) See if $u < \frac{P_{\text{true}}(x)}{P_{\text{approx}}(x)}$ is true:
 - (a) If true, then accept x as a sample point for \bar{q}^2 ;
 - (b) If false, then assign the value of x to \bar{k}^2 , go back to step (1) and repeat the algorithm, with the replacement of $Q_{\text{approx}}(x, \bar{k}^2)$ by $Q_{\text{approx}}(x, \bar{k}'^2)$.

We initialize \bar{k}^2 to be ∞ every time we begin sampling a new point for \bar{q}^2 . The validity of the above algorithm can be proved without much trouble. For simplicity, suppose we only need to sample points in a finite region between 0 and \bar{q}_{max}^2 , and divide this region into N small pieces with the same size $\Delta \equiv \bar{q}_{\text{max}}^2/N$. The boundaries of those small regions are denoted as $\bar{q}_0^2, \bar{q}_1^2, \dots, \bar{q}_i^2, \dots, \bar{q}_N^2$. Obviously, in the limit of $N \rightarrow \infty$, the probability of getting an accepted point for \bar{q}^2 within $[\bar{q}_i^2, \bar{q}_{i+1}^2]$ during the first iteration is

$$\begin{aligned}
 P_0 &= Q_{\text{approx}}(\bar{q}_i^2, \bar{q}_{\text{max}}^2) \cdot \Delta \cdot \frac{P_{\text{true}}(\bar{q}_i^2)}{P_{\text{approx}}(\bar{q}_i^2)} \\
 &= \frac{1}{\bar{q}_i^2} \frac{\alpha_s}{2\pi} P_{\text{true}}(\bar{q}_i^2) \exp\left(-\int_{\bar{q}_i^2}^{\bar{q}_{\text{max}}^2} \frac{d\bar{l}^2}{\bar{l}^2} \frac{\alpha_s}{2\pi} P_{\text{approx}}(\bar{l}^2)\right) \cdot \Delta. \quad (2.104)
 \end{aligned}$$

It is also not difficult to figure out the probability of getting an accepted point within the same region $[\bar{q}_i^2, \bar{q}_{i+1}^2]$ during the second iteration is a sum of conditional probabilities:

$$\begin{aligned}
P_1 &= Q_{\text{approx}}(\bar{q}_{i+1}^2, \bar{q}_{\text{max}}^2) \cdot \Delta \cdot \left(1 - \frac{P_{\text{true}}(\bar{q}_{i+1}^2)}{P_{\text{approx}}(\bar{q}_{i+1}^2)}\right) \cdot Q_{\text{approx}}(\bar{q}_i^2, \bar{q}_{i+1}^2) \cdot \Delta \cdot \\
&\quad \cdot \frac{P_{\text{true}}(\bar{q}_i^2)}{P_{\text{approx}}(\bar{q}_i^2)} \\
&+ Q_{\text{approx}}(\bar{q}_{i+2}^2, \bar{q}_{\text{max}}^2) \cdot \Delta \cdot \left(1 - \frac{P_{\text{true}}(\bar{q}_{i+2}^2)}{P_{\text{approx}}(\bar{q}_{i+2}^2)}\right) \cdot Q_{\text{approx}}(\bar{q}_i^2, \bar{q}_{i+2}^2) \cdot \Delta \cdot \\
&\quad \cdot \frac{P_{\text{true}}(\bar{q}_i^2)}{P_{\text{approx}}(\bar{q}_i^2)} \\
&+ \dots \\
&+ Q_{\text{approx}}(\bar{q}_N^2, \bar{q}_{\text{max}}^2) \cdot \Delta \cdot \left(1 - \frac{P_{\text{true}}(\bar{q}_N^2)}{P_{\text{approx}}(\bar{q}_N^2)}\right) \cdot Q_{\text{approx}}(\bar{q}_i^2, \bar{q}_N^2) \cdot \Delta \cdot \\
&\quad \cdot \frac{P_{\text{true}}(\bar{q}_i^2)}{P_{\text{approx}}(\bar{q}_i^2)} \\
&= \frac{1}{\bar{q}_i^2} \frac{\alpha_s}{2\pi} P_{\text{true}}(\bar{q}_i^2) \exp\left(-\int_{\bar{q}_i^2}^{\bar{q}_{\text{max}}^2} \frac{d\bar{l}^2}{\bar{l}^2} \frac{\alpha_s}{2\pi} P_{\text{approx}}(\bar{l}^2)\right) \cdot \Delta \cdot \\
&\quad \cdot \int_{\bar{q}_i^2}^{\bar{q}_{\text{max}}^2} \frac{d\bar{l}^2}{\bar{l}^2} \frac{\alpha_s}{2\pi} [P_{\text{approx}}(\bar{l}^2) - P_{\text{true}}(\bar{l}^2)] \tag{2.105}
\end{aligned}$$

If calculating probabilities like those given above for the rest iterations and summing them up, one would obtain the Taylor expansion of

$$\begin{aligned}
Q_{\text{true}}(\bar{q}_i^2, \bar{q}_{\text{max}}^2) \cdot \Delta &= \frac{1}{\bar{q}_i^2} \frac{\alpha_s}{2\pi} P_{\text{true}}(\bar{q}_i^2) \exp\left(-\int_{\bar{q}_i^2}^{\bar{q}_{\text{max}}^2} \frac{d\bar{l}^2}{\bar{l}^2} \frac{\alpha_s}{2\pi} P_{\text{true}}(\bar{l}^2)\right) \cdot \\
&\quad \cdot \Delta, \tag{2.106}
\end{aligned}$$

and therefore the validity of algorithm of sampling \bar{q}^2 according to $Q_{\text{true}}(\bar{q}^2, \bar{q}_{\text{max}}^2)$ is proved.

Now let us show that Eq. (2.74) is indeed solvable if we use the auxiliary function P_{approx} . If we write down Eq. (2.74) explicitly, and call the random number in $[0, 1]$,

$$\begin{aligned}
r &= \exp \left[- \int_{\bar{q}^2}^{\bar{p}^2} \frac{d\bar{l}^2}{\bar{l}^2} \frac{\alpha_s}{2\pi} P_{\text{approx}}(\bar{l}^2) \right] \\
&\Downarrow \\
\frac{2\pi}{\alpha_s} \log(1/r) &= \int_{\bar{q}^2}^{\bar{p}^2} \frac{d\bar{l}^2}{\bar{l}^2} P_{\text{approx}}(\bar{l}^2) \\
&= \int_{\bar{q}^2}^{\infty} \frac{d\bar{l}^2}{\bar{l}^2} P_{\text{approx}}(\bar{l}^2) - \int_{\bar{p}^2}^{\infty} \frac{d\bar{l}^2}{\bar{l}^2} P_{\text{approx}}(\bar{l}^2) \\
&\equiv i_q - i_p, \tag{2.107}
\end{aligned}$$

where \bar{p}^2 is the given upper limit of splitting virtuality. The value of the integral included in the second term of the above equation depends on how big \bar{p}^2 is compared to μ_{mod}^2 since the expression for $P_{\text{approx}}(\bar{l}^2)$ changes when \bar{l}^2 crosses over the point of $\bar{l}^2 = \mu_{\text{mod}}^2$, as exemplified by Eq. (2.101). The integration is straightforward, and we only give the results here:

$$i_p = \begin{cases} 2N_c \log\left(\frac{\mu_{\text{mod}}^2}{\bar{p}^2}\right) + b \left(1 + \log\left(\frac{\mu_{\text{mod}}^2}{\bar{p}^2}\right)\right) / \mu_{\text{mod}}^2 & \text{if } \bar{p}^2 < \mu_{\text{mod}}^2 \\ b/\bar{p}^2 & \text{if } \bar{p}^2 > \mu_{\text{mod}}^2 \end{cases}, \tag{2.108}$$

where b is the same as defined in Eq. (2.102). Now we can easily get

$$i_q = i_p + \frac{2\pi}{\alpha_s} \log(1/r). \tag{2.109}$$

Similarly, before solving for \bar{q}^2 given a randomly generated number r , we need to perform the integration of i_q as well with the fact kept in mind that P_{approx} has different forms in different regions. Eventually one can derive the following analytical expressions for \bar{q}^2 which can be easily implemented in computer programs:

$$\bar{q}^2 = \begin{cases} b/i_q & \text{if } i_q < \frac{b}{\mu_{\text{mod}}^2} \\ \mu_{\text{mod}}^2 \exp \left[\frac{\frac{b}{\mu_{\text{mod}}^2} - \sqrt{\left(\frac{b}{\mu_{\text{mod}}^2}\right)^2 + 4N_c \left(i_q - \frac{b}{\mu_{\text{mod}}^2}\right)}}{2N_c} \right] & \text{if } i_q > \frac{b}{\mu_{\text{mod}}^2} \end{cases}. \tag{2.110}$$

In addition to generating the splitting virtualities according to virtual self-energy functions of partons in Coulomb gauge at one loop level with the help of auxilliary functions, one also has to generate the right momentum distribution among the splitting products. According to straightforward calculation of Feynman diagrams under the assumption of collinear splitting as what we did earlier, the momentum fraction of one of the two daughter partons, x , should obey some approximate probability density distributions $\hat{P}(x)$. These functions are exactly the Alterelli-Parisi functions we have derived step by step. Thus naturally, we should be able to generate the right momentum fractions using Eq. (2.75). However, because of the complexities of some of the integrals of the virtual parton self-energy function over the momentum fraction space, the above method is not well suited for numerical calculations. To solve this problem, we will first introduce a very useful technique called *Importance Sampling*.

Typically, importance sampling is frequently used to evaluate expectation values at some distribution of interest that is not available or impractical for various reasons. Importance sampling would generate random samples according to another probability measure, but still manage to calculate the expectation values correctly. Generally, suppose one wants to figure out the expectation of function $f(x)$ given a distribution $p(x)$,

$$\mathbb{E}[f(X)|p] \equiv \int f(x)p(x) dx , \quad (2.111)$$

what he can do is to generate random samples according to p , and take the following to be an estimate of the real expectation after n iterations,

$$\hat{\mathbb{E}}[f(X)|p] \equiv \frac{1}{n} \sum_{i=1}^n f(x_i) . \quad (2.112)$$

Sometimes the distribution of interest could be hard to generate numerically. Instead, if one has another probability distribution $q(x)$, namely the *proposal* distribution, and still wants to calculate the same expectation, he could do use an another estimate

of the same integral by trivially rewriting Eq. (2.111) as below:

$$\begin{aligned}
 \mathbb{E}[f(X) | p] &= \int f(x) p(x) dx \\
 &= \int \frac{f(x)}{\rho(x)} q(x) dx \\
 &= \mathbb{E} \left[\frac{f(X)}{\rho(x)} | q \right], \tag{2.113}
 \end{aligned}$$

where

$$\rho(x) \equiv q(x) / p(x), \tag{2.114}$$

and usually ρ^{-1} is called the *importance weight*. So the estimate we are looking for from samples produced according to the proposal distribution is

$$\hat{\mathbb{E}}[(f/\rho) | q] = \frac{1}{n} \sum^n f(x_i) / \rho(x). \tag{2.115}$$

We can imagine by choosing proper importance weight one can optimize the numerical integration, through avoiding enormous fluctuations of the integrand within the region of integration.

In our case, BEOWULF uses a simple proposal distribution that is easy to calculate the integral of, and thus samples can be generated straightforwardly by solving the (2.75) repeatedly. In turn the integrand will have an extra factor of ρ^{-1} that accounts for the change in the distribution of random points. In more detail, the density of sampling distribution is taken to be

$$q(x) \sim N_c \frac{(1 + \bar{q}^2/\bar{q}^2)}{2\min(x, 1-x) + \bar{q}^2/\bar{q}^2}. \tag{2.116}$$

up to a normalization factor. N_c is the color factor of the splitting under investigation. Obviously $q(x)$ given above is invariant under the transformation $x \rightarrow 1-x$, and it is because the distribution of two daughter partons in the momentum space is symmetric. This sampling distribution does have a much simpler algebraic form and thus Eq. (2.75) can be solved without too much programming efforts.

2.5.3 Numerical Tests

For practical reasons that have been stated many times earlier in this article, we would like to develop even further showers from the partons after the primary splittings, and finally generate hadrons instead of partons. It is the main motivation for us to match the NLO matrix elements with parton showers and hadronizations. In our case to do it properly, the shower history has to be recorded during the primary splitting, because later the final state partons from the primary showering will become the initial state of Pythia, a LO Monte Carlo program that generates parton showers and hadronizations, and Pythia needs to know some necessary information [9] to kick off further evolutions of the hardest partons, such as parton flavors, color configuration, hardness scale of the last splitting, etc. Eventually events with physical particles can be generated by Pythia, but this time calculations done based on those events will be accurate to the next-to-leading order as we will confirm below, and thus we say this type of calculation is carried out in the mode of NLO + PS + Had. Similarly, if we only use Born graphs with showers and hadronization, we shall refer to this mode as LO + PS + Had. We also perform calculations from a pure lowest order perturbative calculation, LO, from a pure next-to-leading order perturbative calculation, NLO, and from the program Pythia itself.

There are several things to be examined before one can confirm this program's validity. First of all, we need to make sure the calculation in the mode of NLO + PS is indeed accurate to the order of α_s^2 . Let us make use of the results of 3-jet fraction in different modes, and construct the following ratio [9],

$$R[\text{NLO} + \text{PS}] = \frac{f_3[\text{NLO} + \text{PS}] - f_3[\text{NLO}]}{f_3[\text{NLO}]} . \quad (2.117)$$

This ratio should have a perturbative expansion starting at order α_s^2 . The rationale is that the difference of $f_3[\text{NLO} + \text{PS}]$ and $f_3[\text{NLO}]$ should start at order α_s^3 if the matching of parton showers to the matrix elements is done correctly. The denominator, the 3-jet fraction of NLO alone, apparently begins at order α_s , since

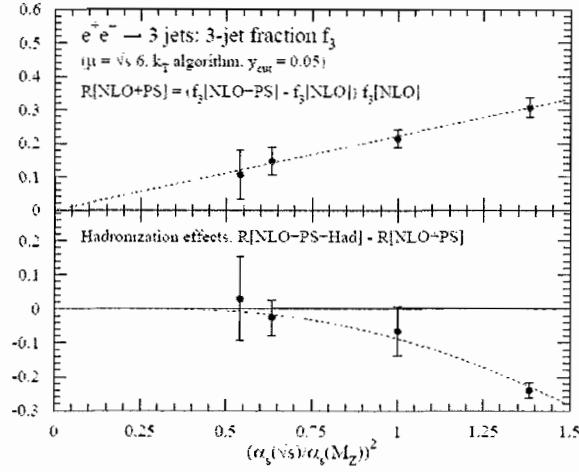


FIGURE 2.14: Comparison of the NLO calculation with showers with pure NLO calculation. In the upper panel, we plot the results of $R[\text{NLO} + \text{PS}]$ at different c.m. energies $\sqrt{s} = 34 \text{ GeV}$, M_Z , 500 GeV and 1000 GeV , which correspond to $\alpha_s = 0.139, 0.118, 0.0940$ and 0.0868 respectively. For comparison, we also show the curve $R = 0.22\alpha_s^2(\sqrt{s})/\alpha_s^2(M_Z)$. In the lower panel we plot the difference between NLO calculations with hadronizations and without hadronizations. For comparison, we also display the curve $\Delta R = 8\text{GeV}/\sqrt{s}$. This figure is provided by [9].

there can only be 2-jet events in the final state of $e^+ + e^- \rightarrow$ partons if the strong interaction is completely turned off. As a consequence, we expect the dependence of $R[\text{NLO} + \text{PS}]$ on α_s^2 should approach a linear function of α_s^2 . To confirm this, we compute f_3 at different c.m. energies \sqrt{s} , and plot our results for $R[\text{NLO} + \text{PS}]$ against $\alpha_s^2(\sqrt{s})/\alpha_s^2(M_Z)$ in Fig 2.14. It can be seen that the R curve indeed looks like a straight line near the origin, and hence we can conclude the integrated NLO calculation with parton showers is as expected accurate to the next-to-leading order.

Furthermore, we construct a similar ratio for NLO calculations with both parton showers and hadronizations, and consider the quantity $\Delta R \equiv R[\text{NLO} + \text{PS} + \text{Had}] - R[\text{NLO} + \text{PS}]$, it should display the property of non-perturbative corrections due to hadronizations. The result of this second test is shown in the lower panel in Fig 2.14, and we discover that points of ΔR can be fit into a simple power law function,

$\Delta R = 8\text{GeV}/\sqrt{s}$. This observation can be explained by adopting an analytical approach to estimate the hadronization effects. The idea is to introduce a universal, non-perturbative parameter

$$\alpha_0(\mu_I) = \frac{1}{\mu_I} \int_0^{\mu_I} dk \alpha_s(k) \quad (2.118)$$

to parameterize the unknown behavior the strong coupling constant below a certain matching scale μ_I . In this way divergent soft gluon contributions to the event shape observables can be removed, and corrections proportional to the powers of $1/\sqrt{s}$ are generated thanks to this technique [16]. Our results is a direct confirmation for this new method.

To verify the statement that NLO calculations with parton showers is superior to pure NLO calculations, we also select events with 3 jet in the final state and calculate the jet mass distributions normalized by the 3-jet fraction, $f_3^{-1}df_3/dM$, using $y_{\text{cut}} = 0.05$. Remember one of the main motivations of devising a MC-NLO event generator is to produce sensible predictions for differential cross sections of event shape variables. Pure NLO calculations can not avoid the unrealistic increase of cross sections near the small mass region, as shown in Fig 2.1. The result of $f_3^{-1}df_3[\text{NLO} + \text{PS} + \text{Had}]/dM$ is shown in Fig 2.15.

Apparently, by adding parton showers and hadronizations to the NLO calculation, one can remove the unphysical infrared behavior of the distribution of event shape variables. In Fig 2.16, it is worth noticing the full NLO+PS+Had calculation yields very similar results to those given by Pythia alone.

As an investigation of the magnitude of corrections induced by parton showers and hadronizations, we finally examine the 3-jet fraction f_3 as a function of the jet resolution parameter y_{cut} in five different modes, NLO, LO, NLO+PS+Had, LO+PS+Had and Pythia. One would expect NLO and NLO+PS+Had to generate very similar results. Because if the matching scheme is valid, the jet structure should be mainly determined by the hardest interaction, which is described by the matrix

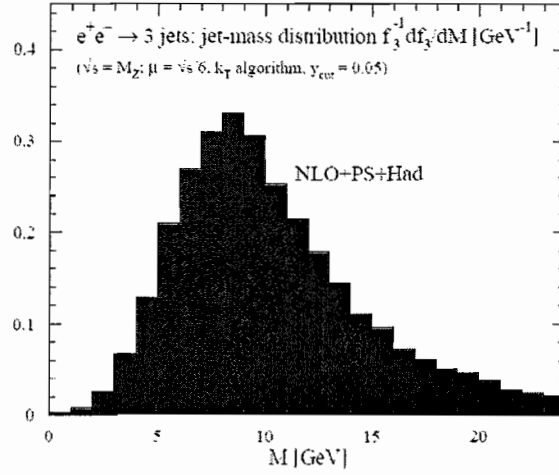


FIGURE 2.15: Jet mass distribution in three-jet events in the full NLO+PS+Had calculation. This figure is provided by [9].

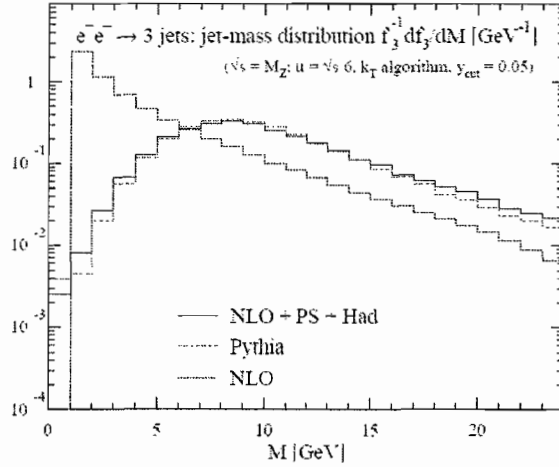


FIGURE 2.16: Distribution of jet masses in three-jet events, $f_3^{-1}df_3/dM$, in pure NLO calculation, in pure Pythia calculation and in the full NLO+PS+Had calculation. This figure is provided by [9].

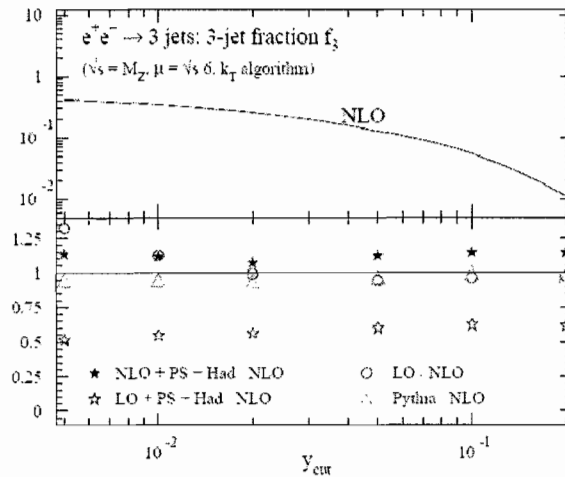


FIGURE 2.17: Three jet fraction f_3 versus y_{cut} . In the top panel, f_3 is plotted as a function of y_{cut} in the pure NLO calculation. The bottom panel shows the ratios of f_3 [NLO + PS + Had], f_3 [LO], f_3 [LO + PS + Had] and f_3 [Pythia] to f_3 [NLO]. This figure is provided by [9].

elements calculation. This argument is proved to be true in Fig 2.17. Pythia also does amazingly well.

2.5.4 Manipulation of Splitting Functions

A disturbing observation about Fig 2.17 is the parton showers and hadronizations added to the Born graphs seems to change the jet structure by a considerable amount, since f_3 [LO + PS + had] is only about half of f_3 [LO] for all selected values of y_{cut} . Presumably the 3-jet fractions for pure LO calculation and for the LO calculation with hadronizations should not be two different. In a valid matching scheme and shower simulation, hard splittings need to be completed before splittings with less virtualities, and as a result, most of the n-jet event that are fed into Pythia should also come out as a n-jet event. Therefore, there must be something that needs to be corrected, especially within the stage of the primary splittings which has not been thoroughly tested yet compared to the well accepted shower algorithm built-in to

Pythia. The magnitude of the deviation of $f_3 [\text{LO} + \text{PS} + \text{had}]$ from $f_3 [\text{LO}]$ can be estimated by considering a factor of $[1 - X\alpha_s (\sqrt{s}/6)]$, which is brought up every time a primary splitting is added to a cut parton propagator in the LO Feynman diagrams and change the normalization by an amount proportional to $\alpha_s (\sqrt{s}/6)$. Qualitatively, since there are three cut propagators in such graphs, one can therefore approximately predict that

$$\frac{f_3 [\text{LO} + \text{PS} + \text{had}]}{f_3 [\text{LO}]} \approx [1 - X\alpha_s (\sqrt{s}/6)]^3, \quad (2.119)$$

where the coefficient X is determined by the splitting functions that we use in the matching algorithm. With the c.m. energy chosen to be 91 GeV and thus $\alpha_s (\sqrt{s}/6) \approx 0.16$, we conclude this branching coefficient X must be ~ 1.5 in order to produce what we see in Fig 2.17. Obviously one could make X much closer to zero in order to resolve this problem, and our remedy is of course to adopt different splitting functions for the primary splittings. Following the same logic behind Eq. (2.87) and Eq. (2.88), in the calculation of shower amplitude $\mathcal{I} [\text{shower}, \lambda_V]$ we choose to replace the one-loop self-energy function \mathcal{M} with a new function, whose form will be restricted later, and to leave the Sudakov exponential untouched. Through some treatment on the propagators of corresponding NLO graphs, the NLO calculations with parton showers will remain equivalent to the pure NLO calculations, up to a slightly different NNLO (Next-to-Next-Leading Order) correction. However, the LO calculations with parton showers can vary a lot as we split the hard partons according to different functions. We can hence make use of the sensitivity of $\mathcal{I} [\text{shower}, \lambda_V]$ to the choice of splitting functions, and justify the reliability of the resulting primary splitting. If one can bring $f_3 [\text{LO} + \text{PS} + \text{had}]$ and $f_3 [\text{LO}]$ closer to each other, we would be able to preserve the virtuality hierarchy inherent with the parton shower algorithm, and keep the approximations made in such an algorithm relevant.

In order to put constraints on a valid splitting function that substitutes \mathcal{M} , we need to remind ourselves about how to keep NLO calculations with showers accurate

to the next-to-leading order. Suppose we replace function \mathcal{M} and \mathcal{P} in the shower amplitude $\mathcal{I}[\text{shower}]$ with different functions \mathcal{M}' and \mathcal{P}' . The cut on shower scales has been omitted here from the amplitude deliberately for simplification. In the calculation of NLO matrix elements, we need to use $\mathcal{M} - \mathcal{M}'$ instead of \mathcal{M} alone to represent the cut one-loop self-energy function, and use $\mathcal{P} - \mathcal{P}'$ instead of \mathcal{P} alone to represent the virtual one-loop function, so that partons can develop primary showers without undermining the program's NLO accuracy. One special example is when $\mathcal{M}' = \mathcal{M}$ and $\mathcal{P}' = \mathcal{P}$, NLO graphs that contain such cut propagators are simply removed calculation. According to this argument, even if the two sets of splitting functions are different, the function with its pairing substitute still has to have the same IR limit. This is because both \mathcal{P} and \mathcal{P}' are IR divergent. Also $\mathcal{M} - \mathcal{M}'$ and $\mathcal{P} - \mathcal{P}'$ shall be integrated to zero virtuality, and both subtractions have to be free of infrared divergences in order for the numerical integration to converge fast enough.

The last paragraph is basically a recapitulation of the Sec. 2.5.2. In that section, the virtual parton self-energy function \mathcal{P} is used to replace the coefficient of the non-vanishing transverse component of the cut parton self-energy function, and as a result, cancellations of some of the IR divergences in NLO graphs are achieved, because the constraint on new splitting functions explained in last paragraph is satisfied. However, this specific implementation of shower scheme could only give us results displayed in Fig. 2.17. Through further investigation and repetitive trials, we find that by putting a factor

$$C(\bar{q}^2, \bar{q}^2) = 1 + \frac{A\bar{q}^2}{B\bar{q}^2 + \bar{q}^2} \quad (2.120)$$

in front of the term including \mathcal{P} in the definition of cut parton self-energy function, and by using this modified function to split Born-level partons, one can effectively enhance parton branching and convert more 2-jet events to 3-jet events because the additional factor is always greater than 1. Meanwhile, one can also retain the same

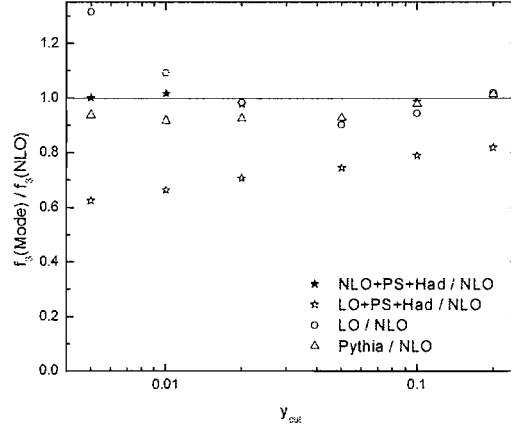


FIGURE 2.18: Three jet fraction f_3 versus y_{cut} . The plot shows the ratios of f_3 [NLO + PS + Had], f_3 [LO], f_3 [LO + PS + Had] and f_3 [Pythia] to f_3 [NLO], with a modified splitting function.

IR limit of the splitting function if the virtuality goes to zero for fixed \bar{q}^2 . In the latest version of program BEOWULF, we set

$$\begin{cases} \mathcal{A} = 2.0 \\ \mathcal{B} = 4.0 \end{cases}, \quad (2.121)$$

and test our choice of parameters by once again plotting the ratios of 3-jet fractions in different modes to the same observable calculated by pure NLO calculations. The results are shown in Fig. 2.18.

In Fig. 2.18, there are several things that are different from the old graph in Fig. 2.17. First of all, compared to the results generated by using old splitting functions, the values of f_3 [LO + PS + Had] are now brought much closer to the pure LO values by switching to the modified splitting functions. The ratio of f_3 [LO + PS + Had] to f_3 [NLO] has become 60% \sim 80% as the chosen jet resolution parameter y_{cut} varies from 0.002 to 0.2. As the smaller y_{cut} one uses, the better resolution one would have over jet finding. Therefore, if there are a lot of 3-jet

events that contain a jet which could be identified as two separate jets, the trend of f_3 [LO + PS + Had] growing as y_{cut} increases would be well explained. However, we still cannot understand why LO calculation with hadronization would develop more events of this type than the rest of the modes. Another improvement displayed by Fig. 2.18 over the old graph is that NLO calculation with hadronizations are now yielding f_3 more consistently with the pure NLO calculation. The average difference between f_3 [NLO + PS + Had] and f_3 [NLO] was around 10%, and a systematic deviation was implied since f_3 [NLO + PS + Had] was universally greater than f_3 [NLO] for different jet resolution parameters. After the splitting functions are modified, the average difference between those two quantities has been reduced to less than 5%, and the unpleasant systematic deviation seems to vanish. This observation also justifies the change made to the primary splitting in BEOWULF.

A variety of tests, such as those that have been done on the old program, can also be performed on the modified program in order to examine its NLO accuracy, ability to deal with differential cross sections, etc., but those tests shall be removed from further discussion here because of the similarity displayed in the results. Instead, we study the program's dependence on the choice of splitting functions. A number of different 3-jet infrared-safe observables are picked for this purpose. We will show the program with modified splitting functions is superior. Before that, we first need to introduce some fundamentals of useful event-shape variables.

2.6 Event Shape Variables

This brief introduction is about how to calculate different event-shape variables of hadronic final states of electron-positron annihilations, including jet production rates, Thrust, Thrust Minor and Major, Oblateness, C-Parameter, Sphericity, jet masses, the jet broadening measures, energy correlations. Earlier, we have already frequently used the concept "3-jet fraction" many times, without seriously defining

what exactly a “3-jet event” refers to. So we will start with defining such an event, and also discuss several different ways to constrain the jet resolution.

2.6.1 Jet Algorithms

Let us take the “minimum invariant mass” or JADE algorithm as an example.

Consider $q\bar{q}g$ production at $O(\alpha_S)$, e.g., with three partons in the final state. In this specific algorithm, a three-jet event is defined as one in which the minimum invariant mass of the parton pairs is larger than some fixed resolution constant y (sometimes called y_{cut}) of the overall center-of-mass energy:

$$\min (p_i + p_j)^2 = \min 2E_i E_j (1 - \cos \theta_{ij}) > y_{cut}, \quad i, j = q, \bar{q}, g. \quad (2.122)$$

More jet-finding algorithms and definitions of their corresponding resolution parameters are listed in Table 2.4. Generally speaking, such algorithms always begin with calculating the resolution values for every possible pair of final-state particles. The next step is to compare the minimum resolution values with the fixed resolution parameter y_{cut} . If y_{cut} is greater than this minimum value, one should first proceed to combine the two particles that correspond to the minimum value according to rule of combining displayed in Table 2.4, and then treat the combined particles as a single new particle when finding the new minimum resolution value during the next cycle. If y_{cut} is smaller, however, one should instead terminate the current jet-finding algorithm, and the jet structure of the current cycle will be used as the finalized jet structure.

2.6.2 Thrust-Related Variables

The following variables are either the variable of Thrust itself, or variable which must be defined with the help of thrust-axis. We will start with defining the variable Thrust.

TABLE 2.4: Definition of the resolution measures y_{ij} and of combination schemes for various jet algorithms.

Algorithm	Resolution	Combination	Remarks
E	$\frac{(p_i + p_j)^2}{s}$	$p_k = p_i + p_j$	Lorentz invariant
JADE	$\frac{2E_i E_j (1 - \cos \theta)}{s}$	$E_k = E_i + E_j$	conserves $\sum E, \sum \mathbf{p}$
E0	$\frac{(p_i + p_j)^2}{s}$	$E_k = E_i + E_j,$ $\mathbf{p}_k = \frac{E_k}{ \mathbf{p}_i + \mathbf{p}_j } \cdot (\mathbf{p}_i + \mathbf{p}_j)$	conserves $\sum E$, but violates $\sum \mathbf{p}$
P	$\frac{(p_i + p_j)^2}{s}$	$\mathbf{p}_k = \mathbf{p}_i + \mathbf{p}_j,$ $E_k = p_k$	conserves $\sum \mathbf{p}$, but violates $\sum E$
D	$\frac{2 \cdot \min(E_i^2, E_j^2)}{s \cdot (1 - \cos \theta)}$	$p_k = p_i + p_j$	conserves $\sum E, \sum \mathbf{p}$; avoids exp.problems
G	$\frac{8E_i E_j (1 - \cos \theta_{ij})}{9(E_i + E_j)^2}$	$p_k = p_i + p_j$	conserves $\sum E, \sum \mathbf{p}_i$; avoids exp.problems
LUCLUS	$\frac{2 \mathbf{i}_i \cdot \mathbf{p}_j \sin \theta_{ij}/2}{ \mathbf{p}_i + \mathbf{p}_j }$	$p_k = p_i + p_j$	conserves $\sum E, \sum \mathbf{p}$ incalculable in perturbation theory

2.6.2.1 Thrust T

The thrust value of a hadronic event is defined by the expression

$$T = \max_{\vec{n}} \left(\frac{\sum_i |\vec{p}_i \cdot \vec{n}|}{\sum_i |\vec{p}_i|} \right). \quad (2.123)$$

The vector \vec{n} which maximizes the expression in parenthesis is the *thrust axis* \vec{n}_T . It is used to divide an event into two hemispheres H_1 and H_2 by a plane through the origin and perpendicular to the thrust axis.

2.6.2.2 Thrust-Major

Given the thrust axis \vec{n}_T which maximizes the sum in equation (2.123), the thrust major is defined as

$$T_M \equiv \max_{\vec{n} \cdot \vec{n}_T = 0} \frac{\sum_i |\vec{p}_i \cdot \vec{n}|}{\sum_i |\vec{p}_i|}, \quad (2.124)$$

where the vector \vec{n} , the thrust major axis, obviously lies in the plane perpendicular to the thrust axis.

2.6.2.3 Thrust-Minor

At this point, we define the event plane to be the plane spanned by the thrust axis and the thrust major axis as the yz -plane, and a unit vector along the x -axis would be $\vec{n}_{min} = \vec{n}_T \times \vec{n}$. And the thrust minor, which measures the radiation out of the event plane, can be defined as

$$T_{min} \equiv \frac{\sum_i |p_{ix}|}{\sum_i |\vec{p}_i|} = \frac{\sum_i |\vec{p}_i \cdot \vec{n}_{min}|}{\sum_i |\vec{p}_i|}. \quad (2.125)$$

2.6.2.4 Oblateness

Given the thrust major and thrust minor defined above, the oblateness is given by

$$O \equiv T_M - T_{min}. \quad (2.126)$$

2.6.2.5 Heavy Jet Mass M_H

From the particles in each of the two hemispheres defined by the thrust axis an invariant mass is calculated. The heavy jet mass M_H is defined to be the larger of the two jet masses. The original analysis by S.Bethke used the measured heavy jet mass scaled by the visible energy E_{vis} which is, after correction for detector resolution, acceptance, and for initial state radiation, equal to M_H/\sqrt{s} . More specifically, in any event, as for the two hemispheres of particles divided by the thrust axis \vec{n}_T , we call the right one R , and the left one L . The squared heavy jet mass is defined as

$$M_H^2 \equiv \max \{ M_R^2, M_L^2 \}, \quad (2.127)$$

where M_R^2, M_L^2 are the single hemisphere squared masses normalized to be dimensionless

$$M_R^2 \equiv \sum_{i \in R} \left(\frac{p_i}{\sum_j |\vec{p}_j|} \right)^2, \quad M_L^2 \equiv \sum_{i \in L} \left(\frac{p_i}{\sum_j |\vec{p}_j|} \right)^2 \quad (2.128)$$

2.6.2.6 Jet Broadening B

The jet broadening measures are calculated by the expression:

$$B_k = \left(\frac{\sum_{i \in H_k} |\vec{p}_i \times \vec{n}_T|}{2 \sum_i |\vec{p}_i|} \right) \quad (2.129)$$

for each of the two hemispheres, H_k , defined above. The total jet broadening is given by $B_T = B_1 + B_2$. The wide jet broadening is defined by $B_W = \max(B_1, B_2)$.

2.6.3 C-Parameter

The C-Parameter is defined as

$$C = 3(\lambda_1\lambda_2 + \lambda_2\lambda_3 + \lambda_3\lambda_1) \quad (2.130)$$

where λ_γ , $\gamma = 1, 2, 3$, are the eigenvalues of the momentum tensor

$$\Theta^{\alpha\beta} = \frac{\sum_i \vec{p}_i^\alpha \vec{p}_i^\beta / |\vec{p}_i|}{\sum_j |\vec{p}_j|}. \quad (2.131)$$

The book *QCD and Collider Physics* [10] gives an algebraic expression of the C-Parameter, which is equation (3.41):

$$C = \frac{3 \sum_{i,j} [|\vec{p}_i||\vec{p}_j| - (\vec{p}_i \cdot \vec{p}_j)^2 / |\vec{p}_i||\vec{p}_j|]}{(\sum_i |\vec{p}_i|)^2}. \quad (2.132)$$

The two above definitions of C-Parameter are equivalent to each other. The proof is given below.

First, take the trace of the momentum tensor (2.131), we could find the following:

$$Tr\Theta = \lambda_1 + \lambda_2 + \lambda_3 = \sum_{\alpha} \Theta^{\alpha\alpha}, \quad (2.133)$$

which leads to

$$(\lambda_1 + \lambda_2 + \lambda_3)^2 = \lambda_1^2 + \lambda_2^2 + \lambda_3^2 + 2(\lambda_1\lambda_2 + \lambda_2\lambda_3 + \lambda_3\lambda_1) = 1. \quad (2.134)$$

Therefore, the C-Parameter can also be expressed as

$$C = \frac{3}{2} \left[1 - (\lambda_1^2 + \lambda_2^2 + \lambda_3^2) \right] \quad (2.135)$$

Because Θ is real and symmetric, it can be diagonalized through orthogonal transformation, $U^{-1}\Theta U = D$. D is the resulting diagonal matrix, and its diagonal elements are the common eigenvalues of both matrices. The quantity $\lambda_1^2 + \lambda_2^2 + \lambda_3^2$

can be seen as the trace of the square of matrix D^2 . Since $D^2 = U^{-1}\Theta U \cdot U^{-1}\Theta U = U^{-1}\Theta^2 U$, we could say

$$\lambda_1^2 + \lambda_2^2 + \lambda_3^2 = Tr\Theta^2. \quad (2.136)$$

Now, let us write down $Tr\Theta^2$ explicitly in terms of the final state momentum:

$$\begin{aligned} Tr\Theta^2 &= \sum_{\alpha,\beta} \Theta^{\alpha\beta} \Theta^{\beta\alpha} \\ &= \sum_{\alpha,\beta} \frac{\sum_i \vec{p}_i^\alpha \vec{p}_i^\beta / |\vec{p}_i|}{\sum_j |\vec{p}_j|} \cdot \frac{\sum_j \vec{p}_j^\beta \vec{p}_j^\alpha / |\vec{p}_j|}{\sum_j |\vec{p}_j|} \\ &= \frac{\sum_{ij} [(\vec{p}_i \cdot \vec{p}_j)^2 / |\vec{p}_i| |\vec{p}_j|]}{\left(\sum_j |\vec{p}_j|\right)^2}. \end{aligned} \quad (2.137)$$

From here, we can derive

$$\begin{aligned} C &= \frac{3}{2} (1 - Tr\Theta^2) \\ &= \frac{3}{2} \left(1 - \frac{\sum_{ij} [(\vec{p}_i \cdot \vec{p}_j)^2 / |\vec{p}_i| |\vec{p}_j|]}{\left(\sum_j |\vec{p}_j|\right)^2} \right) \\ &= \frac{3}{2} \frac{\sum_{i,j} [|\vec{p}_i| |\vec{p}_j| - (\vec{p}_i \cdot \vec{p}_j)^2 / |\vec{p}_i| |\vec{p}_j|]}{\left(\sum_i |\vec{p}_i|\right)^2}. \end{aligned} \quad (2.138)$$

So we have proved the above two definitions of C-Parameter are indeed equivalent.

2.6.4 Sphericity

The sphericity of a certain event is defined as

$$S = \left(\frac{4}{\pi}\right)^2 \min_{\vec{n}} \left(\frac{\sum_i |\vec{p}_i \times \vec{n}|}{\sum_i |\vec{p}_i|} \right)^2. \quad (2.139)$$

TABLE 2.5: Values of the shape variables for different event types.

Quantity	T	S	C
pencil-like event	1	0	0
spherical event	$\frac{1}{2}$	1	1
$q\bar{q}g$	$\max\{x_i\}$	$\frac{16 \prod_i (1 - x_i)}{\pi^2 \max\{x_i^2\}}$	$6 \frac{\prod_i (1 - x_i)}{x_1 x_2 x_3}$

The vector \vec{n} minimizes the expression in the parenthesis. Since we have seen quite a few eventshape variables so far, it is a good time to give some typical values of those variables corresponding to some specially-shaped events. I put them in Table 2.6.4.

The third row of Table 2 works exclusively for events with three final-state partons. The expressions listed in that row are constraint functions f_X of x_1, x_2, x_3 for different shape variables, where

$$x_i \equiv \frac{E_i}{\sqrt{s}/2} = \frac{2p_i \cdot q}{s} \quad (2.140)$$

represents the energy fraction of a certain final state parton. q is the four-momentum of the intermediate virtual particle, eg. photons, Z bosons. And $s \equiv q^2$. Due to energy conservation, we should have

$$\sum_i x_i = \frac{2(\sum_i p_i \cdot q)}{s} = 2. \quad (2.141)$$

Here we have chosen the center-of-mass frame for the final-state partons, and made the approximation that all these final-state particles are massless. After some trivial calculations, following facts can be derived:

$$x_1 x_3 (1 - \cos \theta_{13}) = 2(1 - x_2), \quad (2.142)$$

and so

$$x_i < 1,$$

$$\theta_{13} \rightarrow 0 \quad \Leftrightarrow \quad x_2 \rightarrow 1.$$

At $O(\alpha_S)$, the distribution of total cross-section in the shape variable $d\sigma/dX$ ($X=T, S, \dots$) is obtained by integrating the right-hand side of

$$\sigma^{q\bar{q}g} = \sigma_0 \cdot 3 \sum_q Q_q^2 \int_J dx_1 dx_2 C_F \frac{\alpha_S}{2\pi} \frac{x_1^2 + x_2^2}{(1-x_1)(1-x_2)} \quad (2.143)$$

over x_1 and x_2 with the constraint

$$\delta(X - f_X(x_1, x_2, x_3 = 2 - x_1 - x_2)), \quad (2.144)$$

i.e. along a contour in the (x_1, x_2) plane. Other than that, there is something else that needs to be noticed here. As long as the variables are not equal to their pencil-like limits, e.g., $T < 1$, then those distributions are finite, since the soft and collinear configurations are excluded from the integration range [10]. I mentioned the above point because there are some shape variables whose calculations could involve soft and collinear singularities, like the *energy-energy correlation function (EEC)*, which I will talk about next.

2.6.5 Energy-Energy Correlation Function

EEC is a dimensionless angular distribution defined by

$$\begin{aligned} \frac{1}{\sigma} \frac{d\Sigma}{d\cos\chi} &= \sum_{\substack{i,j \\ i \neq j}} \int \frac{d^3p_i}{E_i} \frac{d^3p_j}{E_j} \left(\frac{2E_i E_j}{s} \right) E_i E_j \frac{d^6\sigma}{d^3p_i d^3p_j} \times \\ &\quad \times \delta(\vec{n}_i \cdot \vec{n}_j - \cos\chi) + \\ &\quad + \sum_i \int \frac{d^3p_i}{E_i} \left(\frac{E_i^2}{s} \right) E_i \frac{d^3\sigma}{d^3p_i} \delta(1 - \cos\chi) \end{aligned} \quad (2.145)$$

where $E_1 E_2 d^6\sigma/d^3p_1 d^3p_2$ is the two-hadron inclusive cross section. The first sum on the right-hand side is over all distinct pairs of hadrons— $n(n-1)/2$ terms for an

n-hadron final state. The second sum is a self-correlation (n terms) which guarantees the sum rule

$$\int_{-1}^1 d \cos \chi \frac{1}{\sigma} \frac{d\Sigma}{d \cos \chi} = 1, \quad (2.146)$$

since $\sum E_i = \sqrt{s}$. Eq (2.145) represents the standard integrated version of the EEC, in the sense that the information concerning the orientation of the final state with respect to the beam direction has been integrated out. A related quantity is the *asymmetry* of the energy-energy correlation function (EECA), defined by

$$\frac{1}{\sigma} \frac{d\Sigma^A}{d \cos \chi} = \frac{1}{\sigma} \frac{d\Sigma}{d \cos \chi} \Big|_{180^\circ - \chi} - \frac{1}{\sigma} \frac{d\Sigma}{d \cos \chi} \Big|_{\chi}, \quad (2.147)$$

for $0 \leq \cos \chi \leq 1$, which, at least in principle, has smaller hadronization corrections [10]. The EEC, therefore, measures the correlation of hadronic energy flow in an event. In a ‘two-jet’ event, for example, the function is strongly peaked at $\chi = 0^\circ$ and $\chi = 180^\circ$. In contrast, the more isotropic the event is, the flatter the distribution will be.

The energy-energy correlation function is infra-red safe. However, as I mentioned before, the calculation of this quantity involves singularities. Although those singular contributions from soft and collinear real gluon emission and from virtual gluons would finally be cancelled out since the net energy weighting and angular distribution is the same for both, they could still impose difficulty on the numerical computation of this observable [17].

It is easy to see that, at lowest order, $e^+e^- \rightarrow q\bar{q}$, the EEC is simply

$$\frac{1}{\sigma} \frac{d\Sigma}{d \cos \chi} = \frac{1}{2} \delta(1 - \cos \chi) + \frac{1}{2} \delta(1 + \cos \chi). \quad (2.148)$$

For $\chi \neq 0^\circ, 180^\circ$ the perturbation series starts at order α_S with the process $e^+e^- \rightarrow q\bar{q}g$, e.g.,

$$\frac{1}{\sigma} \frac{d\Sigma}{d \cos \chi} = \frac{\alpha_S(\mu^2)}{2\pi} A_1(\chi) + \left(\frac{\alpha_S(\mu^2)}{2\pi} \right)^2 A_2\left(\chi, \frac{s}{\mu^2}\right) + \dots \quad (2.149)$$

The first two terms in this series have been calculated. In fact, A_1 is obtained from the differential cross section given in Eq.(2.143) by including an appropriate δ -function expressing the angle χ in terms of the energy fractions x_i [10]. The functions $A_i(\chi)$ are singular at $\chi = 0^\circ, 180^\circ$, but well away from these regions the series appears to converge satisfactorily. As for the other shape variables, resummation of large logarithmic contributions can extend the region of applicability into the singular region. A familiar example is by using Monte Carlo event generators which include both NLO graph calculations and parton shower, one could control the singular behavior of jet-mass distribution $f_3^{-1}df_3/dM$ very well [9].

There is also a well-known paper by G.Kramer and H.Spiesberger [17] that can help understand the arguments above.

2.7 Numerical Results

In this section, the distributions of various event shape variables will be presented. All of the event shape variables that will appear here have been introduced in last section already. They are 3-jet infrared-safe observables, which means they would vanish when the parton configuration approaches the 2-jet region from 3-jet region. The distribution we will consider is, taking C parameter as an example, $(1/\sigma_T)d\sigma/dC$. It has been normalized using the total cross section, σ_T .

2.7.1 Validating Numerical Results

We let BEOWULF calculate distributions in three different modes: pure NLO, NLO + PS + Had with old splitting functions, and NLO + PS + Had with modified splitting functions. All those results are compared to experimental data. We want to find out if the program can really be improved by using new splitting functions in the primary parton showering stage. Two different energy scales, $\sqrt{s} = 35$ GeV and $\sqrt{s} = 91$ GeV, are chosen to be the c.m. energies of the initial electron-positron pair.

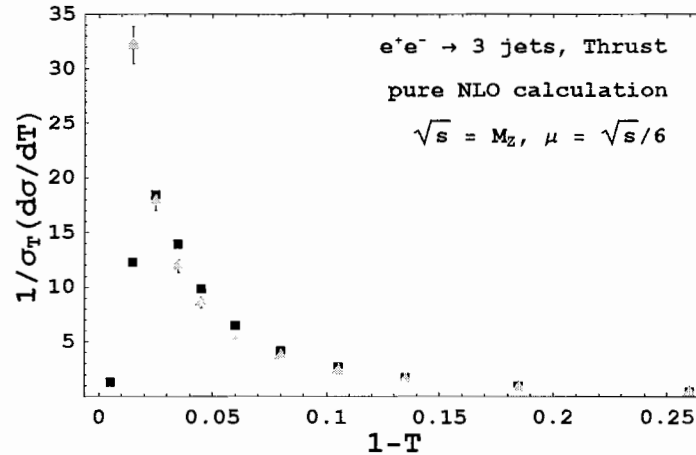


FIGURE 2.19: Thrust distribution. Experimental data is compared with the numerical results for Pure NLO (91 GeV).

In principle, more serious long distance effects should be present at the lower energy, which would obviously compromise the ability of pure NLO calculation to describe the shape of final states. However, non-perturbative effects can be accounted for by developing parton showers and hadronizations. We want to find out if parton showers and hadronizations can indeed be more helpful at the lower energy of the two. In this project, we use the experimental data presented in [18][19][20]. We choose to study the distributions of Thrust, Total Jet Broadening measure, Wide Jet Broadening measure, Heavy Jet Mass and C Parameter due to the availability of experimental data at 35 GeV.

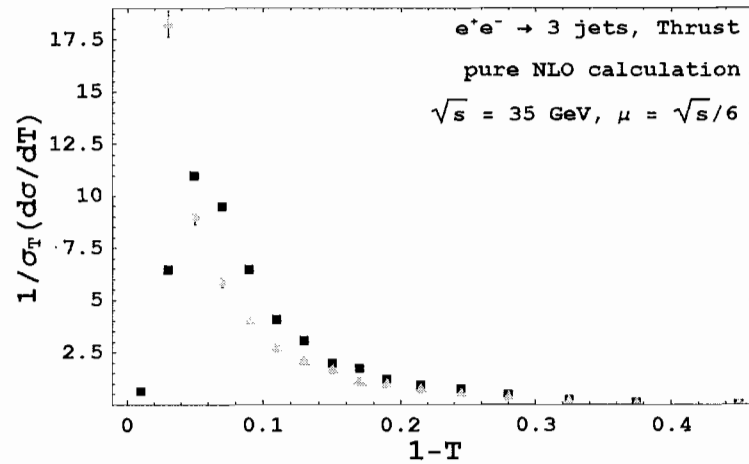


FIGURE 2.20: Thrust distribution. Experimental data is compared with the numerical results for Pure NLO (35 GeV).

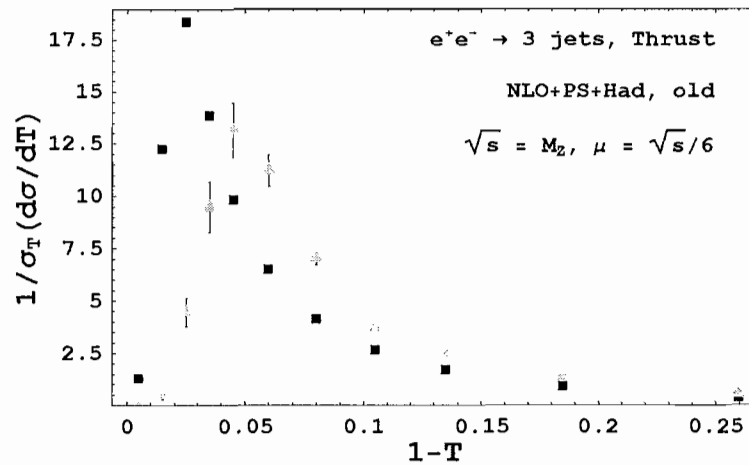


FIGURE 2.21: Thrust distribution. Experimental data is compared with the numerical results for NLO + PS + Had with old splitting functions (91 GeV).

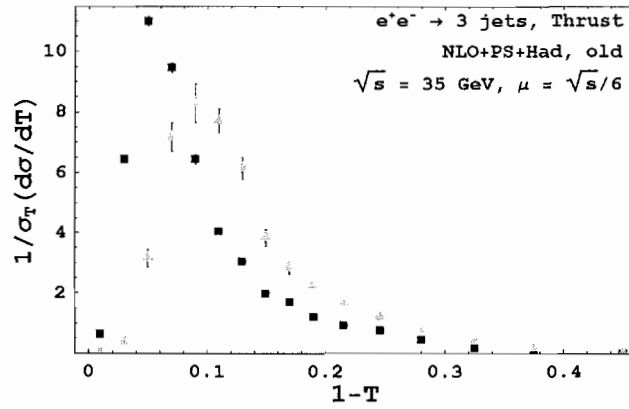


FIGURE 2.22: Thrust distribution. Experimental data is compared with the numerical results for NLO + PS + Had with old splitting functions (35 GeV).

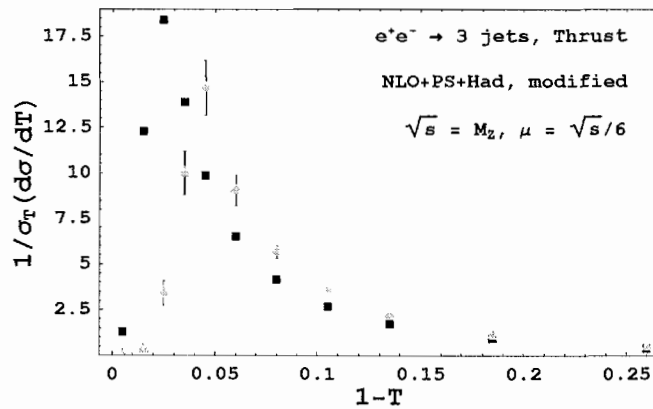


FIGURE 2.23: Thrust distribution. Experimental data is compared with the numerical results for NLO + PS + Had with modified splitting functions (91 GeV).

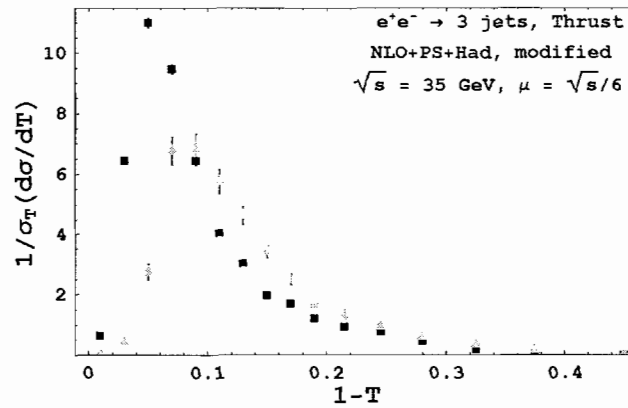


FIGURE 2.24: Thrust distribution. Experimental data is compared with the numerical results for NLO + PS + Had with modified splitting functions (35 GeV).

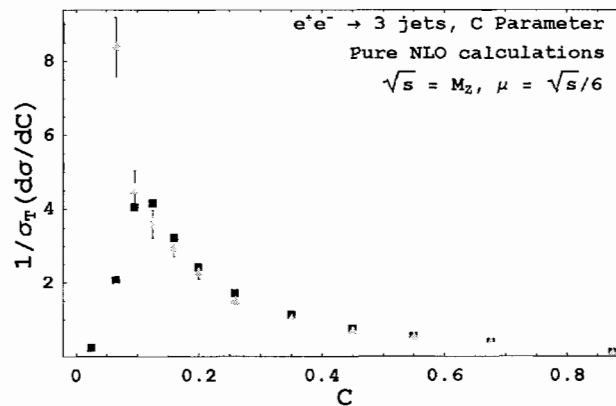


FIGURE 2.25: C-Parameter distribution. Experimental data is compared with the numerical results for pure NLO (91 GeV).

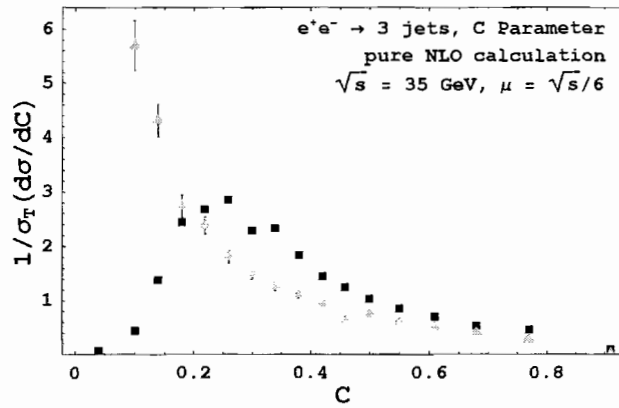


FIGURE 2.26: C-Parameter distribution. Experimental data is compared with the numerical results for pure NLO (35 GeV).

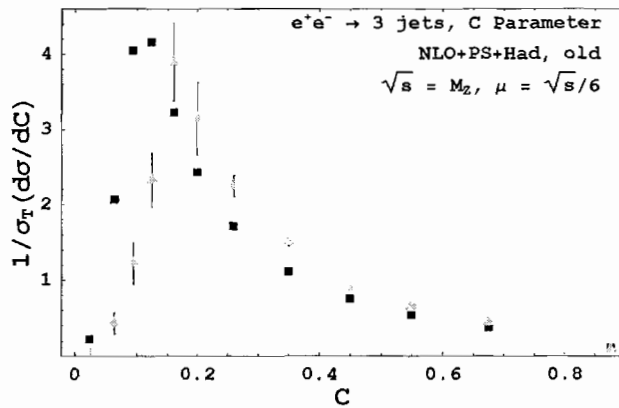


FIGURE 2.27: C-Parameter distribution. Experimental data is compared with the numerical results for NLO + PS + Had with old splitting functions (91 GeV).

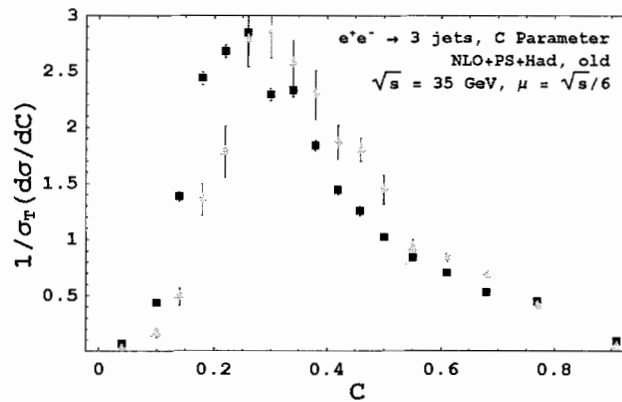


FIGURE 2.28: C-Parameter distribution. Experimental data is compared with the numerical results for NLO + PS + Had with old splitting functions (35 GeV).

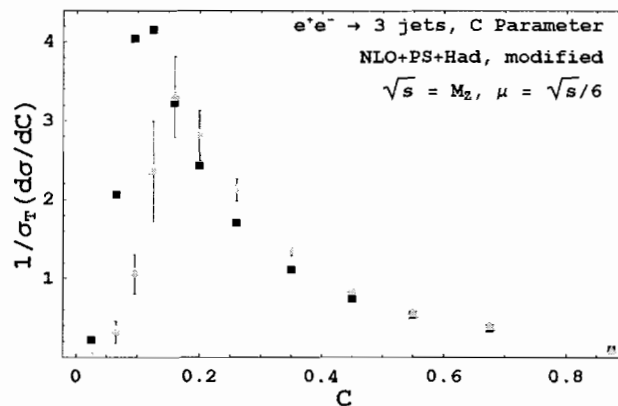


FIGURE 2.29: C-Parameter distribution. Experimental data is compared with the numerical results for NLO + PS + Had with modified splitting functions (91 GeV).

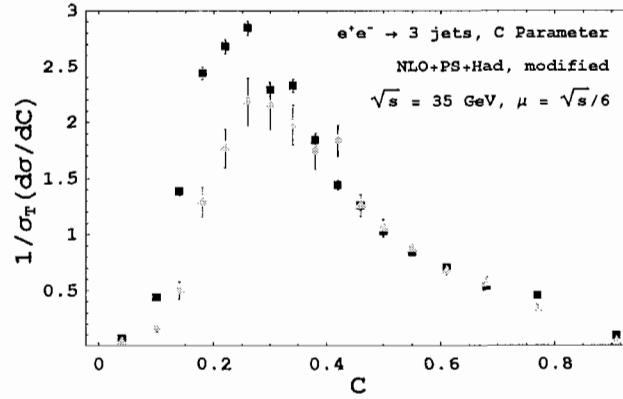


FIGURE 2.30: C-Parameter distribution. Experimental data is compared with the numerical results for NLO + PS + Had with modified splitting functions (35 GeV).

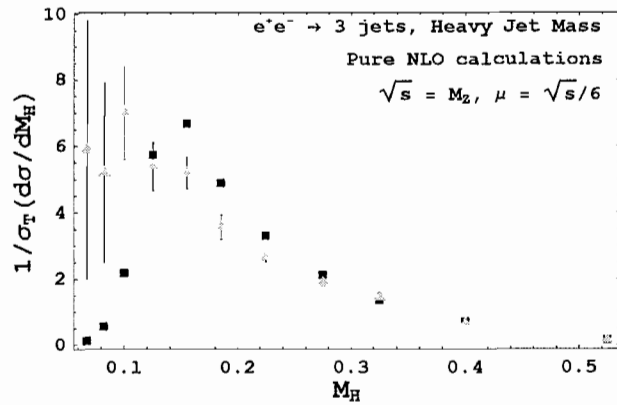


FIGURE 2.31: Heavy Jet Mass distribution. Experimental data is compared with the numerical results for pure NLO (91 GeV).

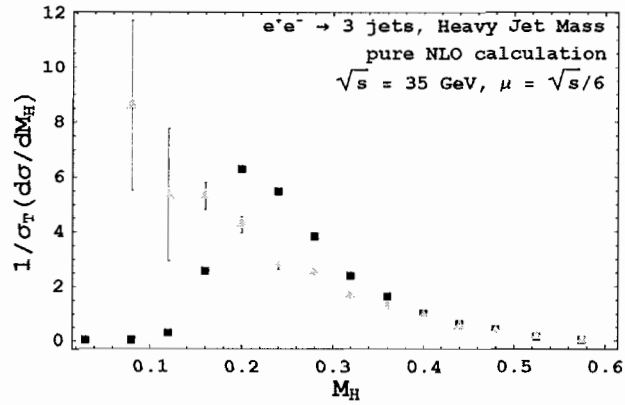


FIGURE 2.32: Heavy Jet Mass distribution. Experimental data is compared with the numerical results for pure NLO (35 GeV).

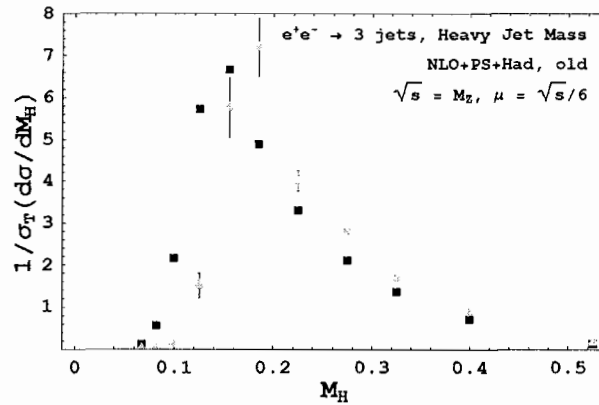


FIGURE 2.33: Heavy Jet Mass distribution. Experimental data is compared with the numerical results for NLO + PS + Had with old splitting functions (91 GeV).

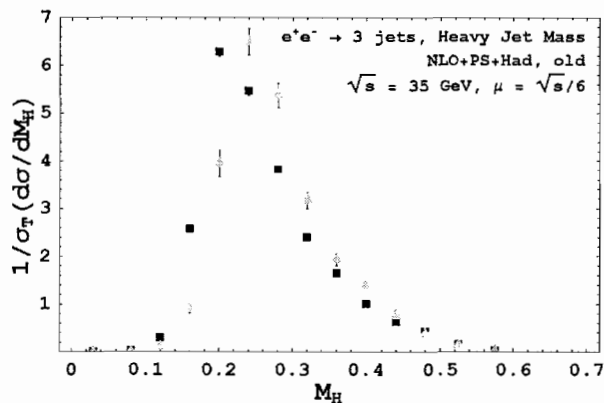


FIGURE 2.34: Heavy Jet Mass distribution. Experimental data is compared with the numerical results for NLO + PS + Had with old splitting functions (35 GeV).

Fig. 2.19 to Fig. 2.48 include experimental data and numerical results acquired by running BEOWULF in different modes, where experimental data points are denoted by black squares and numerical results are denoted by grey triangles. Several conclusions can be drawn from those graphs.

First of all, as expected it can be seen that pure NLO calculations do better at the higher energy, 91 GeV. Predictions made by pure NLO calculations near the 2-jet regions are unphysical because of the failure of cancellation of infrared divergences. Program BEOWULF is designed to handle only events with 3 or 4 jets. The NLO accuracy refers to observables of 3-jet events only, and Feynman graphs with only 2 partons in the final state are not considered. As a result, BEOWULF would generate way too many back-to-back-like events, unlike what really happens in colliders. The direct impact on the numerical calculation of the distribution of 3-jet event shape variable is that the differential cross sections appear to be too large near the 2-jet region, where variables like $1 - T$, C , B_T , B_W and M_H are close

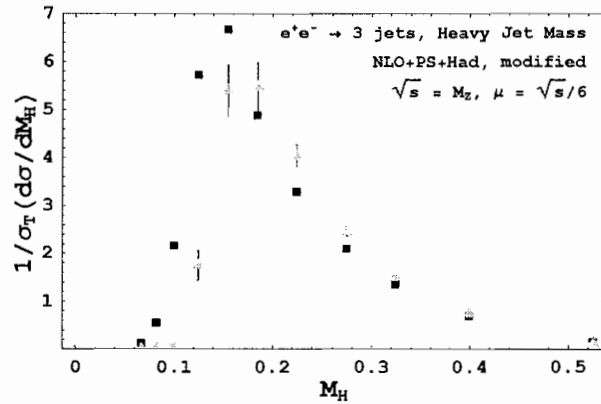


FIGURE 2.35: Heavy Jet Mass distribution. Experimental data is compared with the numerical results for NLO + PS + Had with modified splitting functions (91 GeV).

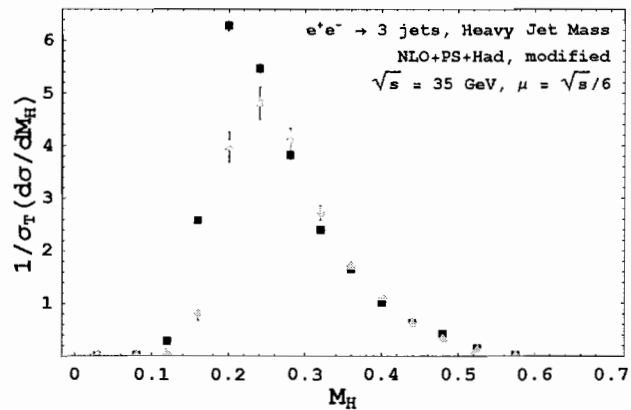


FIGURE 2.36: Heavy Jet Mass distribution. Experimental data is compared with the numerical results for NLO + PS + Had with modified splitting functions (35 GeV).

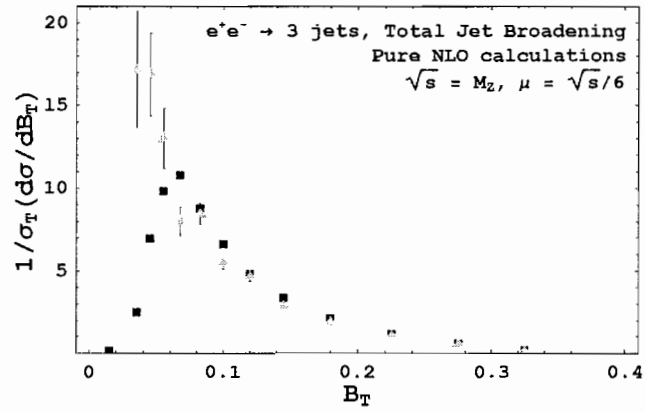


FIGURE 2.37: Total Jet Broadening distribution. Experimental data is compared with the numerical results for pure NLO (91 GeV).

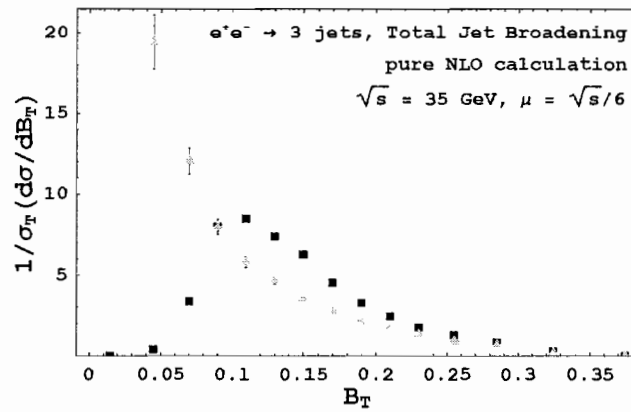


FIGURE 2.38: Total Jet Broadening distribution. Experimental data is compared with the numerical results for pure NLO (35 GeV).

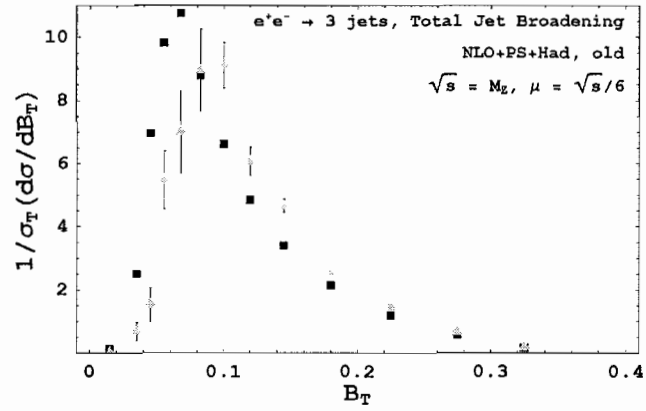


FIGURE 2.39: Total Jet Broadening distribution. Experimental data is compared with the numerical results for NLO + PS + Had with old splitting functions (91 GeV).

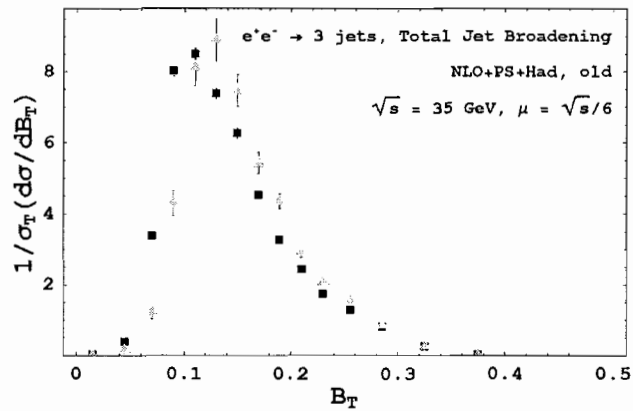


FIGURE 2.40: Total Jet Broadening distribution. Experimental data is compared with the numerical results for NLO + PS + Had with old splitting functions (35 GeV).

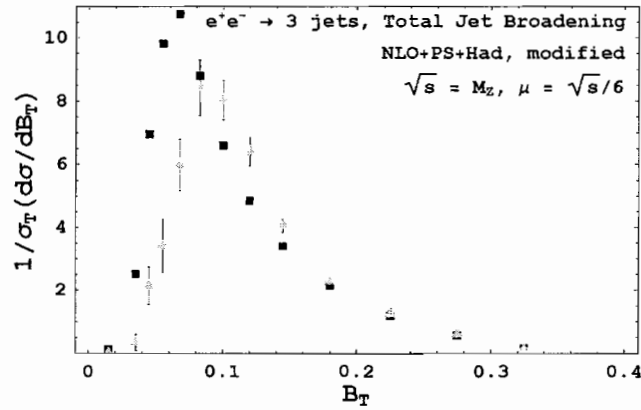


FIGURE 2.41: Total Jet Broadening distribution. Experimental data is compared with the numerical results for NLO + PS + Had with modified splitting functions (91 GeV).

to zero. The 3-jet region is far away from those infrared singularities of Feynman diagrams and pure NLO calculation is supposed to be reliable at energies much higher than the QCD scale ($\Lambda \sim 1$ GeV). However, at low energies, the strong coupling constant gets bigger, and the perturbation expansions of cross sections will eventually break down at the QCD scale. Even at energies not as low as Λ , the perturbative treatment becomes insufficient to model the important long-distance effects, such as parton showers and hadronizations, which only happen long time after the hardest interactions. As foreseen, this discrepancy between pure NLO results and experimental data in the 3-jet region is much more noticeable at $\sqrt{s} = 35$ GeV for almost all event shape variable chosen to be evaluated.

We also made another postulate about the outcome of simulations. Since parton showers and hadronizations can approximately account for the long distance effects when the c.m. energy scale is low, we believe the NLO + PS + Had mode of

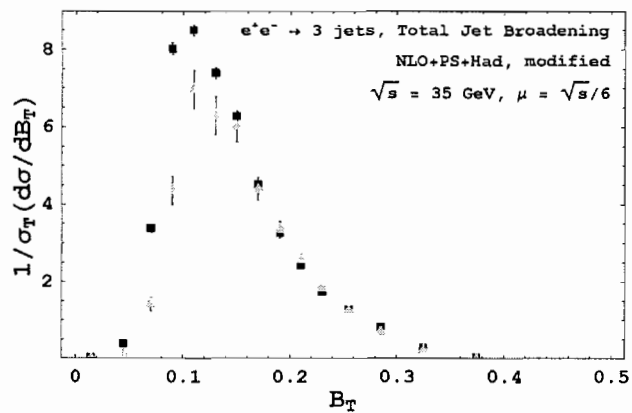


FIGURE 2.42: Total Jet Broadening distribution. Experimental data is compared with the numerical results for NLO + PS + Had with modified splitting functions (35 GeV).

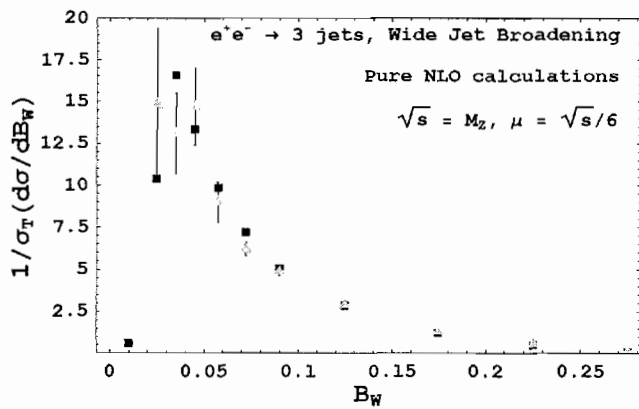


FIGURE 2.43: Wide Jet Broadening distribution. Experimental data is compared with the numerical results for pure NLO (91 GeV).

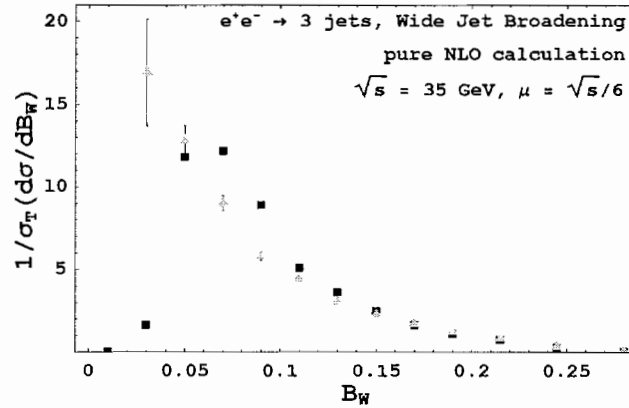


FIGURE 2.44: Wide Jet Broadening distribution. Experimental data is compared with the numerical results for pure NLO (35 GeV).

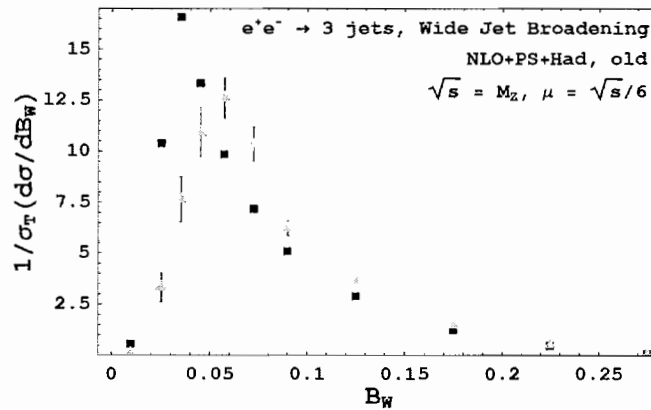


FIGURE 2.45: Wide Jet Broadening distribution. Experimental data is compared with the numerical results for NLO + PS + Had with old splitting functions (91 GeV).

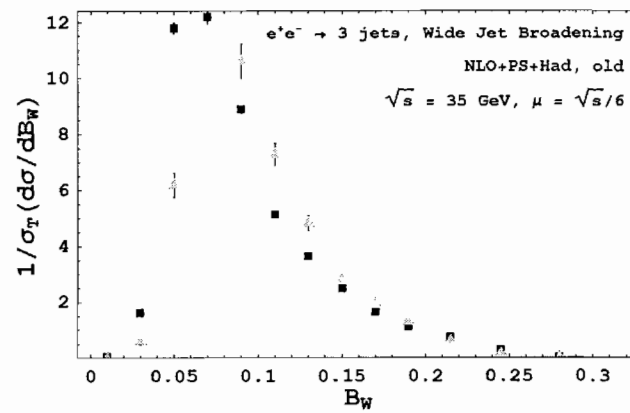


FIGURE 2.46: Wide Jet Broadening distribution. Experimental data is compared with the numerical results for NLO + PS + Had with old splitting functions (35 GeV).

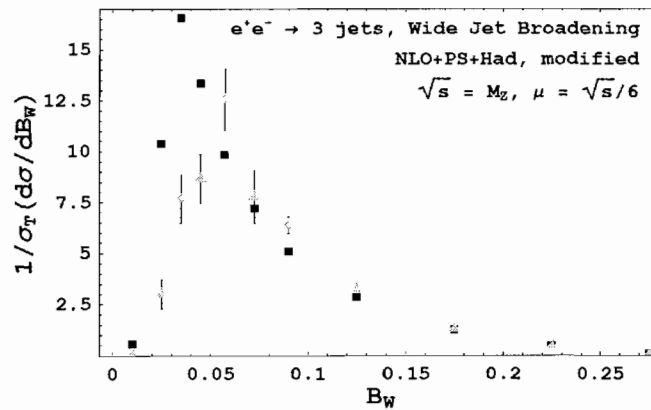


FIGURE 2.47: Wide Jet Broadening distribution. Experimental data is compared with the numerical results for NLO + PS + Had with modified splitting functions (91 GeV).

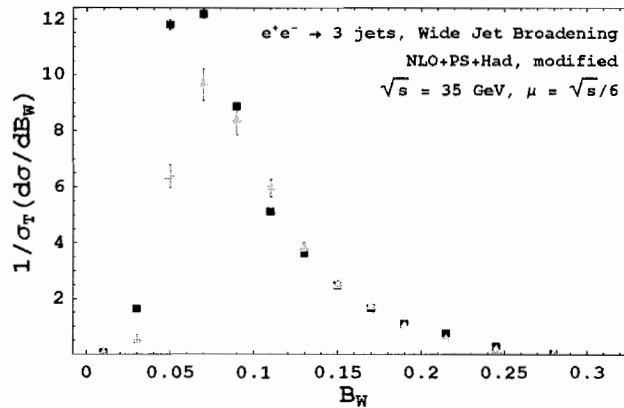


FIGURE 2.48: Wide Jet Broadening distribution. Experimental data is compared with the numerical results for NLO + PS + Had with modified splitting functions (35 GeV).

BEOWULF should be able to produce better results for the distribution of 3-jet event shape variables, especially in the region without those infrared divergences mentioned earlier. We also want to see if the modified splitting functions could make an positive impact on the numerical simulation. Before going into more details, we need to bring up one more point. In NLO + PS + Had, corresponding weights will be given to different 3-parton and 4-parton events after the evaluation of Feynman diagrams. Other relevant information of those events will also be recorded and fed into Pythia for parton showering and hadronizations, such as parton favors, momentum configurations. Due to infrared divergences, the cross sections of generating 2-jet-like events are unphysically large, and thus most events of this type should be abandoned. Based upon this consideration, we set up a hard cutoff on the thrust of events, and all partonic final states will not be sent to Pythia for further evolution if their thrust values are bigger than this cutoff. We can of course benefit

from not including unphysical events in the final calculation, but there could be drawbacks too. For example, there are cancellations of infrared divergences between NLO graphs with 4 cut propagators and NLO graphs with 3 cut propagators plus one virtual loop. By throwing events with big thrust away we might end up with sending events that have huge weights but small thrust values to Pythia, and therefore undermining the convergence of numerical integrations. However, we will not be able to tell how severe this problem can be until we look at the results generated by NLO calculations with hadronizations.

It turns out BEOWULF performs quite differently for different distributions. For the thrust distribution, we display the comparison between simulations and experimental data in Fig. 2.19 – Fig. 2.24. Clearly the differential cross sections produced by NLO + PS + Had are universally bigger than lab measurements in the 3-jet region, for both energy scales and both sets of splitting functions. The long distance effects are overestimated in this case. In Fig. 2.25 – Fig. 2.30, the distribution of C parameter is studied. Again, parton showers with old splitting functions overcorrected the pure NLO calculation and make the cross sections too big in the 3-jet region. The modified parton shower scheme, however, seems to help improve the calculation of differential cross sections by just the right amount at large values of C parameter. We could also see the modified NLO + PS + Had does better at the lower energy, 35 GeV. What happen to the rest of the variables, M_H , B_T , B_W , is very similar to the case of C parameter. The pure NLO calculations fail to model the differential cross sections for these variables correctly in the 3-jet region. Only the modified shower algorithm combined with hadronizations can help, especially for c.m. energy at 35 GeV.

2.7.2 Numerical Convergence

The observation made in last section is a corroboration for our initial postulate on how the pure NLO calculations and different shower schemes would perform with

respect to the evaluation of 3-jet event shape variable distributions. However, as discussed earlier, we still need to examine the convergence of numerical integrations. In other words, the systematic and statistical errors of the numerical results have to be studied before we can make use of any of those to extract useful information, eg., the strong coupling constant α_s .

Program BEOULF has a built-in mechanism to check the convergence of the numerical integrations. Let us take an example the calculation of C parameter of generated events. Roughly speaking, this observable are calculated in BEOULF by taking the sample mean of the C parameter values of all N events. The C parameter value of each individual event is of course supposed to be a random number, and can be affected by many different factors. The events are generated randomly according to a pre-determined distribution, and therefore the C parameter values of N events should be independent and identically distributed. On the other hand, the sample mean of the C parameter values is also a random variable. Central Limit Theorem (CLT) says the sample mean of those C parameters will approach a normal distribution when the sample size $N \rightarrow \infty$, as long as the distribution of individual C parameter value has a finite mean and variance. As a result, we can examine the distribution of the sample mean and draw conclusions about the convergence of the underlying distribution of the C parameter.

To better illustrate what can be done to study the distribution of sample mean, let us consider a random variable X. Generate N samples of X independently according to the same distribution. We call the value of the i^{th} sample x_i . The central moments μ_r of this distribution is defined as

$$\mu_r \equiv \langle (x - \mu)^r \rangle , \quad (2.150)$$

where μ without any index is the expectation value of the random variable,

$$\mu \equiv \langle x \rangle . \quad (2.151)$$

The second central moment μ_2 is also called the *variance*. In a normal distribution

$$P(x) = \frac{1}{\sigma\sqrt{2\pi}} e^{-(x-\mu)^2/(2\sigma^2)}, \quad (2.152)$$

it can be easily proved that the mean of the variable X is μ and the variance is σ^2 . The first and the third central moments of any normal distribution are zero. The second central moment μ_2 by definition is just σ^2 , and the fourth central moment is

$$\mu_4 = 3\sigma^4. \quad (2.153)$$

So, if people want to prove an unknown distribution is normally distributed, they can first calculate both the second and fourth central moment, and see if

$$\mu_4 = 3\mu_2^2 \quad (2.154)$$

is satisfied. The problem is, with finite number of samples we do not know what μ is for this distribution, and further more there is no way to calculate the expectation values of powers of $(x - \mu)$. However, one can always construct unbiased estimators for the second and fourth central moments, and see if the estimators could approximately satisfy Eq. (2.154) when the sample size is large. The reason is according to the Law of Large Numbers, the unbiased estimator of any expectation value should converge to the same expectation value when the sample size increases to infinity.

In our case, the objective is to investigate the distribution of the sample mean of an underlying variable X ,

$$\bar{x} \equiv \frac{1}{N} \sum_{i=1}^N x_i. \quad (2.155)$$

We call this new random variable \bar{X} . In order to construct unbiased estimators of the second and the fourth central moments of \bar{X} , one needs to find out the relations between the central moments of \bar{X} and those of X , and then calculate the estimators

for the distribution of X . Any direct calculation of the unbiased estimators for the central moments of \bar{X} would be practically very unreliable, because usually it takes hours to generate just one sample of \bar{X} , and the estimators will not converge with very few samples. Meanwhile, it only takes ~ 1 micro second to produce a sample of the variable X . Notice that $\langle \bar{X} \rangle = \langle X \rangle = \mu$. By making use of tools such as the characteristic functions of probability distributions, one can derive the following:

$$\mu_2(\bar{X}) = \frac{\mu_2(X)}{N} \quad (2.156)$$

$$\mu_4(\bar{X}) = \frac{3(2N-3)\mu_2(X)^2 + (N^2-3N+3)\mu_4(X)}{N^3(N-1)}. \quad (2.157)$$

If we denote the power sum of variable X with

$$S_k \equiv \sum_{i=1}^N x^k, \quad (2.158)$$

and define

$$m_2 \equiv \frac{1}{N-1} \left(-\frac{S_1^2}{N^2} + \frac{S_2}{N} \right) \quad (2.159)$$

$$m_4 \equiv \frac{1}{(N-1)^2} \left(-\frac{3S_1^4}{N^4} + \frac{6S_1^2 S_2}{N^3} - \frac{4S_1 S_3}{N^2} + \frac{S_4}{N} \right). \quad (2.160)$$

One can show that the expectation values of m_2 and m_4 are equal to the second and the fourth central moment of the distribution of the sample mean of X . As pointed out earlier, this same distribution will approach a normal distribution if the underlying variable X has finite mean and variance. On the other hand, calculating the sample mean of X is in principle equivalent to integrating X over all possible parameter space. This integral converges well is only another way of saying it has finite mean and variance. Therefore, if we find out the following is true when the sample size N is large,

$$m_4 \approx 3m_2^2, \quad (2.161)$$

we would be able to conclude the corresponding integration must have converged well. This is precisely what BEOWULF does to test the convergence of variance numerical integrations, including the calculation of differential cross sections in bins of different event shape variables. For every integral of variable X there is a sample mean \bar{X} , and a pair of unbiased estimator for the second and the fourth central moments of \bar{X} . One can be alarmed by a pair of m_2 and m_4 that cannot even remotely satisfy Eq. (2.161) if there is something wrong with the cancellation of divergences. When calculating those event shape variables whose distributions are plotted somewhere between Fig. 2.19 and Fig. 2.48, we observe that from time to time m_4 is twice or three times bigger than m_2 .

The marginal convergence of some differential cross sections is inherent with the way we treat Feynman graphs in BEOWULF. At leading order, only events with 3 partons are included and further showered. However, the LO graph with 3 cut propagators becomes divergent when two of them that come out of the same uncut propagator become collinear with each other. It means events with large thrust and 3 partons will be generated at an unphysically high rate, or equally, generated with unphysically large and positive weights. There would not be any problem if all Feynman diagrams are included, because events from the LO graph with only two cut propagators and one virtual loop can have large and negative weights, and hence eliminate the divergence when the total cross section of $e^+e^- \rightarrow hadrons$ is calculated. However, events of the second type are ignored and discarded, because BEOWULF is designed to deal with events with 3 hard partons or more. Points of finite values in the Monte Carlo integration with huge and unbalanced weights are equivalent to points with large values. As a result, after primary splittings, BEOWULF will produce many events with large and positive weights near the two-jet region, and we have to make a hard cut-off on the thrust values of events. The motive is to get rid of those unphysical events and have finite total cross section when normalizing the differential cross sections. However, many events of this type

with thrust values slightly smaller than the cut-off would still be sent to PYTHIA. After further showering and hadronization in PYTHIA, a portion of those events can get broadened, and their values of event shape variables could be comparable to those real 3-jet events. These events that have very large thrust values before parton showering possess unbalanced positive weights, and hence will make the differential cross sections higher than what they should be in the 3-jet region. For interactions at $\sqrt{s} = 91$ GeV, the long-distance effects are weaker than those at $\sqrt{s} = 35$ GeV, and as we see, parton showers overshoot and make the simulation results deviate further away from the experimental data in the 3-jet region.

CHAPTER III

COLORFUL QUANTUM BLACK HOLES

3.1 Introduction

The Standard Model of particle physics is perhaps the most successful physics theory up until now. It unifies the Maxwell's theory of electromagnetism and the Weak Interaction, describes the strong interaction as a non-Abelian gauge field, and yields many theoretical predictions that have been matched with experimental data to very impressive accuracy. As a very powerful field theory, Standard Model has its own limitations. The theory has too many input parameters to be adjusted. In addition, the mechanism responsible for breaking the electroweak symmetry and generating particle masses in this model is not yet fully understood. The mass of neutrinos cannot be explained; Higgs boson mass, which is only of order 10^2 GeV, receives quantum corrections that are sensitive to the cut-off scale ($\sim 10^{19}$ GeV), and thus seems to be radiative unstable. The Large Hadron Collider (LHC) has been built to help physicists tackle those problems, which is able to constantly smash proton-proton beams at a c.m. energy $\sqrt{s} = 14$ TeV. At this scale, we should be able to reveal the real scheme that breaks the electroweak symmetry, and as a result, solve the hierarchy problem.

There have already been various candidates that could stabilize the hierarchy m_{EW}/M_{Pl} , such as Supersymmetry and Extra Dimensions. Our project is to explore one bold and yet possible outcome, the production of quantum black holes at the LHC, assuming there are indeed compactified extra dimensions in addition to ordinary 4-dimensional spacetime. It will be explained how we attempt to constrain

the decay of black holes created in a proton collider. However, it would be worthwhile to first say a bit more about the origin of extra dimension scenarios, the reason behind their revival, and how they give rise to the possibility of producing micro black holes.

3.2 Extra Dimensions

3.2.1 Kaluza-Klein Theory

In the early 20th century, people discovered that five-dimensional spacetime can be splitted into the Einstein equations and Maxwell equations in four dimensions, which was an attempt to unify gravity and electromagnetism. Oscar Klein later suggested the fifth dimension can be curled up in a extremely small circle, so that a particle will come to its original position very shortly if it travels along this extra dimension. The distance a particle can move before returning to where it started is defined as the size of the extra dimension. People call extra dimensions of this type a compact set, and call the phenomenon of a spacetime having compact extra dimensions *compactification*. From an experimentalist's view, the compact fifth dimension can be tested. Standing waves should be allowed to exist, and have an energy spectrum

$$E_n = nhc/R , \quad (3.1)$$

where R is the size of the extra dimension, h is the Planck's constant, c is the speed of light and n is a positive integer. This set of energies corresponds to the mass spectrum of a set of resonance, and we call this spectrum the *Kaluza-Klein Tower*. In particle reactions those standing waves can in principle be produced through resonance, and can at the same time be identified in the particle detectors as missing energies that could fill in the Kaluza-Klein Tower.

Kaluza-Klein theory has a very elegant geometric presentation, but it was forgotten not long after it was first invented, because it ran into a series of problems and was not able to be converted to a realistic model. For example, fermions must be introduced in an artificial way in the Kaluza-Klein theory, unlike the modern standard model where fermions obey various gauge symmetries and have to be sorted in a specific fashion. The existence of new generations of fermions can even be predicted in order to explain CP violation within the framework of standard model. It would be great if the standard model of particle theory could be embedded into the beautiful geometry of Kaluza-Klein theory.

3.2.2 The Hierarchy Problem

In standard model, the hierarchy between the electroweak scale m_{EW} and an ultraviolet cut-off scale Λ_{UV} is large, because Λ_{UV} is usually considered to be the Planck scale,

$$M_{\text{Pl}}^{D-2} \equiv \frac{(2\pi)^{D-4}}{4\pi G V_{D-4}}, \quad (3.2)$$

where D is the dimension of spacetime, G is the Newton's constant, and V_{D-4} is the volume of the compact space. As a result, the Higgs boson mass is radiatively unstable, since it receives quadratically divergent quantum corrections through the coupling between ordinary fermions and the Higgs boson. In supersymmetric models, super partners of standard model particles are proposed to stabilize the hierarchy problem. For every standard model fermion, there is a scalar particle as its super partner. Those scalars are coupled to the Higgs boson in a way such that the corresponding corrections to the Higgs boson mass will exactly cancel the corrections induced by virtual standard model fermions. However, supersymmetry is not apparent based upon existing experimental data, and thus the mechanism that breaks supersymmetry needs to be studied.

Compared to the approach of supersymmetry, the solution to the hierarchy problem in extra-dimensional theories seems trivial. In such theories, there is only one fundamental scale, instead of two. The standard model theory is only valid up to the electroweak scale. Gravitational effects will become important beyond that scale, and the ordinary $SU(3) \times SU(2) \times SU(1)$ field theory will break down. Simply by construction there is no such thing as severe hierarchy between the electroweak scale and the ultraviolet cutoff scale. In fact, whether the hierarchy problem can really be resolved in such a straightforward way depends on if one can lower the Planck scale to the Tera electron volt (TeV) scale.

It is worthwhile to define the Planck scale first. In quantum mechanics, the smallest scale of localizing a particle is this same particle's Compton's wavelength. Compton's wavelength of a particle is equivalent to the wavelength of a photon whose energy is equal to the rest mass m of that particle,

$$\lambda_c = \frac{h}{mc} . \quad (3.3)$$

According to the Heisenberg Uncertainty Principle, if we use a light of certain wavelength to measure the position of some particle, the momentum and the position of that particle obeys the following:

$$\Delta x \cdot \Delta p > \hbar/2 , \quad (3.4)$$

which can be also written down as a lower limit for Δp :

$$\Delta p > \frac{\hbar}{2\Delta x} . \quad (3.5)$$

The uncertainty in particle momentum can not be infinitely large, either. Because as soon as $\Delta p > mc$, the energy of the particle would become greater than the threshold of creating a new particle of the same type, which is equal to the rest mass mc^2 , and the measurement of the position of the original particle would be undermined. In

quantum field theory this argument is qualitatively justified, and photons can indeed create a pair of fermions as long as the photon energy is larger than the rest mass of the two fermions. After we put this constraint for Δp in Eq. (3.5), immediately we will have

$$\Delta x > \frac{\hbar}{2mc}, \quad (3.6)$$

which is equivalent to saying the smallest length scale a particle can be localized is its Compton's wavelength, up to a factor of order 1. On the other hand, let us consider a black hole of mass M_{BH} . Assume this black hole is not rotating and spherically symmetric for simplicity. All the massive material is trapped behind its event horizon, which is a spherical surface of radius equal to the Schwarzschild radius

$$r_S = 2GM_{BH}/c^2, \quad (3.7)$$

where G is the Newton's gravitational constant. However, the size of the black hole can not be smaller than its own Compton's wavelength, otherwise the quantum fluctuation of the massive material that forms the black hole will overrule the gravitational effects, and the black hole will disappear instantly as the massive material can no longer be trapped behind the event horizon. Combined with Eq. (3.7), this argument leads to

$$M_{BH} > \sqrt{\hbar c/G} \quad (3.8)$$

up to a factor of order 1. This smallest mass of a black hole is defined as the *Planck mass*, M_{Pl} , and the *Planck scale*, $\sim 10^{19}$ GeV, corresponds to the Planck mass by the mass-energy equivalence.

In extra-dimensional models, the Planck scale can be much lower than 10^{19} GeV if the size of the extra dimensions is large. A well-accepted argument that supports this claim is given in [21] by Arkani-Hamed, Dimopoulos and Dvali in 1998. Assume

a model with 4 ordinary spacetime dimensions and n compactified extra dimensions. Intuitively speaking, the gravitational field can be diluted by the n extra dimensions. It is possible that at TeV scale the gravity has already become as important as the gauge forces if we take all dimensions into account. Suppose the standard model fields can only propagate in the ordinary 3 spatial dimensions but gravitational field can freely propagate in all spatial dimensions, then the gravitational field would still look much weaker than the other forces in the ordinary 3 spatial dimensions. It means the Planck scale that is induced from measuring the effective gravitational coupling G_N in the ordinary 3 spatial dimensions could be much higher than what the real Planck scale should be.

Let us perform a rough quantitative analysis (see [21] for more details). The Planck scale $M_{Pl} = G_N^{-1/2}$ if we adopt the system of units in which $\hbar = c = 1$. The Gauss's law is approximately right with 3 spatial dimensions, and the gravitational potential between object of mass m_1 and another object of mass m_2 is

$$\begin{aligned} V(r) &\sim G_N \frac{m_1 m_2}{r} \\ &= \frac{m_1 m_2}{M_{Pl}^2} \frac{1}{r}. \end{aligned} \quad (3.9)$$

If there are n compactified extra dimensions of size R , for length scale far smaller than R , the n extra dimensions would not be very different from the ordinary 3 spatial dimensions. The Gauss's law should be modified accordingly by first putting in a new factor of $1/r^n$, because the Gaussian sphere now has n more dimensions. The gravitational potential should remain linear with the masses of individual field sources. Using dimensional analysis, there should also be a new factor of $1/M_{Pl}^n$, and hence we have

$$V(r) \sim \frac{m_1 m_2}{M_{Pl(4+n)}^{2+n}} \frac{1}{r^{n+1}}, (r \ll R), \quad (3.10)$$

where $M_{Pl(4+n)}^{2+n}$ is the true Planck scale in $4 + n$ dimensions. In comparison, at a

distance scale much larger than R , the compactified dimensions are almost invisible, and the Gauss's law for gravitational potential should have the same r dependence as that in Eq. (3.9). Matching the two different expressions for gravitational potential at the boundary $r = R$, one can derive the following for $r \gg R$:

$$V(r) \sim \frac{m_1 m_2}{M_{Pl(4+n)}^{2+n}} \frac{1}{R^n r}, (r \gg R), \quad (3.11)$$

and thus the effective Planck scale M_{Pl} in $4D$ spacetime can be expressed in terms of $M_{Pl(4+n)}$. The relation between the effective scale and the true scale is simply

$$M_{Pl}^2 = M_{Pl(4+n)}^{2+n} R^n. \quad (3.12)$$

If we let $M_{Pl(4+n)}$ be of order 10^3 GeV, which is the scale of m_{EW} , the hierarchy problem can be solved naturally. We also want to push the effective Planck scale (M_{Pl}) up to the measured value ($\sim 10^{19}$ GeV), and as a result one would derive

$$R \sim 10^{\frac{30}{n}-17} \text{cm} \times \left(\frac{10^3 \text{GeV}}{m_{EW}} \right)^{1+\frac{2}{n}}, \quad (3.13)$$

where n is the number of extra compactified dimensions. From here we will use M_D instead of $M_{Pl(4+n)}$ to denote the Planck scale in $4+n$ dimensions. Notice that R has to be smaller than the smallest length scale (~ 1 cm) at which Newton's law of gravity can be tested in any available experiments, otherwise we would have already observed deviations. The case of $n = 1$ has been ruled out because it corresponds to $R \sim 10^{13}$ cm. For scenarios with $n \geq 2$, the size of the compactified dimensions would be smaller than 1 mm, and thus they are still in play. It is well motivated to question the validity of Newtonian gravity at distance smaller than 1 cm. The present Planck scale is only extrapolated from current measurements, and it corresponds to 10^{-33} cm. Believing the real Planck scale to be $\sim 10^{18}$ GeV is no different from believing nothing happens to the gravity between the above two widely separated scales.

The Kaluza-Klein theory has been revived in this way, with many new elements added in. People have invented theoretical techniques to prevent standard model

fields from leaking into the compactified dimensions, and therefore the modern versions of extra dimension theories can possess realistic particle contents that were missing from the original theory. One of the most well-known extra-dimensional scenarios that encompass the standard model is *ADD*[21], and another one is the *Randall-Sundrum* (RS) model [22]. We will adopt these two scenarios when we investigate quantum black holes later.

3.3 Black Hole Formation at the LHC

An important consequence of using extra dimensional models to explain hierarchy problem is that black holes may be able to form at a much lower scale than what people thought. If the Planck scale were to be proved to be actually close to 1 TeV, black holes with masses greater than 1 TeV can exist despite quantum fluctuations. People even suggest black holes can be produced colliding proton pairs at the Large Hadron Collider (LHC) which runs at a c.m. energy of 14 TeV, based on the hoop conjecture. The hoop conjecture was first proposed by Kip Thorn[23] in 1972, and states:

An imploding object forms a black hole when, and only when, a circular hoop with a specific critical circumference could be placed around the object and rotated . . . , and the critical circumference is given by 2 times π times the Schwarzschild radius corresponding to the object's mass.

According to the hoop conjecture, as long as the impact parameter b is larger than 2 times the Schwarzschild radius corresponding to the mass of the two colliding protons at the LHC, a small black hole would be formed. This is illustrated in Fig. 3.1.

Black holes of astrophysical size are supposed to evaporate into all available fields through Hawking radiation. Typical Hawking radiation of such a macroscopic black hole is believed to be democratic in a sense that the particle production rates are independent of their flavors. It is very different from any Standard Model decay process where gauge symmetries put tight constraints on what the final states can be.

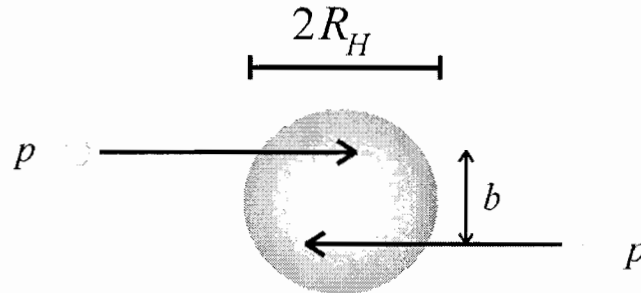


FIGURE 3.1: Two protons forming a black hole inside the Large Hadron Collider.

Naturally, the next question would be whether black holes can really be observed at the LHC given the Planck scale has been lowered to ~ 1 TeV. The answer should have several layers. We shall start with discussing the effects of *Initial-state Radiation* (ISR).

3.3.1 Initial-State Radiation and PDFs

If black holes can be created at the LHC, their masses should at least be greater than the Planck scale, $M_D \sim 1$ TeV. The size of the black hole, or the Schwarzschild radius of the corresponding event horizon, will be of the order of $(100 \text{ GeV})^{-1}$. This is much smaller than the size of a proton, which is of the order of $\Lambda_{\text{QCD}}^{-1}$ ($\Lambda_{\text{QCD}} \sim 1$ GeV). It indicates the black holes, if there are any at the LHC, would be formed by quarks and gluons inside the protons, instead of being formed directly by protons. The hard interaction responsible for the black hole formation will probe the structure of protons at scales from a few hundred GeV to a few TeV. Under this circumstance, the radiation in the initial state becomes very important, and a considerable amount of c.m. energy of the proton pair will be lost in this way before partons get close enough to each other and create an event horizon.

In QCD, the effects of IR are incorporated into the DGLAP evolution of *parton distribution functions* (PDF) as the scale of the eventual transverse interaction varies. An example is the parton distribution function for an up quark inside a proton, $f_u(x, Q)$, which expresses the probability the proton probed at scale Q contains an up quark of longitudinal momentum fraction x . Since the black holes are believed to be created at the parton level, the particle level cross section will have to be the parton level cross section convoluted with the PDFs. To address this issue more clearly, let us first define the momentum fractions of the two incoming partons to be x_a and x_b . If the c.m. energy of the initial proton pair is \sqrt{s} , then the energy actually available for producing the energy would be

$$\hat{s} = sx_ax_b \equiv su , \quad (3.14)$$

where the new parameter u is defined. Taking both general relativity and quantum fluctuations into account, we should have the threshold $\hat{s} \geq M_D^2$. The full particle level cross section σ can then be calculated as the following:

$$\begin{aligned} \sigma_{pp \rightarrow BH+X}(s) &= \sum_{a,b} \int_{\frac{M_D^2}{s}}^1 dx_a \int_{\frac{M_D^2}{sx_a}}^1 dx_b f_a(x_a, Q) f_b(x_b, Q) \cdot \\ &\cdot \hat{\sigma}_{ab \rightarrow BH}(M_{BH}^2 = \hat{s}) , \end{aligned} \quad (3.15)$$

where $\hat{\sigma}_{ab \rightarrow BH}(M_{BH}^2 = \hat{s})$ is the parton level cross section of creating a black hole of mass M_{BH} , and we will discuss this cross section later. Both a and b are the parton types in the two initial protons, and the sum run over all possible pairings of quarks and gluons. The scale Q at which PDFs are evaluated is determined by the inverse length scale of the interaction. For perturbative hard scattering in a local field theory, this momentum scale is the momentum transfer, and in an s-channel reaction it is just the c.m. energy $Q \sim \sqrt{\hat{s}}$. For a non-perturbative s-channel process in the black hole formation of classic general relativity, it makes sense to take the size of the horizon as the relevant scale, and $Q \sim r_s^{-1}$ [24]. Apparently there are two

competing effects when producing a black hole in this way. Intuitively, the parton level cross section of black hole production should become larger as the black hole mass increases, because the corresponding Schwarzschild radius gets bigger as more energy is trapped behind the event horizon. On the other hand, the PDFs fall rather rapidly at high energies as any single parton demands more energy from its mother proton, due to more severe energy loss through initial-state radiation. It turns out, without giving any proof here, the effects of the drop of PDFs dominates, and the consequence is most of the black holes will be created at the threshold, with the c.m. energy of the proton system fixed.

We can write the particle cross section above in a more convenient form for later use. Make a variable change by replacing x_a and x_b with u and v . As defined earlier, $u \equiv x_a x_b$. Let $v \equiv x_b$. Straight forwardly, we will have

$$\begin{aligned} \sigma_{pp \rightarrow BH+X}(s) &= \int_{\frac{M_D^2}{s}}^1 du \int_u^1 \frac{dv}{v} \sum_{a,b} f_a(u/v, Q) f_b(v, Q) \cdot \\ &\quad \cdot \hat{\sigma}_{ab \rightarrow BH}(M_{BH}^2 = \hat{s}) . \end{aligned} \quad (3.16)$$

3.3.2 Inelasticity

In the previous section, we have naively taken the mass trapped the event horizon to be equivalent with the parton c.m. energy $\sqrt{\hat{s}}$. This is a poor approximation, considering the fact a great non-negligible portion of $\sqrt{\hat{s}}$ will escape in gravitational waves even at impact parameter $b = 0$. We have not specified any form for the parton level cross section of black hole formation, either. We will discuss this particular cross section in the current section, which will account for the inelasticity inherent in the grazing collisions of high energy particles.

Based upon the hoop conjecture, naively one would suggest using the geometric cross section

$$\hat{\sigma} = \pi r_s^2 \quad (3.17)$$

as the parton level cross section. However, the shape of the horizon would not be a perfect circle as a result of a grazing collision, and therefore Eq. (3.17) would not be accurate enough for computational purposes. Yoshino and Nambu [25] quantified the inelasticity $y \equiv M_{BH}/\sqrt{\hat{s}}$ using a system originally set up by D'Eath and Payne [26], and derived lower bounds on y , as a function of the number of extra dimensions n and the impact parameter b . Qualitatively an inelasticity $y < 1$ means there is even less energy available for producing a black hole, and the chance of finding a black hole with mass much greater than the threshold is even more slim. Another implication is that the parton level cross sections should be weighted by their impact parameters when calculating the particle level cross sections. If modifying Eq. (3.16) accordingly, one can get the following:

$$\begin{aligned} \sigma_{pp \rightarrow BH+X}(s, n, M_D) &= \int_0^1 2z dz \int_{\frac{M_D^2}{y^2 s}}^1 du \int_u^1 \frac{dv}{v} F(n) \pi r_s^2(us, n, M_D) \cdot \\ &\cdot \sum_{a,b} f_a(u/v, Q) f_b(v, Q) , \end{aligned} \quad (3.18)$$

where $z = b/b_{\max}$, and $F(n)$ is the form factor that accounts for the deviation of the shape of the horizon from a perfect sphere. We use the numerical values provided in [25]. In addition, r_s is the Schwarzschild radius of the horizon in $(4+n)$ dimensions. The exact definition of r_s depends on the normalization convention for the Planck scale, and we will use the following,

$$r_s(us, n, M_D) = k(n) M_D^{-1} [\sqrt{us}/M_D]^{1/(1+n)} , \quad (3.19)$$

where

$$k(n) \equiv \left[2^n \sqrt{\pi}^{n-3} \frac{\Gamma[(n+3)/2]}{n+2} \right]^{1/(n+1)} . \quad (3.20)$$

Although the numerical lower bounds for the inelasticity y is used in Eq. (3.18), one should keep it in mind that the particle level cross sections calculated in this way are only rough estimates. A real calculation involving the grazing collision of high energy particles should take effects of true quantum gravity into account, since we are indeed discussing the black holes near the threshold.

3.3.3 Semi-Classic Black Holes

People have been studying black holes of astrophysical size for years using general relativity. For a black hole that might potentially be produced during a proton-proton collision, there must be important quantum effects involved. The best way to tell whether a black hole has been produced in the collider is to look for its decay products, and people can only attempt to make predictions for the decay of such black holes using semi-classical analysis in the absence of a theory of real quantum gravity. Obviously, several criterions have to be satisfied in order to justify this kind of approach, and any black hole that meets the criterion given next would be a truly thermal black hole.

Most people would agree that a black hole can be produced if the c.m. energy of the system E is much larger than the higher-dimensional Planck scale M_D . It remains to be ambiguous at which exact scale a black hole could be formed. Planck scale is only a lower limit of the real threshold of black hole creation. For this purpose, we use a parameter, x_{\min} , to describe the relation between the threshold and the fundamental scale of gravity, and

$$x_{\min} \equiv M_{\min\text{BH}}/M_D . \quad (3.21)$$

where $M_{\min\text{BH}}$ is the mass of a black hole at the threshold.

Black holes that are often studied are a derivative of the Einstein's theory of gravity, and they are usually thermalized, which means those black holes can reach an internal thermal equilibrium. Let us get a sense of what x_{\min} could be if all

possible black holes have to be thermalized. More detailed analysis can be found in [27]. For such a black hole, the initial entropy S_0 of course has to be large enough to ensure a well-define thermodynamic description [28]. More specifically, the following needs to be satisfied:

$$|\partial T_{BH}/\partial M| \ll 1, \quad (3.22)$$

which is another way of requiring the change in the Hawking temperature is small per particle emission. This particular criterion yields $x_{\min} \sim 1$ for both *ADD* and *RS*. A similar but stronger constraint could come from restricting the energy carried by any individual degree of freedom in a thermal bath to be much smaller than the total energy:

$$|\partial M_{BH}/\partial N| \ll M_{BH}. \quad (3.23)$$

This second criterion can be satisfied in both *ADD* and *RS* if $x_{\min} \geq 2$ [27].

In addition, the life time τ of a semi-classical black hole should be large compared to its inverse mass, M_{BH}^{-1} , so that the black hole can behave as a well-defined resonance [29]. It is found in [27] that this criterion is satisfied for $x_{\min} \sim 1.3$ in *ADD* and for $x_{\min} \sim 1.6$ in *RS*.

Another possible constraint on the mass threshold for thermal black holes comes from a concern on the set up of the extra-dimensional model. The black hole mass should be large compared to the 3-brane tension so that the brane does not significantly perturb the black hole's metric [29]. The value of an appropriate x_{\min} largely depends how exactly the standard model is localized in the ordinary *4D* spacetime, and thus in this article we will not use this criterion to put limits on x_{\min} .

Furthermore, when a truly thermal black hole decays on the brane, it should be able to re-equilibrate itself as it decays [27]. It qualitatively means the lifetime of the black hole should be greater than the radius of the event horizon. In *ADD*, it is

necessary to let $x_{\min} \geq 3$ in order to satisfy this condition, while any values of x_{\min} works well in RS.

Based on the above analysis, it is straight forward to conclude that $x_{\min} \approx 3$ is favored as the ratio of the minimum thermal black hole mass to the Planck scale, under the normalization convention for the Planck scale we adopted. As discussed earlier, most black holes will be generated near the threshold, if we also take into account the drop of PDFs at high energies and the inelasticity of grazing collisions. A $x_{\min} \approx 3$ says the semi-classical black hole production rate would be far less than the rate with the threshold to be simply the Planck scale itself. This argument will be confirmed in our numerical results presented later in this article. For now we only want to stress the fact that most events involving strong gravitational effects might not even be able to be separated from the Standard Model background, because their decay products would probably lack the dramatic characteristics of the final state of a typical thermal black hole.

It is worthwhile to investigate proton reactions with energies greater than the Planck scale but smaller than the threshold of creating thermal black holes. Before that, it is helpful to figure out the average number of particles an ordinary black hole could emit. One can extrapolate from such semi-classical analysis and get a sense of what those “intermediate” “bound states” would look like. During a typical Hawking radiation, a black hole would lose its mass through emitting particles. The Hawking temperature of such a black hole can be related to its Schwarzschild radius in the following way:

$$r = \frac{1+n}{4\pi T_{BH}} = \frac{k(n)}{M_D} \left(\frac{M}{M_D} \right)^{\frac{1}{1+n}}, \quad (3.24)$$

where n is the number of compactified dimensions. Not surprisingly, the Hawking temperature plays a significant role in determining the properties of black hole decay. The average emission rate for various particle species from a black hole, or the change in the average multiplicity $\langle N \rangle$, can be expressed in terms of the Hawking

temperature. The change in the black hole's mass can also be related to the Hawking temperature, radius and some other relevant quantities. Without much difficulty, one can combine the two above rates together and derive the average multiplicity $\langle N \rangle$ in terms of the mass of the same black hole, so that we would get an idea of roughly how many particles can be found after the decay. After the dust has settled, we have [29]

$$\langle N \rangle = \frac{4\pi\rho k(n)}{2+n} \left[\frac{M_{BH}}{M_D} \right]^{\frac{2+n}{1+n}} = \rho S_0, \quad (3.25)$$

where S_0 is the initial entropy of the black hole,

$$S_0 = \left(\frac{1+n}{2+n} \right) \frac{M_{BH}}{T_{BH}}. \quad (3.26)$$

It makes sense that we can derive a relation where the multiplicity of the black hole is proportional to its entropy, since the entropy of an arbitrary object is in principle a measure of the number of its possible microscopic configurations. The function $k(n)$ has been defined in Eq. (3.20). For function ρ , we only need to know it is determined by the Hawking temperature, the internal degrees of freedom of different particle species, and the statistical properties of all available particles that can be emitted. It accounts for the backscattering of part of the outgoing radiation into the black hole. In [29], ρ is calculated to estimate the average multiplicity. It is found that $\langle N \rangle \approx 0.30 M_{BH}/T_{BH}$, which is about a factor of 3 times smaller than the initial entropy.

We can assume the semi-classical black holes with thermally distributed final state particles obey Poisson distribution. Then $\langle N \rangle$ becomes the expectation value of the Poisson distribution. Based upon the above assumption, we can roughly compare the relative abundances between low-multiplicity events and high-multiplicity events by simply using

$$P_i = e^{-\langle N \rangle} \frac{\langle N \rangle^i}{i!}, \quad (3.27)$$

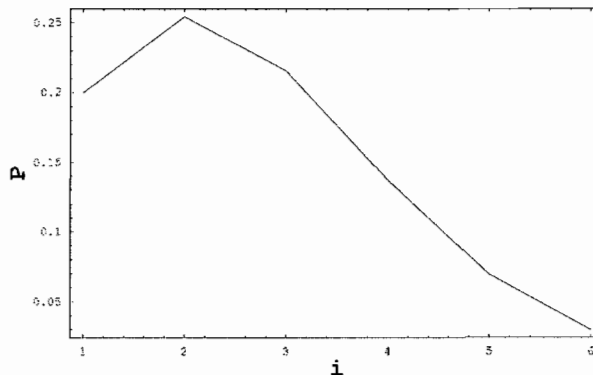


FIGURE 3.2: Distribution of the number of final-state particles of a black hole if a Poisson distribution is assumed.

where i is the actual number of final-state particles in a single event, and P_i is the probability of finding an event with exactly i particles in the final states. The case of $i = 0$ and 1 can be neglected for physics reasons, because it is hard to imagine either a black hole vanishes without radiating or a tiny black hole stays stable without decaying. As an example, we set $x_{\min} = 2$. We then focus on the black holes with masses exactly twice the extra-dimensional Planck scale, and study the probability distribution of the number of final-state particles. According to last paragraph, we would have $\langle N \rangle \approx 1.15$. The Poisson distribution with this average multiplicity is given in Fig. 3.2.

From this plot, the least one can conclude is that it is very unlikely for a black hole with mass $M_{BH} = M_D$ to produce a “fireball” explosion with a high multiplicity isotropic distribution of final-state particles. If we unitarize the probability distribution by adding P_0 and P_1 to P_2 , we can even say that 2-particle events dominate. These arguments can be generalized to black holes with $M_D < M_{BH} < 3M_D$. As a comparison, the black hole mass has to be a factor of

3 times larger than the extra-dimensional Planck scale in order to yield an average multiplicity around 4. We can get to a very similar conclusion by analyzing the phase space of final states with different numbers of particles, and the domination of 2-particle events is still favored because the phase space of more final-state particles is strongly suppressed.

Most of the previous studies used high multiplicity as the signature of finding a thermal black hole at the LHC. However, we think this approach is impractical since the proton pairs at the LHC will mostly form black holes at lower energies and with low multiplicity, if there were any. Those black holes will not qualify as truly thermal black holes as their masses are below the semi-classical threshold. They are probably not even real black holes. It would be more precise if we call them “bound states”. Nevertheless these states should exhibit significant gravitational effects. It seems plausible to us that some of the properties of such states can be extrapolated from a thermal black hole. We will call such “bound states” *quantum black holes* (QBHs) from now.

In order to verify the production of QBHs at the LHC, we need to make a few assumptions about how it would decay. Thorough study shows that a black hole of astrophysical size usually goes through several stages before it loses all its energy and vanishes eventually. Typically, a black hole formed in a particle collision would have nonzero angular momentum determined by the impact parameter. At particle level, it is also very likely for the black hole to carry gauge numbers of the initial parton pairs, which might include both electromagnetic charges and color charges. Moreover, since the formation occurs in a violent process, the initial event horizon could be very asymmetric, and hence the black hole could possess extra hair corresponding to the multi-pole moments of the distribution of gauge charges and energy momentum within the configuration [30]. Therefore, a black hole formed in this way is believed by many to go through a four-stage process, including balding, spindown, Hawking radiation and final explosion.

After balding and spindown the black hole can become symmetric by getting rid of various multi-pole moments and its angular momentum, through classical gauge radiation to gauge fields on the brane where the standard model fields resides, and through gravitational radiation. The frequency of the radiation, ω , also from a classic point of view, is obviously determined by the frequency of the oscillation of the multi-pole moments. Naturally, since the typical length scale of those multi-pole moments is set by the Schwarzschild radius of the horizon, r_s , the duration of the balding process should be $\sim r_s^{-1}$. On the other hand, the lifetime of an ordinary black hole is $\sim M_{BH}$. However, for a Planckian QBH, the above two scales are very close, and it suggests we should not treat balding as a separate stage from the rest of the decay. We also consider the spin-down process as inseparable from the other stages because it happens almost instantaneously near the threshold. It is calculated in [31] that for $n = 0, 1$ there are upper limits to the angular momentum of the black hole produced in a grazing collision,

$$J \leq J_*(M_{BH}) = \begin{cases} (1/2) r_s M_{BH} & n = 0 \\ (2/3) r_s M_{BH} & n = 1 \end{cases} . \quad (3.28)$$

For $M_D < M_{BH} < 3M_D$, the angular momentum is at most of order 1. We assume these results can be generalized to $n \geq 2$, and hence we decide not to treat the spin-down process separately, either.

During the following Hawking radiation and the final explosion as the black hole mass has diminished down to the Planck scale, it is possible black hole will radiate to both the brane fields and the modes in extra dimensions, which people call ‘‘bulk’’ modes. Energy dissipated into the extra dimensions will of course be identified as missing energy. We show this process in Fig. 3.3. It would have severely undermined the prospect of observing the decay products of black holes if the black holes were to lose too much energy to the bulk. In fact, [32] argues the black hole radiates mainly on the brane. We will simply give a qualitative analysis here [33].

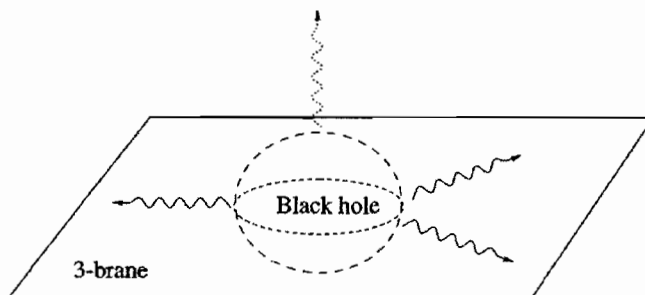


FIGURE 3.3: An extra-dimensional black hole bound on a 3D brane emits Hawking radiation to both brane fields and bulk modes. This figure is provided by [30].

As indicated in Eq. (3.24), the Hawking temperature is proportional to the inverse Schwarzschild radius of the underlying black hole,

$$T_{BH} = \frac{1+n}{4\pi r_s}. \quad (3.29)$$

This temperature determines a variety of properties of the black hole decay, including the typical wavelength,

$$\lambda = \frac{2\pi}{T_{BH}} \gg r_s. \quad (3.30)$$

The fact that the wavelength greatly exceeds the size of the horizon implies we should treat the decaying black hole as a point radiator, and therefore the emission is mostly in s waves. In other words, the radiation is only sensitive to the radial coordinate, and the extra angular modes available in the extra dimensions are not important. As a result, the black hole will decay equally to a particle on the brane and in the bulk.

Since there are many more modes on the brane than those in the bulk, the Hawking radiation is believed to be dominated by Standard Model fields, and we will neglect the bulk modes from our following discussions.

Summarizing the last few paragraphs, it is unlikely for a black hole near the Planck scale to shed its multi-pole moments, gauge charge, angular momentum through well-separated processes. The radiation into the extra dimensions from such a black hole also seems to be irrelevant. As a result, we think it is plausible to think of the decay of a QBH to be instantaneous, and its quantum numbers will simply be preserved by a two-body final states which will dominate the phase space of the decay products. The two particles in the final states are confined on the brane and included in the Standard Model, and the Compton wavelength of each particle will be of order the size of the QBH.

3.4 Quantum Black Holes and Cross Sections

3.4.1 What Is a Quantum Black Hole

To state our assumptions more clearly, we first characterize our QBHs by three quantities: mass, spin and gauge charges. Most importantly, QBHs can have a $SU(3)$ charge, or equivalently, a color charge, in contrast to the traditional treatment of black holes where only electromagnetic charges are considered. This characterization does not contradict the confinement since apparently the hadronization only happens at a much longer scale (Λ_{QCD}) than the QBH formation and decay. The central assumptions of our study are listed as below in a more formal way:

- (I) Processes involving QBHs conserve QCD and $U(1)$ charges since local gauge symmetries are not violated by gravity.
- (II) QBH coupling to both on-shell long wavelength and highly off-shell perturbative modes of the Standard Model is suppressed.
- (III) QBHs decay democratically to all Standard Model fields as long as assumption I and II are both satisfied.

We choose to hold assumption (I) because it is hard to imagine local gauge charges would be modified by the formation and decay of QBHs. We think the most reasonable scenario is that the total flux through a large Gaussian 3-sphere surrounding the spatial region where QBH formation and decay occurs should remain constant by causality. This implies the conservation of both QCD charges and $U(1)$ charges. It would be extremely odd if gravity only chooses to violate only one local gauge symmetry while leaving the other intact. This is the key assumption of our project, because it leads to the statement that the two-body final states of the QBH decay would preserve not only the electromagnetic charge of the black hole, or that of the initial parton pair, but it would also preserve the QCD charge of the initial parton pair, which enables us to calculate the branching ratios of individual channels of the decay. In the discussions below, we shall classify QBHs according to the irreducible representations of $SU(3)_c$ and $U(1)_{em}$, and label QBH states as QBH_c^q . Assumption (II) is necessary so that the precision measurements, or possibly proton decay would not force the quantum gravity scale to be much larger than the TeV scale.

It is worth mentioning that our results for the decay of QBHs also depend on whether we require QBH processes correspond to Lorentz invariant local effective field theory operators. We are not aware of any argument in favor of this which is as robust as that for the conservation of QCD charge. However, even if Lorentz invariance is indeed violated by quantum gravity in QBH processes, we can still employ assumption (II) to avoid any contamination from those effects in low energy physics near 1 TeV. We will come back to this with more details later.

3.4.2 Inclusive Cross Sections

In order to get quantitative results for we shall assume that QBH production cross sections can be extrapolated from the cross sections obtained for semi-classical black holes. We rewrite Eq. (3.18) by putting in the parameter $x_{\min} \equiv M_{\min\text{BH}}/M_D$,

$$\begin{aligned} \sigma_{pp}(s, x_{\min}, n, M_D) &= \int_0^1 2zdz \int_{\frac{x_{\min} M_D^2}{y^2 s}}^1 du \int_u^1 \frac{dv}{v} F(n) \cdot \\ &\cdot \pi r_s^2(us, n, M_D) \sum_{a,b} f_a(u/v, Q) f_b(v, Q) . \end{aligned} \quad (3.31)$$

Originally, the input for x_{\min} , as we illustrated earlier, is around 3 or 4 so that one can derive numerical results for cross sections of the production of semi-classical black holes. In our case, x_{\min} is chosen to be only 1 in order to calculate the production rates of QBHs which have limited entropy and mostly decay to only two particles in the final states. The construction for black hole production from high-energy collisions by Eardley and Giddings in [34] is held to be true for a QBH process as well in our calculation. To complete numerical analysis we use CTEQ5 PDFs and leave it to the users of our numerical program to decide whether to let the momentum transfer Q to be $\sim M_D$ or r_s^{-1} . We have also fitted the functions y_z for different numbers of compactified dimensions to the curves given by Nambu and Yoshino in [25]. For comparison we will calculate cross sections of semi-classical black hole production as well by setting $x_{\min} = 3$, and confirm our previous assumption that most of the c.m. energy will be lost through Initial-state Radiation and gravitational waves so that QBHs will dominate beyond the extra-dimensional Planck scale at the LHC.

3.4.3 Conservation of Gauge Charges

Finally we are ready to discuss the conservation of gauge charges in QBH processes. As mentioned earlier, QBHs can form representations of the $SU(3)_c$ group and carry a QED charge at the same time. We denote the process of two partons p_i, p_j forming a QBH in the c representation of the $SU(3)$ group of electric charge q as

$$p_i + p_j \rightarrow \text{QBH}_c^q . \quad (3.32)$$

In quantum chromodynamics, quarks resides in $\mathbf{3}$, the fundamental representation of $SU(3)$, which is simply named by the dimension of this irreducible representation. This same rule of notation will apply to any other irreducible representation as well. Anti-quarks are described by the conjugate representation of the fundamental representation, $\bar{\mathbf{3}}$, while gauge transformation property of gluons resemble the irreducible representation known as the *adjoint representation*, $\mathbf{8}$. The color representation of QBHs should be equivalent to the direct product of the color representations of the initial parton pair. For example, a quark and an anti-quark form a representation of $\mathbf{3} \otimes \bar{\mathbf{3}}$, the direct product of $\mathbf{3}$ and $\bar{\mathbf{3}}$. In group theory, this representation that results from a direct product can be decomposed to two separate irreducible representations:

$$\mathbf{3} \otimes \bar{\mathbf{3}} = \mathbf{1} \oplus \mathbf{8} , \quad (3.33)$$

where $\mathbf{1}$ denotes a color singlet that transforms to itself under the $SU(3)$ group. In colliders, Eq. (3.33) corresponds to the transition of a quark and an anti-quark forming either a singlet QBH or an octet QBH which transforms under $SU(3)$ in the adjoint representation. There is no a priori knowledge that can help us determine the exact likelihood of producing QBHs in different irreducible representations, but it seems to us the most natural assumption we can make about this is:

- (IV) The probability to create a QBH within an irreducible representation during a given transition process is proportional to the dimension of the irreducible representation.

Consequently, the probability to find a color-singlet QBH produced by a quark-anti-quark pair is $1/9$, while the probability to find a color-octet QBH in the same reaction is $8/9$. For completeness, we list all the other direct products of representations and their decompositions that are relevant to parton pairs forming QBHs^g as below:

$$\mathbf{3} \otimes \mathbf{3} = \mathbf{6} \oplus \bar{\mathbf{3}} \quad (3.34)$$

$$\mathbf{3} \otimes \mathbf{8} = \mathbf{3} \oplus \bar{\mathbf{6}} \oplus \mathbf{15} \quad (3.35)$$

$$\mathbf{8} \otimes \mathbf{8} = \mathbf{1}_S \oplus \mathbf{8}_S \oplus \mathbf{8}_A \oplus \mathbf{10} \oplus \bar{\mathbf{10}}_A \oplus \mathbf{27}_S, \quad (3.36)$$

where the lower index “A” means “anti-symmetric” and “S” means “symmetric”. An tensor object within a representation can be either symmetric or anti-symmetric under the exchange of two of the tensor indices. On the other hand, the decay product of a QBH should inherit the color charge of the same QBH according to our assumption (I). We shall use a specific example to illustrate this color charge conservation. Consider a quantum black hole with electric charge $-2/3$ and color charge $\bar{\mathbf{3}}$. A QBH will decay to a final state consisting of two standard model particles as pointed out earlier, which by themselves could be color-singlets (leptons, SU(2) gauge bosons, Higgs), color-triplets (quarks and anti-quarks) or color-octets (gluons). The direct products of the color representations of those two particles must have a non-zero overlap with the color representation of the mother black hole, otherwise the transition channel would be forbidden by assumption (I). As a result, possible final states could be made up of two down-type quarks, one anti-up-quark plus a neutrino, and all other particle combinations that could yield a color charge of “ $\bar{\mathbf{3}}$ ” and an electric charge of $-2/3$. Each individual degrees of freedom will have the same branching ratio since we consider a QBH to be an extrapolation of a semi-classical black hole and thus decay democratically to standard model fields. Other constraints could apply if a local field theory description is relevant and if Lorentz invariance is held to be true at the QBH scale. More decay channels and corresponding branching ratios will be covered later.

There are some other issues that remain to be clarified. In a local field theory description that respects Lorentz invariance, we assume a transition is probable as long as a local field operator for that same reaction can be written down. This

treatment is also justified by the observation that the decay of a Planckian black hole should be dominated by S waves, since black holes near the threshold are much smaller in size compared to the typical wavelength of the radiation and thus act like point radiators. Furthermore, we adopt this treatment because we believe the angular momentum of a QBH that comes from a nonzero impact parameter is extremely small and can be neglected from numerical considerations, which is supported by the calculation of [31]. The angular momentum conservation can therefore be taken care of by constraining the local field operator to preserve Lorentz invariance. However, more channels will be open if we relax the requirement on Lorentz invariance, and one would have more striking signatures of QBHs in that way.

Another problem is related to the numerical integrations present in Eq. (3.31). The integrand changes drastically within the domain of integration due to the effects of PDFs. As a result, ordinary Monte Carlo integration might not be appropriate for our purpose which would converge very slowly in this case. Instead, a integration package developed by M. Martinez, J. Illana, J. Bossert, and A. Vicini is used to evaluate the integral in Eq. (3.31) and many other integrals that will be introduced later. The algorithm this package makes use of is known as *VEGAS*. It achieves better convergence over ordinary Monte Carlo integration through *importance sampling* and *stratified sampling*. *VEGAS* starts the integration at interest with a uniform stratified distribution, and evolves the stratified distribution adaptively by histogramming the integrand in order to achieve a better resemblance of the shape of the integrand. A separable probability function is used as the stratified distribution function when dealing with multi-dimensional integrals,

$$g(x_1, x_2, x_3, \dots) = g_1(x_1) g_2(x_2) g_3(x_3) \dots, \quad (3.37)$$

such that the number of histogram bins will only increase as Kd instead of K^d if there are K bins for each coordinate and d dimensions in total.

3.4.4 Individual Decay Channels

We have assumed that QBH processes will conserve both color charge and electric charge, and this is one of the governing rules that determine the decay process of QBHs. An example is already given as we mention the possible decay products of $\text{QBH}_{\frac{2}{3}}^{-2/3}$. QBHs with other gauge charges will be discussed below under different assumptions about Lorentz invariance.

Let us begin with a color-singlet QBH that is also neutral under $U(1)_{\text{em}}$, or, QBH_1^0 . In our setup, such a black hole can decay to any combinations of Higgs bosons, leptons, quarks as well as gauge bosons and gravitons, e.g.

$$\begin{aligned}
 \text{QBH}_1^0 &\rightarrow e^+ + e^- , \\
 \text{QBH}_1^0 &\rightarrow e^+ + \mu^- , \\
 \text{QBH}_1^0 &\rightarrow q_i + \bar{q}_i ,
 \end{aligned}
 \tag{3.38}$$

etc., as long as we do not impose Lorentz invariance and the global final state is neutral under $SU(3)$ and $U(1)_{\text{em}}$. The number of degrees of freedom of a quark-anti-quark pair a QBH_1^0 can decay to is three times that of a lepton pair, since there are three different colors. Similarly, the number of degrees of freedom of a pair of Z^0 bosons is $\frac{3}{2} \times \frac{3}{2} = 9/4$ times that of a lepton pair, since there are 3 degrees of freedom in spin space for a massive gauge boson while only 2 for a fermion. We follow these rules when developing the branching ratios for individual channels based on the particle level cross sections of a certain type of QBH, which in this case is just QBH_1^0 . The integral that need to be evaluated is simply Eq. (3.31) with the sum over parton pairs modified in order to account for the right combination of gauge charges. For a color-singlet black hole with zero electric charge, we select to sum over only neutral quark-anti-quark pairs, and then multiply the resulting integral by a factor of $1/9$, according to the color representation argument we give above. Apparently,

most of the time QBH_1^0 would decay into two-jet events due to the large number of color degrees of freedom.

A color-octet black hole which is electromagnetically neutral, QBH_8^0 , can decay into a pair of a quark and an anti-quark with opposite electric charge, or a gluon and a neutral particle, e.g., a graviton or a Z-boson. More details on the branching ratios depend on how many independent channels there are. The availability of any specific channel can be affected by whether one wants to enforce a Lorentz invariant local field theory description of the QBH reaction. If we do assume this particular description of QBH processes, then transitions such as

$$q_i + g \rightarrow \text{QBH}_c^q \rightarrow \bar{q}_k + \bar{q}_j \quad (3.39)$$

would not be allowed, where q_i are quarks and g is gluon, because there is no way to write down a Lorentz invariant local field operator linking three fermions and a spin-1 gauge boson.

An electrically charged color-triplet black hole, QBH_3^q , can decay to either a pair of a charge q quark and a gluon, or a pair of anti-quarks, depending on the initial configuration of the parton pair that forms the same QBH. However, those two types of events are both characterized by two back-to-back jets in the final state, and thus are difficult to be separated from the Standard Model background. Other similar modes may include quark + photon, quark + Z-boson, anti-quark + anti-neutrino, etc. The decay products of black holes in higher representations can also be determined in this way: QBH_{10}^0 , QBH_{10}^0 , QBH_{27}^0 , QBH_6^q , QBH_{15}^q , QBH_6^q and QBH_3^q .

In this project, we study the QBH cross sections in three different scenarios that can give rise to the production of QBHs near the 1 TeV scale. We will not review *ADD* and *RS* here since both of them have been well known and explored. We will only briefly discuss a new four-dimensional model here that is suggested by Xavier Calmet, Stephen Hsu and David Reeb [35]. In an ordinary extra-dimensional model, the Planck scale is lowered to the TeV scale because the large volume of extra

TABLE 3.1: Cross-sections for the production of quantum black holes and semiclassical (sc) black holes from a pair of protons. The missing energy (m.e.) component is also indicated. We take the reduced Planck mass to be 1 TeV and thus restrict our considerations to ADD with $n \geq 5$ since lower dimensional models with $M_D = 1$ TeV are ruled out by astrophysical data.

models	$\sigma(\text{any QBH})$ in fb	$\sigma(\text{sc-BHs})$ in fb	$\sigma(\text{m.e.})$ in fb
RS	1.9×10^6	151	\sim none
ADD $n = 5$	9.5×10^6	3.1×10^4	some
ADD $n = 6$	1.0×10^7	3.2×10^4	some
ADD $n = 7$	1.1×10^7	2.9×10^4	some
CHR	1×10^5	5×10^3	744

dimensions can dilute the gravitational field and thus make gravitational field look weaker than the other fundamental forces in the usual four-dimensional spacetime. However, in this new four-dimensional model, the authors point out the Planck scale can also be lowered to the TeV range, if a large hidden sector is allowed with about 10^{32} scalar particles interacting with Standard Model particles only gravitationally. From the perspective of introducing vast amount of new degrees of freedom in order to lower the fundamental scale of gravity, this new model, which we will refer to as *CHR*, is no different from the traditional extra-dimensional models. Through coupling to the graviton, the scalar particles in this hidden sector can radically change the renormalization of the gravity and therefore the gravitational field can become strong at renormalization scale μ_* , where $M_P(\mu_*) = \mu_*$ [36]. For 10^{32} new particles, $\mu_* \sim 1$ TeV.

3.4.5 Cross Sections

We have calculated the inclusive production rate of QBHs at the LHC, for all three different models mentioned above. The results are displayed in Table. 3.1. As expected, the production is dominated by quantum black holes over semi-classical black holes by several order of magnitude. We assume the semi-classical black holes

start to form at $x_{\min} = 3$ in *ADD* and *CHR*, while those black hole will not be created until raising x_{\min} to 5 in the *RS* model. We have argued earlier that quantum black holes emit mainly on the brane because they act as point radiators due to the small size of the horizons, and here this is held to be true for both *ADD* and *RS* so that we would not lose much energy to invisible sectors. However, QBHs in the *CHR* model will emit a non-negligible amount of energy invisibly because of the large hidden sector that interacts with gravitons.

As we see, due to the conservation of gauge charges and the large number of color degrees of freedom, a pair of initial partons will most likely produce two hard jets in the final state via an intermediate quantum black hole. Two jet events from QBH radiation are difficult to be identified since there would be significant Standard Model background, although one can examine the angular distribution of the di-jet final states carefully and tell the difference between events with and without important gravitational effects. However, it is also very helpful to identify some individual transition channels through the assumption of color charge conservation, which have relatively much less Standard Model background and thus can be practically used to discover QBHs. These signatures can be, for example, a pair of lepton and anti-lepton of another flavor:

$$\text{proton} + \text{proton} \rightarrow \text{QBH}_1^0 \rightarrow e^- + \mu^+, \quad (3.40)$$

as we have already shown before. If we allow the violation of baryon and lepton number conservation, one can also have the transition of $\text{QBH} \rightarrow \text{lepton} + \text{jet}$ available. One example is:

$$\text{proton} + \text{proton} \rightarrow \text{QBH}_3^{-2/3} \rightarrow l^- + \bar{d}, \quad (3.41)$$

where l^- could be any charged lepton and \bar{d} could be the anti-particle of any down-type quark. This reaction can be described by a Lorentz invariant local field operator $qqq\bar{l}$ [37]. Similarly, there could be an anti-lepton in the final state and

thus the corresponding Lorentz invariant operator is $qqql$ [37]. The above two types of operators do not appear in the Standard Model, where operators are further constrained by chirality and $SU(2)$ invariance after leptons and quarks are introduced. However, we do allow such transitions in QBH processes since we only want to enforce $U(1)_{em}$ and color charge conservation. Furthermore, lepton + jet could potentially be a better discovering channel for QBHs than the di-lepton ones since there are more color degrees of freedom with little Standard Model background because of its high p_T . On the other hand, the magnitude of cross sections of processes such as

$$\text{proton} + \text{proton} \rightarrow \text{QBH}_{\frac{1}{3}}^{1/3} \rightarrow \gamma + \bar{d} \quad (3.42)$$

heavily depends on whether a Lorentz invariant local field operator description is appropriate. Should the cross sections of those processes be indeed measured at the LHC, one would have more clues about the spacetime near the Planck scale.

According to assumption (III), QBHs couples equally to all degrees of freedom, regardless of the flavors of fields. It is also plausible to assume the decay products are all massless since they are all highly boosted, and therefore we expect the following to be true:

$$\begin{aligned} \sigma(p + p \rightarrow \text{QBH} \rightarrow e + \text{jet}) &= \sigma(p + p \rightarrow \text{QBH} \rightarrow \mu + \text{jet}) \\ &= \sigma(p + p \rightarrow \text{QBH} \rightarrow \tau + \text{jet}) . \end{aligned} \quad (3.43)$$

Combined with our earlier arguments on both color and spin degrees of freedom, we can calculate the rates of all interesting signatures using a program that performs the integrations numerically. Results for these cross sections are listed in Table 3.2. The final-state lepton can belong to any of the three generations, and can even be a neutrino, in which case the signature would be missing energy with a high p_T jet. Note that there could still be gauge bosons and the Higgs boson in the final state, e.g., a QBH can decay into a Z and a jet or a Higgs boson and a jet. The transitions

TABLE 3.2: Possible final states in quantum black hole decay for the models CHR, RS and ADD. Gravity is democratic; one thus expects the same cross-sections for final states with any charged lepton combination. Note that if the neutrino is a Majorana particle the cross-section $\sigma(\text{p+p} \rightarrow \text{QBH}_3^{-2/3} \rightarrow \nu_i + \bar{u})$ is nine times larger since one cannot differentiate ν from $\bar{\nu}$. If the neutrino is a Dirac type particle, then one has $\sigma(\text{p+p} \rightarrow \text{QBH}_3^{-2/3} \rightarrow \nu_i + \bar{u}) = \sigma(\text{p+p} \rightarrow \text{QBH}_3^{-2/3} \rightarrow \bar{\nu}_i + \bar{u})$. Note that we have summed over the polarization of the photon for the cross-sections $\sigma(\text{p+p} \rightarrow \gamma + \text{jet})$. The cross-section $\sigma(\text{p+p} \rightarrow \text{Z} + \text{jet}) = \sigma(\text{p+p} \rightarrow \gamma + \text{jet})$.

rates in fb	CHR	RS	ADD $n = 6$	ADD $n = 7$
$\sigma(\text{p+p} \rightarrow \text{QBH}_3^{4/3} \rightarrow l^+ + \bar{d})$	346	5.3×10^3	3.5×10^4	3.7×10^4
$\sigma(\text{p+p} \rightarrow \text{QBH}_3^{-2/3} \rightarrow l^- + \bar{d})$	27	422	2.5×10^3	2.7×10^3
$\sigma(\text{p+p} \rightarrow \text{QBH}_3^{1/3} \rightarrow \nu_i + \bar{d})$	167	1.5×10^3	1.7×10^4	4.2×10^4
$\sigma(\text{p+p} \rightarrow \text{QBH}_3^{-2/3} \rightarrow \nu_i + \bar{u})$	27	422	2.5×10^3	2.7×10^3
$\sigma(\text{p+p} \rightarrow \text{QBH}_3^{-2/3} \rightarrow \gamma + \bar{u})$	54	844	5×10^3	5.4×10^3
$\sigma(\text{p+p} \rightarrow \text{QBH}_3^{1/3} \rightarrow \gamma + \bar{d})$	334	3×10^3	3.4×10^4	8.4×10^4
$\sigma(\text{p+p} \rightarrow \text{QBH}_1^0 \rightarrow e^+ \mu^-)$	0	161	8.5×10^2	8.9×10^2

can exist even if Lorentz invariance is preserved in a local field theory description, as long as the initial parton pair is made up of a quark and a gluon. It is a less outstanding type of signature only because their cross sections are relatively small compared to those with a lepton and a jet, due to the details of PDFs.

3.5 Conclusions

We have shown that while semi-classical black holes are unlikely to be produced at the LHC, quantum black holes which only decay to a few, most likely two, particles can lead to extraordinarily large cross sections, due to the lack of small couplings. Striking signatures include two leptons of different flavors and with opposite charges, one hard lepton plus one hard jet with high p_T . From the theoretical point of view we have also shown with very conservative assumptions about the dynamics of quantum black holes one can still make predictions for their decay modes. The calculated

branching ratios for such channels are sufficiently big and numerous interesting events can be generated at the LHC, given our four central assumptions.

CHAPTER IV

DIRECT NUMERICAL INTEGRATION

4.1 Introduction

At the LHC era, the Standard Model cross sections of many transitions, where 2 particles scatter to produce n other particles, are important for the discovery of new physics beyond the Standard Model itself. At the lowest order in perturbation theory, the calculation of such cross sections is straightforward. One can simply multiply the squared tree-level matrix elements by the measurement function for each choice of final-state momentum $\{p_1, p_2, \dots, p_n\}$, and then integrate over these momentum either numerically or analytically without too much trouble, since there are no singularities present.

However, it is not trivial to extend the same calculation to the next-to-leading order. A matrix element with one virtual loop needs to be multiplied with both the complex conjugate of the tree-level matrix element and the measurement function, plus the complex conjugate of this product. To calculate the corresponding cross section, one can typically choose to compute the loop integral first within the loop diagram, and use the result as a whole to be the integrand of the integration over the final state momentum. It is unavoidable that people would run into infrared and ultraviolet divergences during the loop integration, and that is exactly what makes such NLO evaluations difficult. Necessary subtraction schemes would have to be adopted to control the divergences. People have been devising algorithms to decompose those loop integrals with multiple external legs using a series of the so-

called “master integrals”, for which values are known. There has been rapid progress in this approach recently [38][39][40].

Another methodology is to perform the loop integral numerically. The idea is to integrate the loop momenta l of the loop diagram with the group of external momentum $\{p_1, p_2, \dots, p_n\}$ altogether at the same time when evaluating the product of the amplitude of the virtual loop diagram and that of the complex conjugate of the tree-level diagram. This means one sample point for the numerical integration in a Monte Carlo style algorithm would be simply $\{l; p_1, p_2, \dots, p_n\}$. However, the loop amplitude still contains factors such as $1/((l - Q_i)^2 + i\epsilon)$, which gives rise to singularities. The numerical approach can set up schemes where some of the above singularities can be avoided through deforming the integration contour away from the singular point into the complex l space. The essential problem is how to specify the contour deformation in a systematic way when there are multiple singular factors present in the integrand. One choice is to use the Feynman parameters, x , to rewrite the integrand so that the loop integral can be integrated over l and x or even only x . Then the mission becomes deforming the contour of x in the complex plane. It is still categorized as the numerical Monte Carlo method because every set of Feynman parameters x (there could be more than one Feynman parameter in a single loop integral) will be sampled with a choice of the external momentum.

In [41], an example is given for using Feynman parameters to integrate the loop momenta numerically. The process studied is the scattering of

$$\gamma + \gamma \rightarrow (N - 2) \gamma \tag{4.1}$$

through a massless electron loop. The virtual loop diagram with 6 external photons is shown in Fig.4.1. According to Feynman rules, the matrix element that corresponds to this diagram is

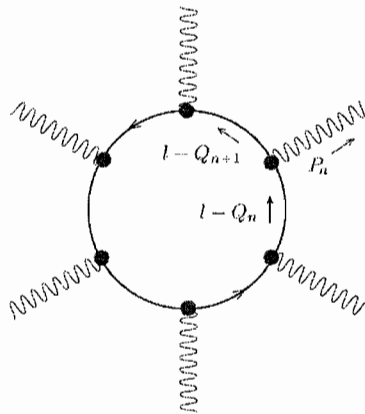


FIGURE 4.1: Feynman diagram for the N-photon amplitude. This figure is provided by [42].

$$\mathcal{M} = \int \frac{d^4 l}{(2\pi)^4} (ie)^N N(l) \prod_{j=1}^N \frac{i}{(l - Q_j)^2 + i0}, \quad (4.2)$$

where $N(l)$ is the numerator function, and the small imaginary part in the denominators $i0$ specifies the prescription for contour deformation in the complex plane, which we will come back to later. Although a QCD diagram with a quark loop would be of more practical interest, but nevertheless this N-photon amplitude is a good starting point for studying the numerical Monte Carlo algorithm itself. The reason is that the infrared singularities of this amplitude are not as serious as what they may look like, and all of them are integrable. Therefore infrared subtractions are not necessary here. Once having this simplification, one can study the contour deformation without worrying about the subtraction scheme at the same time. By simply power counting, the loop integral is also finite when the number of external photons is greater than 4.

Let us give a simple proof to illustrate the severity of the pinch singularities in this Feynman graph. These singularities can not be deviated from through simply deforming the integral contour into the complex plane. At first glance extra measures need to be taken in order to solve this problem, but we will now show that it is not true. As displayed in Fig. 4.1, the loop momentum carried by electron line n is $l - Q_n$, where Q_n is fixed and we integrate over l . The momentum for external photon n is of course

$$P_n = Q_{n+1} - Q_n \quad (4.3)$$

once we define the momentum that flows outward to be positive. Since we eventually will calculate the cross sections of 2 photons scattering to $N - 2$ photons, it is appropriate to consider the case where all N external photons are on shell and $P_n^2 = 0$ for all possible choices of n . Apparently, the propagators of electron loop momentum provide logarithmic divergences over the soft and collinear region. However, those divergences are cancelled and hence we are relieved from setting up a subtraction scheme to deal with the infrared singularities. For each electron line there is a factor $l - Q_n$ in the numerator, and it will vanish right at the soft singular point where $(l - Q_n)^2$ become zero. The soft singularities are removed thanks to this factor. In addition, when $(l - Q_n) \rightarrow xP_n$, it also happens that $(l - Q_{n+1}) \rightarrow -(1 - x)P_n$. It means the momentum of the external photon n becomes collinear or parallel with the two neighboring loop momenta. Since P_n is on shell, $(l - Q_n)^2$ also becomes zero close to the collinear domain. Singularities of this kind again cannot be avoided through contour deformation, which we will further discuss in more details. Fortunately, according to the Feynman rules, there is a factor

$$(l - Q_{n+1}) \not{\epsilon}_n (P_n) (l - Q_n)$$

for each vertex, where $\epsilon_n (P_n)$ is the polarization vector of the external photon n . In

the collinear limit when $(l - Q_n) \rightarrow xP$, we can use a little bit of the gamma matrix algebra and derive

$$-x(1-x)\not{P}_n\not{\ell}_n(P_n)\not{P}_{n+1} = -2x(1-x)\not{P}_n\epsilon_n(P_n)\cdot P_n. \quad (4.4)$$

We require $\epsilon_n(P_n)\cdot P_n = 0$ because photon as a massless gauge boson can only have transverse degrees of freedom and hence be transversely polarized. This automatically removes collinear divergences from our consideration.

Back to the Feynman parameter approach, Eq. (4.2) can be rewritten down as

$$\begin{aligned} \mathcal{M} = & -m_0^2 e^N \Gamma(N+1) \int \frac{d^4\ell}{(2\pi)^4} \frac{1}{(1+\ell\cdot\ell)^{N+1}} \\ & \times \int_C dx \left(\sum_{i=1}^N x_i \right)^{N-3} \frac{N(l(x,\ell))}{[\Lambda^2(x)]^{N-1}}, \end{aligned} \quad (4.5)$$

where ℓ is the spatially translated and Wick rotated loop momentum, and therefore $\ell\cdot\ell$ is in fact the Euclidean square of l . $\Lambda^2(x)$ is a quadratic function of the Feynman parameters, and C is the integration contour over which x 's are integrated.

Since all singularities left in Eq. (4.5) are integrable, it is in principle guaranteed the numerical integration will converge given enough sample points in a Monte Carlo style calculation. However, a numerical algorithm is only useful when it can reduce the statistical uncertainty to an acceptable degree with a practical number of sample points. Thus the contour C of the Feynman parameters are carefully chosen [41], instead of randomly picked, to stay away from singularities whenever it is possible. It turns out the maximum number of external photons, for which such a numerical calculation can give a sensible answer on an ordinary computer, is $N = 6$. The numerical integral introduced in Eq. (4.5) would fail to converge fast enough for $N > 6$. For several helicity configurations (of the external photons), there are analytical solutions, and the numerical results have been found to agree with the analytical results.

There are limitations to the Feynman parameter method. As the number of external photons increases, the power of the quadratic function $\Lambda(x)$ also goes up, and this can make the numerical convergence worse, although theoretically the integral will converge eventually. Moreover, if a calculation is encountered where the infrared subtraction is needed, people would not be able to construct any subtraction scheme within the framework of the Feynman parameter approach. In contrast, it is already known [43] how to construct subtractions directly in the momentum space. It would be therefore very nice if one can specify a way to perform the numerical integral directly in the momentum space, without the help of Feynman parameters.

The most difficult issue concerning a direct numerical integration would be the determination of the contour of the integral. The Feynman parameter is free of this problem because the singular denominator is the power of a quadratic function, $\Lambda(x)$, of the integration variables. It is very simple to find a contour that can be diverted away from all the roots of the quadratic equation $\Lambda(x) = 0$. However, as Eq. (4.2) shows, there are many different factors in the denominator in the direct approach, and the singularities are scattered out in a manner for which it is not trivial at all to find an appropriated deformed contour in the loop momentum space. It is thus the objective of this project to specify the contour deformation, and compare the numerical results with those derived by the Feynman parameter method and the analytical answer. The expectation is, as implied earlier, compared to the Feynman parameter method the direct numerical integration should be able to calculate virtual loop diagrams with more external photons. Even if it were only as good as the Feynman parameter method, we would still be glad to have an algorithm in which the infrared subtraction can be applied straightforwardly. The standard methodology where \mathcal{M} is evaluated as whole in terms of master integral might still be found to be superior to our new numerical algorithm, but nevertheless it is still worthwhile to invent new tools and methods which could turn out to be useful in some other contexts.

4.2 Contour Deformation

4.2.1 Generic Form

In Eq. (4.2), the integrand is singular on the surface of $(l - Q_j)^2$. It is a lightcone with its vertex at Q_j in the loop momentum space. People can avoid those singularities by deforming the loop momentum into the complex plane. The general technique is to add a small imaginary part to the original momentum, and thus the deformed momentum becomes a vector function of the original loop momentum:

$$\ell^\mu(l) = l^\mu + i\kappa^\mu(l) , \quad (4.6)$$

where κ^μ are all real, and they are the components of a 4-vector. After making this deformation, there will be a new imaginary term showing up in the denominators of electron propagators, and people will no longer run into singularities on the surface of the lightcones as long as the imaginary parts do not vanish. In addition, the value of the deformed integral will remain the same as what the original value is if the following criterions are satisfied:

- (I) The deformation starts in the direction specified by the “ $+i0$ ” prescription, meaning the imaginary part should be positive when close to the original singularities;
- (II) The contour should not encounter any other singularities when it is deformed away from the original singularities.

A simple proof of the above argument can be found in [44]. If we convert the integration variables of the deformed integral from ℓ back to l , we would have

$$\mathcal{M} = \int \frac{d^4l}{(2\pi)^4} (-ie)^N \det(\partial\ell/\partial l) N(\ell(l)) \prod_{j=1}^N \frac{i}{(\ell - Q_j)^2} , \quad (4.7)$$

for a virtual loop diagram with N photons.

Since the contour we study is deformed in a vector space, we need to specify both the direction and the magnitude of the deformation. It would thus be helpful to rewrite the imaginary part as

$$\kappa^\mu(l) = \lambda(l) \kappa_0^\mu(l) , \quad (4.8)$$

and in this expression, $\lambda(l)$ is the real function of momentum that controls the size of the deformation at each point on the contour. The lower limit of this function is zero everywhere, and the upper limit λ_f shall be constrained by the second criteria for contour deformation mentioned earlier, that is, the deformation should be stopped before the contour hits any other new singularities. If using Eq. (4.8) to express the denominator for propagator j in Eq.(4.7), one would have

$$(l - Q_j + i\kappa(l))^2 = (l - Q_j)^2 - \lambda^2(l) \kappa_0^2(l) + 2i\lambda(l) (l - Q_j) \cdot \kappa_0(l) . \quad (4.9)$$

By construction, $\lambda(l) \rightarrow 0$ when one just starts the deformation, and the contour is very close to the original singularities. Geometrically speaking, it also means the integration variable l would be on the surface of one or more lightcones. Therefore, in order to retain the value of the original integral, one must have $\lambda(l) (l - Q_j) \cdot \kappa_0(l) > 0$ on the lightcones so that the $+i0$ prescription can be satisfied. Again, the geometric interpretation of this requirement is the 4-vector κ_0 must be pointing toward the interior of the lightcone. This can be easily proved by considering an arbitrary l on the cone where the condition $(l - Q_j)^2 = 0$ is automatically met. If the corresponding point $l + \lambda\kappa_0$ is indeed in the interior of the cone j , it would be a light-like point and have

$$(l + \lambda\kappa_0 - Q_j)^2 > 0 . \quad (4.10)$$

One can make use of the fact $(l - Q_j)^2 = 0$ and expand the left hand side of Eq. (4.10) to the first order in λ assuming λ is a small parameter. It would come out that

$\lambda(l - Q_i) \cdot \kappa_0 > 0$. This proof also works the other way around. More over, it can be shown in the same way that $(l - Q_j) \cdot \kappa_0 = 0$ means the vector κ_0 is tangent to the cone surface.

Ideally, one would want to move the contour away from singularities whenever it is possible. When there is only one cone j involved, that means, according to the discussion above, we should let $\kappa_0 \cdot (l - Q_j) > 0$. However, it is only true when l is not on the vertex of that cone, otherwise it is impossible to deform if $l - Q_j = 0$. We call it a “pinch singularity” when the singularity cannot be avoided by making deformations. In this case, the soft singularity is pinched, but fortunately the analytical divergences can be removed by a corresponding numerator function as we already pointed out earlier. The numerical values of the integrand near soft singularities could still be large and undermine the numerical convergence of the whole integral. A special technique will be introduced later to resolve this issue by sampling more points near pinch singularities in a Monte Carlo style calculation.

Things are a little more complicated when momentum l is on more than one lightcones at the same time. With the help of the geometric interpretation of κ_0 that satisfies the $+i0$ prescription, however, we can still see what κ_0 should look like in the momentum space without a problem. One typical situation is when two cones intersect, how should we manage the contour right on the intersection? Suppose the vertex of one of the two cones is Q_i and the vertex of the other is Q_j . If $Q_j - Q_i$ is timelike, obviously the singularities on the intersection are not pinched, because we can easily specify a κ_0 that points to the common interior of both cones, e.g.,

$$\kappa_0 = -(l - Q_i) - (l - Q_j) . \quad (4.11)$$

Through simple vector summation, one would find κ_0 defined as such does point to the correct direction. We can of course prove the same argument by calculating $\kappa_0 \cdot (l - Q_i)$. Since $(l - Q_i)^2 = 0$, the κ_0 given in Eq. (4.11) can lead to

$$\kappa_0 \cdot (l - Q_i) = (Q_i - Q_j) \cdot (l - Q_j) , \quad (4.12)$$

and straightforwardly this dot product is positive because it is the product of one timelike vector and one lightlike vector both in the same direction in time. One can prove this same κ_0 also satisfies the same requirement for cone j , and hence confirm the claim that the contour is deformed in the right direction. If $Q_j - Q_i$ is instead a spacelike vector, a κ_0 can be easily found in a similar way as well.

If $Q_j - Q_i$ is lightlike, it means the two loop momentum, $l - Q_i$ and $l - Q_j$, are next to each other in the electron loop, and vector $K \equiv Q_j - Q_i$ must be equal to the momentum of the external photon between these two loop momentum up to a sign. Any l on the intersection of the two corresponding lightcones will make the loop momentum collinear with K , and we can parameterize $l - Q_i = xK$. If $x < 0$ or $x > 1$, the inside of one cone is inside the other cone, so apparently a κ_0 can be pointing to the interior of both cones when it points to the interior of the inner cone. However, as pointed earlier, collinear singularities exist when $0 < x < 1$, because the interior of one cone is always outside the other cone. It is thus impossible to deform the contour into the complex plane in the right direction. To satisfy the $+i0$ prescription, the only thing one can do is to choose $\kappa_0(x) = c(x)K$ on the intersection with $0 < x < 1$ so that neither $(l - Q_i) \cdot \kappa_0$ nor $(l - Q_j) \cdot \kappa_0$ is negative.

4.2.2 Geometric Configuration

One can have more specific discussion on the contour deformation with the help of Fig. 4.2, in which vertices of lightcones and external momenta are suitably visualized. This plot shows a coordinate system for the loop momentum l , as used in Eq. (4.7), and this coordinate system is carefully chosen so that the transverse components of incoming photons vanish. Soft singularities, $l = Q_i$, are shown as black dots in this sketch, where no contour deformations can be made. Lines joining those end points are the collinear singularities, $l = Q_i + x(Q_{i+1} - Q_i)$ where $0 < x < 1$.

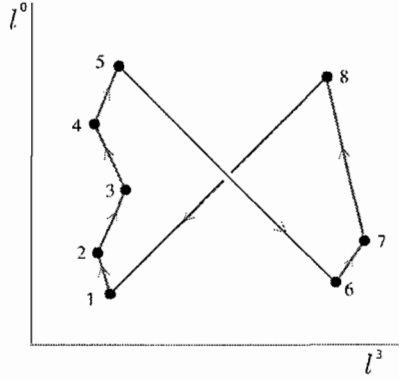


FIGURE 4.2: Kinematics for the N -photon amplitude, illustrated for $N=8$. Only the 0 and the 3 component of loop momentum l are shown in this plot. The coordinate system is chosen in such a way that the two incoming external photon have no transverse components. In addition, the points for $l = Q_i$ are marked, and the lines joining those points depict the external momentum $P = Q_i - Q_j$. This figure is provided by [42].

These singularities are also pinched, and κ_0 can only be chosen to be parallel to the external momentum $P_i = Q_{i+1} - Q_i$. We require $(l - Q_i) \cdot \kappa_0 > 0$ anywhere else on those lightcones with $l = Q_i$ as vertices. One would also find two of the external momenta, $P_A = Q_{A+1} - Q_A$ and $P_N = Q_1 - Q_N$, both have negative time components. In Fig. 4.2 we have $A = 5$ and $N = 8$. It is because they are incoming photons but we have defined the outgoing direction to be the positive direction for all external photons. For convenience, we shall define two positive momenta, $P = -P_A$ and $\bar{P} = -P_N$, for later use.

For the purpose of specifying κ_0 for the entire space of loop momentum l , one needs to have a more detailed analysis of the relations between any two vertices. It will soon prove useful to systematically study where and how different lightcones intersect. In Fig. 4.3, not only the two types pinch singularities are shown, but the projection of every lightcone on the 0-3 plane is also indicated to make our investigation easier. For lightcone $(l - Q_i)^2 = 0$, its projection is the region between the two dashed lines

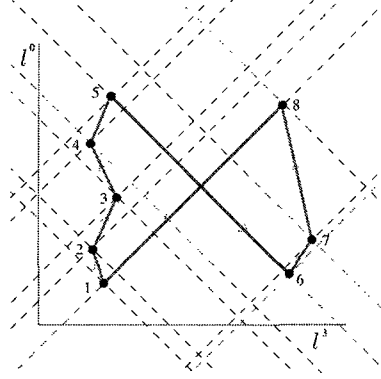


FIGURE 4.3: Kinematics for the N -photon amplitude, illustrated for $A = 5$ and $N = 8$. Lightcones $(l - Q_i)^2 = 0$ are also indicated. This figure is provided by [42].

that run through $l = Q_i$. Furthermore, the space has been divided into four shaded regions, in which, as we will see, κ_0 has different forms. Next we will discuss the geometric relations between lightcones in more detail, which will help us determine the form of κ_0 more definitely.

Let us study the left region first. The vertices of cones in this region are $\{Q_1, Q_2, \dots, Q_A\}$. For $1 \leq i < A$, the forward lightcone from Q_i is tangent to the backward lightcone from Q_{i+1} along the line between Q_i and Q_{i+1} , and intersects the backward lightcone from Q_j for $i + 1 < j \leq A$. The forward lightcone from Q_i is also tangent to the forward lightcone from Q_{i+1} , and the forward lightcones from Q_j for $i + 1 < j \leq A$ are all nested inside the forward lightcone from Q_i . The relations of the backward lightcone from $Q_{i'}$ with $1 < i' \leq A$ with other lightcones in the left region are similar to those of the forward lightcone from the same vertex $Q_{i'}$. Obviously, one can derive the same type of geometric relations between lightcones in the right region, with vertices of the cones from Q_{A+1} to Q_N .

If one looks at the relations between two lightcones, one from the left and one from the right region, the forward lightcones from any vertex in the left region do

not intersect with the backward lightcones from any vertex in the right region. The only exception is that the forward lightcone from Q_1 is tangent to the backward cone from Q_N along the line between Q_1 and Q_N . Vice versa, the forward cones from any vertex in the right region will not intersect with the backward lightcones from any vertex in the left region, with the only exception of the forward cone from Q_{A+1} being tangent to the backward cone from Q_A along the line from Q_A to Q_{A+1} .

There are no lightcone vertices at all either in the top region or the bottom region. However, in the top region, the forward cones from any vertex in the left region will intersect the forward cones from every vertex in the right region. Once again, the exception is the forward cone from Q_1 in the left region is tangent to the forward cone from Q_N . In the same top region, the forward cones from any vertex in the right region intersect the forward cones from every vertex in the left region, with the exception that the forward cone from Q_{A+1} is in fact tangent to the forward cone from Q_A . For intersections in the bottom region, we can simply duplicate the above analysis.

The picture of the lightcone configurations look very different when $A = 1$ or $A = N - 1$. Fortunately, the above argument still holds in these two special cases. To parameterize the four different regions, we choose a convenient set of coordinate system and define the coordinates to be

$$\begin{aligned} x &\equiv \frac{(l - Q_{A+1}) \cdot \bar{P}}{P \cdot \bar{P}}, \\ \bar{x} &\equiv \frac{(l - Q_1) \cdot P}{P \cdot \bar{P}}. \end{aligned} \tag{4.13}$$

Accordingly, the left region is $x < 0$ and $\bar{x} > 0$; the right region is $x > 0$ and $\bar{x} < 0$; the top region is $x > 0$ and $\bar{x} > 0$; the bottom region is $x < 0$ and $\bar{x} < 0$.

4.2.3 Double Parton Scattering

Until now we have seen collinear singularities and soft singularities, and have concluded that they are in fact all integrable singularities because the powers of zeros in the denominator could be lowered by corresponding numerator functions. There could be one true singularity in the numerical integration, called *double parton scattering singularity*, and it appears only if the line from Q_1 to Q_N intersects the line from Q_A to Q_{A+1} . A pinch singularity will sit right at such an intersection. Even if the external momentum configuration does not exactly satisfy the above condition, the two lines may still be close to intersecting, and the nearby region would cause trouble to the numerical convergence of the integral.

In a real reaction where two photons scatter to produce more photons, the double parton scattering will happen when the situation illustrated in Fig. 4.4 is true. Generally, incoming photon N could split into a pair of off-shell electron and positron, while the other incoming particle, photon A , could also split into a pair of off-shell electron and positron. The electron from photon N could annihilate with the positron from photon A and produce two or more external photons, and the positron from photon N could also interact with the electron from photon A and produce two or more external photons. Note that the reference frame can always be boosted so that neither of the two incoming photons has transverse momentum. Furthermore, we can even choose a frame where the two incoming external photons are traveling on parallel trajectories in opposite directions. One special case, as shown in Fig. 4.4, is the head-on collision of the initial photon pair, in which there exists one loop momentum to make the splitting of photon N and the splitting of photon A both collinear, with the two pairs of electrons and positrons all on shell, because the impact parameter is now zero. Two collinear branchings at the same time could dramatically enhance the cross section of the head-on collision, and thus contribute to a real divergence of the integral. We can also easily prove that the double parton scattering singularity exists if the transverse component p_T of a subset (containing at least two photons) of

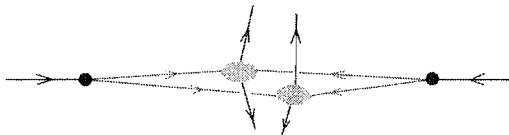


FIGURE 4.4: Physics picture of the double parton scattering. This figure is provided by [41].

the total external momentum vanishes in a frame where the incoming momentum are pointing in the $+z$ and $-z$ direction. The amplitude can numerically be very large when $p_T^2 \ll s$. The p_T test can be very useful in practical applications to crudely evaluate the severity of the double parton scattering problem.

More precisely, one can find out how close the line between Q_1 and Q_N is to the line between Q_A and Q_{A+1} . If the two lines do intersect, apparently we would have $x = 0$ and $\bar{x} = 0$ for the intersecting point according to our earlier definition of x and \bar{x} , and there is no other point on the above two lines whose values of x and \bar{x} can vanish at the same time. However, if the two line do not intersection, there would be exactly two points with a pair of zero x and \bar{x} . We can find out the positions of those two points by parameterizing the two lines using two additional parameters a_I and a_{II} , which are used to specify one arbitrary point on each of the line respectively. The point on the line from Q_1 to Q_N is called v_I , and

$$v_I = a_I Q_1 + (1 - a_I) Q_N . \quad (4.14)$$

It automatically has $\bar{x} = 0$. Using Eq. (4.13) and the definitions of P, \bar{P} , if the x value of point v_I also vanishes, we must have

$$\begin{aligned} 0 &= (v_I - Q_{A+1}) \cdot \bar{P} \\ &= (-a_I P + Q_N - Q_{A+1}) \cdot \bar{P}. \end{aligned} \quad (4.15)$$

One can therefore solve for a_I and get an expression for point v_I in terms of Q_i, P and \bar{P} , which are all calculable based on the input of the diagram calculation. Similarly, we can define

$$v_{II} = a_{II} Q_{A+1} + (1 - a_{II} Q_A), \quad (4.16)$$

and solve for the only a_{II} that gives $\bar{x} = 0$. $v_I - v_{II}$ is a spacelike vector, and the separation of the two points can be measured by the Lorentz invariant quantity $-(v_I - v_{II})^2$. The smaller this separation is, more singular the nearby region would be. One can denote the midpoint between v_I and v_{II} to be v ,

$$v \equiv (v_I + v_{II}) / 2. \quad (4.17)$$

Naively this can be thought of as the most singular point. In our numerical program, we choose v to be the origin of the coordinate system for l , although we shall not assume this in the following discussion.

4.2.4 Deformation in All Four Regions

Now we shall propose a specific deformation by specifying the corresponding 4-vector $\kappa_0(l)$. As seen before, the contour eventually will deform into the complex space by adding an imaginary part, $i\kappa(l)$, and $\kappa(l)$ is proportional to κ_0 . The question of how far to deform the contour will be answered later. First we shall present a general formula for $\kappa_0(l)$, and the coefficients of different terms included

in the formula will then be given. Then it will be shown that this method does yield a map of κ_0 and the integral contour can be deformed in the right direction required by the $+i0$ prescription everywhere in the space of l .

Define

$$\kappa_0 = - \sum_{j=1}^N c_j (l - Q_j) + \tilde{c}_+ (P + \bar{P}) - \tilde{c}_- (P + \bar{P}), \quad (4.18)$$

where coefficients c_j , \tilde{c}_+ and \tilde{c}_- are all non-negative functions of l , and the lower index j runs from 1 to N . Different terms are responsible for the deformations in the four shaded regions indicated in Fig. 4.3, and they are carefully turned on and off as one integrates over l along the contour.

For the generic case $1 < A < N - 1$, we choose the coefficients to be

$$\begin{aligned} c_j &= h_-(l - Q_{j-1}) h_+(l - Q_{j+1}) h_-(l - Q_N) \\ &\quad \times h_+(l - Q_{A+1}) g(l) \quad j \in \{2, \dots, A-1\}, \\ c_j &= h_-(l - Q_{j-1}) h_+(l - Q_{j+1}) h_-(l - Q_A) \\ &\quad \times h_+(l - Q_1) g(l) \quad j \in \{A+2, \dots, N-1\}, \\ c_1 &= h_+(l - Q_2) h_-(l - Q_{N-1}) h_+(l - Q_{A+1}) g(l), \\ c_A &= h_-(l - Q_{A-1}) h_+(l - Q_{A+2}) h_-(l - Q_N) g(l), \\ c_{A+1} &= h_+(l - Q_{A+2}) h_-(l - Q_{A-1}) h_+(l - Q_1) g(l), \\ c_N &= h_-(l - Q_{N-1}) h_+(l - Q_2) h_-(l - Q_A) g(l), \\ \tilde{c}_+ &= h_-(l - Q_A) h_-(l - Q_N) \\ &\quad \times (x + \bar{x}) \theta(x + \bar{x} > 0) g_-(l), \\ \tilde{c}_- &= h_+(l - Q_1) h_+(l - Q_{A+1}) \\ &\quad \times [-(x + \bar{x})] \theta(x + \bar{x} < 0) g_+(l). \end{aligned} \quad (4.19)$$

The functions $h_{\pm}(l)$, $g_{\pm}(l)$ and $g(l)$ control the boundaries of regions for nonzero c_j ,

c_+ and c_- , and will be defined below. For the special case $A = 1$, the definitions of coefficients are a bit different,

$$\begin{aligned}
c_j &= h_-(l - Q_{j-1}) h_+(l - Q_{j+1}) h_-(l - Q_1) \\
&\quad \times h_+(l - Q_1) g(l) \quad j \in \{3, \dots, N-1\}, \\
c_1 &= h_-(l - Q_{N-1}) h_+(l - Q_3) g(l), \\
c_2 &= h_+(l - Q_3) h_+(l - Q_1) g(l), \\
c_N &= h_-(l - Q_{N-1}) h_-(l - Q_1) g(l), \\
\tilde{c}_+ &= h_-(l - Q_N) (x + \bar{x}) \theta(x + \bar{x} > 0) g_-(l), \\
\tilde{c}_- &= h_+(l - Q_2) [-(x + \bar{x})] \theta(x + \bar{x} < 0) g_+(l).
\end{aligned} \tag{4.20}$$

For the other special case $A = N - 1$,

$$\begin{aligned}
c_j &= h_-(l - Q_{j-1}) h_+(l - Q_{j+1}) h_-(l - Q_N) \\
&\quad \times h_+(l - Q_N) g(l) \quad j \in \{2, \dots, N-2\}, \\
c_1 &= h_+(l - Q_2) h_+(l - Q_N) g(l), \\
c_{N-1} &= h_-(l - Q_{N-2}) h_-(l - Q_N) g(l), \\
c_N &= h_+(l - Q_2) h_-(l - Q_{N-2}) g(l), \\
\tilde{c}_+ &= h_-(l - Q_{N-1}) (x + \bar{x}) \theta(x + \bar{x} > 0) g_-(l), \\
\tilde{c}_- &= h_+(l - Q_1) [-(x + \bar{x})] \theta(x + \bar{x} < 0) g_+(l).
\end{aligned} \tag{4.21}$$

The factors $h_{\pm}(l - Q_i)$ contained in c_j are functions of momentum l . For the purpose of obeying $+i0$ prescription, we want h_+ to vanish only in the forward lightcone from Q_i , and want h_- to vanish only in the backward lightcone from Q_i . The above requirement can be satisfied if

$$h_-(k) = \frac{(|\vec{k}| + E_k)^2}{(|\vec{k}| + E_k)^2 + M_1^2} \theta(E_k > -|\vec{k}|), \tag{4.22}$$

and

$$h_+(k) = \frac{(|\vec{k}| - E_k)^2}{(|\vec{k}| - E_k)^2 + M_1^2} \theta(E_k < |\vec{k}|) . \quad (4.23)$$

In the above definitions, E_k and \vec{k} are the energy and the spatial components of the 4-vector k . Constructed as such, it can be easily proved that $h_+(k) = 0$ in the forward lightcone from $l = 0$ and $h_-(k) = 0$ in the backward lightcone from $l = 0$. The magnitude of this function is affected by our choice for the parameter M_1 . In our numerical program, the default value is $M_1 = 0.05 (P \cdot \bar{P})^{1/2}$.

Factor $g(l)$ is also included in the definition of c_j , and it is used to make sure the contour deformation is relatively larger near the possible double parton scattering singularity compared to those region far away from this singularity. It is in fact quite rare to have a configuration of the external momentum that allows the presence of double parton singularity, but the numerical convergence in the region near the point v as we defined above is usually marginal. So we want to deform the contour away from v as much as possible. The form of $g(l)$ we adopt is defined to be

$$g(l) = \frac{\gamma_1 M_2^2}{(l^0 - v^0)^2 + (\vec{l} - \vec{v})^2 + M_2^2} . \quad (4.24)$$

The dimensionless parameter γ determines the magnitude of $g(l)$ right at v , and is by default set to be 0.7 in our numerical program. The other parameter M_2 is by default set to be $M_2 = (P \cdot \bar{P})^{1/2}$, and it affects the size of the deformation in regions further away from the double parton scattering region.

The coefficient c_+ includes a factor $g_-(l)$ and the coefficient c_- includes a factor $g_+(l)$. If taking the top region as an example, we want the contour deformation to be large on the forward lightcones and the spacelike intersections of forward lightcones in the top region, and we want the deformation to be small when the contour is far away from any singular region. This can be roughly satisfied by forcing the magnitude of $\kappa_0(l)$ to maximize on the surface of the upper branch of a hyperbola, with the

forward lightcone from the point v as its asymptotes, since most forward lightcones from vertices in the left and right region will be near such a hyperbola. Therefore, we find it could be helpful to let c_+ , which regulates the deformation in the top region, to include the factor

$$g_-(l) = \frac{\gamma_2}{1 + (1 - E/\omega)^2} , \quad (4.25)$$

where γ_2 is a dimensionless parameter that affects the size of the contour deformation near all forward lightcones. The parameter E and ω are defined as

$$\begin{aligned} E &= l^0 - v^0 , \\ \omega &= \left[(\vec{l} - \vec{v})^2 + M_3^2 \right]^{1/2} , \end{aligned} \quad (4.26)$$

in which the parameter M_3 has the dimension of mass and impacts when to maximize c_+ . We set the default values of γ_2 and M_3 to be 1 and $(P \cdot \bar{P})^{1/2}$ in our numerical program. Similarly, we choose the factor $g_+(l)$ in c_- to be

$$g_+(l) = \frac{\gamma_2}{1 + (1 + E/\omega)^2} , \quad (4.27)$$

with the same definitions for γ_2 , E and ω as above. This way the deformation will also approximately be large near the singular points and surfaces in the bottom region and gradually decreases as the contour moves to domains without any cones.

Next, we shall first introduce some useful notations for the lightcones, and then we will try to find out whether the general formula for κ_0 defined in Eq. (4.18) is really able to yield the correct deformation near singularities by tracking the values of $\kappa_0 \cdot (l - Q_i)$. The generic case will be studied before the special case with $A = 1$ or $A = N - 1$.

4.2.5 Notations for Cones

In order to make the later analysis more compact, we will name different parts of a light cone, and use the cone from Q_i as an example. The forward lightcone will be denoted by $C_+(Q_i)$,

$$(l - Q_i)^2 = 0, \quad (l - Q_i) \cdot (P + \bar{P}) > 0, \quad (4.28)$$

and the forward lightcone plus its interior will be denoted by \bar{C}_+ ,

$$(l - Q_i)^2 \geq 0, \quad (l - Q_i) \cdot (P + \bar{P}) > 0. \quad (4.29)$$

The dot products of $(l - Q_i)$ and $(P + \bar{P})$ are positive in the above two cases because the two factors are both timelike vectors pointing in the same time direction. We also denote the backward lightcone from Q_i ,

$$(l - Q_i)^2 = 0, \quad (l - Q_i) \cdot (P + \bar{P}) < 0, \quad (4.30)$$

by $C_-(Q_i)$, and denote the backward lightcone plus its interior,

$$(l - Q_i)^2 \geq 0, \quad (l - Q_i) \cdot (P + \bar{P}) < 0. \quad (4.31)$$

The dot products are now negative because the two factors are timelike vectors pointing in the opposite time directions.

4.2.6 The Coefficients for $2 \leq A \leq N - 2$

4.2.6.1 The Coefficients c_j for $j \in \{2, \dots, A - 1\}$

We can have $\kappa_0 \cdot (l - Q_i) \geq 0$ for l on the lightcone from any Q_i as long as every single term in the definition of κ_0 can have a non-negative dot product with the same

factor $(l - Q_i)$. Let us talk about c_j with $j \in \{2, \dots, A - 1\}$ first. We define the term in κ_0 that contains c_j to be

$$\kappa_j = -c_j (l - Q_j) . \quad (4.32)$$

For $l \in C_{\pm}(Q_i)$ with any i other than j , we find the product

$$\begin{aligned} \kappa_j \cdot (l - Q_i) &= -c_j (l - Q_i)^2 + c_j (Q_j - Q_i) \cdot (l - Q_i) \\ &= c_j (Q_j - Q_i) \cdot (l - Q_i) . \end{aligned} \quad (4.33)$$

We first consider the case of $j < i \leq A$ where $Q_j \in \bar{C}_-(Q_i)$. Therefore, for $l \in C_-(Q_i)$ we would have $\kappa_j \cdot (l - Q_i)$ as desired since c_j is chosen to be non-negative already. However, for $l \in C_+(Q_i)$ the same dot product will never be greater than zero. As a result, we have to make c_j vanish for $l \in C_+(Q_i)$ in order to make the product non-negative for all l on the cone from Q_i . It is true that within the given range of i and j in this particular case we always have $C_+(Q_i) \subset \bar{C}_+(Q_{j+1})$. We can then include the factor $h_+(l - Q_{j+1})$ in c_j so that it will vanish for $l \in C_+(Q_i)$.

Similarly, if we consider the case where $1 \leq i < j$ we can get $Q_j \in \bar{C}_+(Q_i)$ for any $j \in \{2, \dots, A - 1\}$. It is ensured that $\kappa_j \cdot (l - Q_i) \geq 0$ for any $l \in C_+(Q_i)$, but again the same dot product has the wrong sign for $l \in C_-(Q_i)$, and thus c_j has to vanish on the backward lightcone from Q_i . Using the nesting relation $C_-(Q_i) \subset \bar{C}_-(Q_{j-1})$, we find we can acquire the correct sign by including a factor of $h_-(l - Q_{j-1})$ in the coefficient c_j .

So far we have only studied the cases where $i \leq A$. When $A + 1 \leq i \leq N$, the two vertices Q_i and Q_j would be spacelike separated, and $\kappa_j \cdot (l - Q_i)$ can be either positive or negative for l anywhere on the lightcone from Q_i , based on Eq.(4.33). Therefore, in order to make the dot product non-negative, we force c_j to vanish for any $l \in C_{\pm}(Q_i)$. Since it is true for any $i \in [A + 1, N]$ that $C_+(Q_i) \subset \bar{C}_+(Q_{A+1})$ and $C_-(Q_i) \subset \bar{C}_-(Q_N)$, we include factor $h_+(l - Q_{A+1})$ and factor $h_-(l - Q_N)$ in

the definition of c_j . The factor $g(l)$ is also included because we want to turn off the deformation gradually when l^0 and \vec{l} are large.

4.2.6.2 The Coefficients c_j for $j = A$

In this case, when $i < j = A$, the dot product $\kappa_j \cdot (l - Q_i)$ is again positive for $l \in C_+(Q_i)$ and negative for $l \in C_-(Q_i)$ based on Eq. (4.33), and thus we still want the factor $h_-(l - Q_{j-1})$ in c_j (or c_A). However, unlike $j < A$, there is no i that could be greater than $j = A$ and not larger than A , so we do not need the factor $h_+(l - Q_{j+1})$ in c_j any more.

For $A + 2 \leq i \leq N$, Q_i and Q_A are spacelike, and $\kappa_A \cdot (l - Q_i)$ can be either positive or negative for $l \in C_\pm(Q_i)$. The coefficient c_A needs to vanish on the lightcones from such Q_i to generate the correct deformation. The nesting relations now become $C_+(Q_i) \subset \bar{C}_+(Q_{A+2})$ and $C_-(Q_i) \subset \bar{C}_-(Q_N)$. Accordingly, we include the factor $h_+(l - Q_{A+2})$ and the factor $h_-(l - Q_N)$ in c_A .

We have not covered the case of $i = A + 1$ yet. Obviously Q_A and Q_{A+1} are lightlike, and $Q_A \in C_+(Q_{A+1})$. The condition $\kappa_j \cdot (l - Q_i) \geq 0$ are always satisfied for any $l \in C_+(Q_i)$ when $i = A + 1$ and $j = A$. For $l \in C_-(l - Q_{A+1})$, the dot product carries the “wrong sign”, and c_A has to vanish on the backward cone from Q_{A+1} . We notice that $C_-(Q_{A+1}) \subset \bar{C}_-(Q_N)$. The factor $h_-(l - Q_N)$ that we have already included in c_A will therefore ensure that c_A goes to zero for $l \in Q_-(Q_{A+1})$.

4.2.6.3 The Coefficients c_j for $j = 1$

Just as the analysis we have done for c_A , the definition of c_1 is similar to c_j for $1 < j < A - 1$ but not identical. We do not need to include the factor $h_-(l - Q_{j-1})$ because there is no Q_i that satisfies $1 < i \leq j = 1$ and we are automatically free of some problems in which $\kappa_j \cdot (l - Q_i)$ has the “wrong” sign. We can force c_1 to vanish for $l \in C_\pm(Q_i)$ with $A + 1 \leq i \leq N - 1$ by putting in the factor $h_+(l - Q_{A+1})$ and the factor $h_-(l - Q_{N-1})$.

4.2.6.4 The Coefficients c_j for $j \in \{A+1, \dots, N\}$

The coefficients c_j for $A+1 \leq j \leq N$ can be defined in the same way as we define those coefficients c_j for $1 \leq j \leq A$.

4.2.6.5 The Coefficient \tilde{c}_+

We have defined a group of coefficients c_j for $j \in \{1, \dots, N\}$, and have proved the corresponding κ_j can yield $\kappa_j \cdot (l - Q_i) \geq 0$ for any $l \in C_{\pm}(Q_i)$, where the index i can be any integer between 1 and N . Moreover, one can show, in a straightforward but tedious way, that $\sum \kappa_j \cdot (l - Q_i) > 0$ for all $l \in C_{\pm}(Q_i)$ except for those loop momentum on the pinched singularities in the left and right region in Fig. 4.3. This is exactly what we want, because in order to have better control over the numerical convergence of the whole integral, we need the contour to be deformed from a singularity whenever it is possible. However, we have not achieved the same objective yet in a large part of the top and bottom region with the collection of κ_j , e.g., $\sum \kappa_j = 0$ for l on the intersection of $C_+(Q_2)$ and $C_+(Q_{A+2})$. In fact, κ_j are mostly turned off in the top and bottom region because $\kappa_j \cdot (l - Q_i)$ could be negative on the spacelike intersection of lightcones, as we discussed earlier.

Fortunately, this problem can be easily resolved by putting in a new term κ_+ to the imaginary part of ℓ , and $\kappa_+ \cdot (l - Q_i) > 0$ is always true for $l \in C_+(Q_i)$ as long as κ_+ is timelike and points to the positive direction in time. We thus choose $\kappa_+ \propto (P + \bar{P})$. The formal definition of this new term is

$$\kappa_+ \equiv \tilde{c}_+ (P + \bar{P}) . \quad (4.34)$$

Obviously $\kappa_+ \cdot (l - Q_i)$ will have the “wrong ” sign for $l \in C_-(Q_i)$, and we need to make sure \tilde{c}_+ vanishes for those l . This requirement can be met by including the factor $h_-(l - Q_A)$ and the factor $h_-(l - Q_N)$ since all other backward cones are nested inside the backward cone from either Q_A or Q_N .

In practice, not only do we want to have nonzero deformation at the singularities, but we also want to suppress the deformation when the contour is not near any singularity. For this purpose, factors $(x + \bar{x})\theta(x + \bar{x} > 0)$ and $g_-(l)$ are included when defining \tilde{c}_+ . As we argued before, the function $g_-(l)$ approaches approximately 1 near the forward lightcones in the top region, and $x + \bar{x}$ will grow with l along the cones. The outcome is that the contour can be deformed significantly away from the forward lightcones when l moves away from the double parton scattering region. However, if the spatial component \vec{l} is fixed, $(x + \bar{x})g_-(l)$ will decrease to zero when its 0-component gets bigger, which effectively turns off the deformation.

4.2.6.6 The Coefficient \tilde{c}_-

Similar to what we have done to the coefficient \tilde{c}_+ in the top region, we want to add a new term κ_- to κ_0 so that $\kappa \cdot (l - Q_i)$ is positive for any $l \in C_-(Q_i)$ in the bottom region. Once again this can be easily achieved as long as κ_- is timelike and points to the negative direction in time. In particular, we can define

$$\kappa_- \equiv -\tilde{c}_-(P + \bar{P}) . \quad (4.35)$$

This same κ_- would yield the “wrong” sign for $\kappa_- \cdot (l - Q_i)$ on the forward lightcones from any of the Q_i , and thus \tilde{c}_- has to be turned off on all forward cones. This can be ensured by including in the definition of \tilde{c}_- the factor $h_+(l - Q_1)$ and the factor $h_+(l - Q_{A+1})$, because all other forward cones are nested inside the forward cone from either Q_1 or Q_{A+1} . We also put in factors $-(x + \bar{x})\theta(x + \bar{x} < 0)$ and g_+ to control the deformation in the bottom region.

4.2.7 The Coefficients for $A = 1$

When $A = 1$, the coefficients that appear in the definition of κ_0 need to be specified slightly differently from the generic case where $2 \leq A \leq N - 1$.

The geometric arrangements of the lightcones cones from Q_j for $j \in \{3, \dots, N-1\}$ is the same as those of the lightcones from vertices in the right region of the generic case. Therefore, the definitions of c_j completely follows those of c_j for $3 \leq j \leq N-1$ in the generic case.

On the other hand, the coefficients $c_1, c_2, c_N, \tilde{c}_+$ and \tilde{c}_j need to be modified. Let us start with c_1 . For $\kappa_1 \propto -(l - Q_1)$, it points in the right direction for $l \in C_+(Q_2)$ and $l \in C_-(Q_N)$, but it points in the “wrong” direction for $l \in C_-(Q_2)$ and $l \in C_+(Q_N)$. Furthermore, $\kappa_1 \cdot (l - Q_i)$ for $i \in \{3, \dots, N-1\}$ can be either positive or negative. To summarize, we want c_1 to vanish for l on all forward lightcones nested in the forward cone from Q_3 and for l on all backward cones nested inside the backward cone from Q_{N-1} . The above requirements on c_1 can be realized by including factors $h_+(l - Q_3)$ and $h_-(l - Q_{N-1})$.

The analysis for the coefficient c_2 is similar. The vector κ_2 points in the correct direction for l on backward cones from all Q_i except for Q_2 itself, because the cone from Q_2 is nested inside any other backward cone in the problem. Accordingly, κ_2 will point in the “wrong” direction for l on forward cones from all Q_i except for Q_i . We thus require c_2 to vanish on all the forward cones except for that from Q_2 . It is achieved by including in c_2 factors $h_+(l - Q_1)$ and $h_+(l - Q_3)$.

Analogously to c_2 , c_N can point in the right direction for all l by including in it factors $h_-(l - Q_1)$ and $h_-(l - Q_{N-1})$.

For \tilde{c}_+ , the vector $\kappa_+ \propto (P + \bar{P})$ obviously points in the right direction for $l \in C_+(Q_i)$ with any valid i choice, and points in the “wrong” direction for $l \in C_-(Q_i)$ with all valid i choice. We have a very convenient nesting relation to make use of when $A = 1$ because all backward cones are nested inside the one from Q_N , and that means, compared to the generic case, we only need to include in \tilde{c}_+ the factor $h_-(l - Q_N)$ in order to make \tilde{c}_+ vanish for l on all backward lightcones. Factors $(x + \bar{x})\theta(x + \bar{x})$ and $g_-(l)$ is again used to control the relative size of the deformation in different sub regions. The construction for \tilde{c}_- is similar to that of \tilde{c}_+ .

4.2.8 The Coefficients for $A = N$

The construction of the coefficients in the definition of κ_0 follows the same logic as that used in the special case of $A = 1$.

4.2.9 Size of the Deformation

We have so far determined the directions of the vector κ everywhere in the space of l by specifying κ_0 and its coefficients as functions of l . As defined before,

$$\kappa(l) = \lambda(l) \kappa_0(l) , \quad (4.36)$$

and the real scalar factor $\lambda(l)$ controls the size of the deformation together with κ_0 . To stick to the $+i0$ prescription, we need to ensure the integrand does not run into any singularity as $\lambda(l)$ is increased from zero to its final value, otherwise the modified contour might enclose different poles and thus have different residues from the original contour. It is trivial when $\lambda(l)$ is infinitesimally small, because under the guidance of κ_0 the contour has already started to deform away from the non-pinched singularities in the correct direction near the original route. However, the practical $\lambda(l)$ should be as large as possible. Being too close to the singularities will undermine the numerical convergence of the integral. On the other hand, one would guess $\lambda(l)$ cannot be arbitrarily big, because for certain values of λ it could be true that

$$(l - Q_i + i\lambda(l) \kappa_0(l))^2 = 0 \quad (4.37)$$

for some l away from the original singularities, while $\kappa_0(l) \cdot (l - Q_i) > 0$ for l near those non-pinched singularities. It is also possible that when the contour get deformed away from one cone, Q_i , it might end up coming across the singularity near another cone, Q_j , which means

$$(l - Q_j + i\lambda(l) \kappa_0(l))^2 = 0 \quad (4.38)$$

The above analysis implies that we should find out the rules about how far the contour can be deformed. The upper limit for $\lambda(l)$ needs to be set. In order to resolve this problem, it is helpful to first see where the new singularities could be in terms of the corresponding values of $\lambda(l)$. We can better formulate this subject by requiring the maximum value, $\lambda_f(l)$, to be the minimum of a number, $\lambda_i(l)$, defined for each propagator, a universal choice, $\lambda_0(l)$, to be determined later, and a constant number, λ_c , whose default value is 1 in our numerical program:

$$\lambda_f(l) = \text{Min} [\text{Min} \{ \lambda_i(l) \}, \lambda_0(l), \lambda_c] . \quad (4.39)$$

We first determine what λ_i should be for each propagator. The new singularity related to the cone from Q_i appears when

$$0 = D_i = (l - Q_i + i\lambda\kappa_0)^2 = (l - Q_i)^2 + 2i\lambda\kappa_0 \cdot (l - Q_i) - \lambda^2\kappa_0^2 . \quad (4.40)$$

The root of this quadratic equation of λ is

$$\lambda = \frac{1}{\kappa_0^2} \left\{ i \kappa_0 \cdot (l - Q_i) \pm \sqrt{\kappa_0^2 (l - Q_i)^2 - [\kappa_0 \cdot (l - Q_i)]^2} \right\} . \quad (4.41)$$

We can see that since the solution for $\lambda(l)$ can be either real or complex, thus the new singularity does not necessarily exist. The poles can have real parts when $[\kappa_0 \cdot (l - Q_i)]^2 < \kappa_0^2 (l - Q_i)^2$, but they will not be able to get near the real axis unless $[\kappa_0 \cdot (l - Q_i)]^2 \ll \kappa_0^2 (l - Q_i)^2$ are satisfied. In that case, one of two poles of λ can have a finite positive real part and the imaginary part of the same pole almost vanishes, which means the contour can get very close to this pole as one increases λ . The special situation is when $\kappa_0 \cdot (l - Q_i) = 0$ and thus the same pole sits right on the positive real axis. The absolute value of this pole would be

$$\begin{aligned}
|\lambda| &= \\
&= \frac{1}{|\kappa_0^2|} \sqrt{[\kappa_0 \cdot (l - Q_i)]^2 + [\kappa_0^2 (l - Q_i)^2 - (\kappa_0 \cdot (l - Q_i))^2]} \\
&= \sqrt{\frac{(l - Q_i)^2}{\kappa_0^2}} .
\end{aligned} \tag{4.42}$$

Obviously we can avoid being too close to or even encountering this new singularity easily by defining the corresponding λ_i to be smaller than the absolute value of this real pole. We will talk about the specific form for λ_i later.

The poles can be purely imaginary when $\kappa_0^2 (l - Q_i)^2 < [\kappa_0 \cdot (l - Q_i)]^2$, and the exact expressions for them will be

$$\begin{aligned}
\lambda &= \frac{i}{\kappa_0^2} \left\{ \kappa_0 \cdot (l - Q_i) \right. \\
&\quad \left. \pm \sqrt{[\kappa_0 \cdot (l - Q_i)]^2 - \kappa_0^2 (l - Q_i)^2} \right\} .
\end{aligned} \tag{4.43}$$

As we increase λ from zero along the positive real axis, the contour will never get close to any new singularity since the poles are both on the imaginary axis. Given this, one would certainly want to set λ_i to be as large as possible so that the contour can be far away from the original singularity. However, there are still restrictions on what one can actually use for λ_i in this region of l . The most important constraint comes from the requirement that the Jacobian determinant present in Eq. (4.7) needs to be small. If the change in κ as we vary l is too sharp, or equivalently, if the gradient of κ with respect to l is too large or even singular, the numerical convergence of the integral in Eq. (4.7) will remain marginal due to a large or even singular Jacobian, even if we have deformed the contour well away from the singularities. To fix this, we have to make sure that λ_f is continuous across all possible boundaries at all times and that the gradient of λ_f is never too large. Next we will discuss the construction of $\lambda_i(l)$ and $\lambda_0(l)$ in more details and see how the above criteria can be satisfied.

For the purpose of defining λ_i , we will first divide the l space into three different regions. The first region has

$$2[\kappa_0 \cdot (l - Q_i)]^2 < \kappa_0^2 (l - Q_i)^2 , \quad (4.44)$$

and it encloses all the sub regions where one of the two λ poles in Eq. (4.41) can be either close or right on the positive real axis of λ . Therefore, we need a λ_i that is small enough so that the contour will not come across any new singularities. Particularly, we can choose λ_i to be only half of the absolute value of the poles,

$$\lambda_i^2 = \frac{\kappa_0^2 (l - Q_i)^2}{(2\kappa_0^2)^2} \quad (4.45)$$

for $2[\kappa_0 \cdot (l - Q_i)]^2 < \kappa_0^2 (l - Q_i)^2$.

The second region is where

$$0 < \kappa_0^2 (l - Q_i)^2 < 2[\kappa_0 \cdot (l - Q_i)]^2 . \quad (4.46)$$

Note that at the boundary between region I and region II λ_i has to be continuous.

We can define

$$\lambda_i^2 = \frac{4[\kappa_0 \cdot (l - Q_i)]^2 - \kappa_0^2 (l - Q_i)^2}{(2\kappa_0^2)^2} \quad (4.47)$$

for $0 < \kappa_0^2 (l - Q_i)^2 < 2[\kappa_0 \cdot (l - Q_i)]^2$,

which does match the definition for λ_i when $\kappa_0^2 (l - Q_i)^2 = 2[\kappa_0 \cdot (l - Q_i)]^2$. The third region, which covers the rest of the l space, is when

$$\kappa_0^2 (l - Q_i)^2 < 0 , \quad (4.48)$$

and accordingly, one can define λ_i in this region as well so that it can match the definition for λ_i in region II at the boundary, where $\kappa_0^2 (l - Q_i)^2 = 0$. This motivates us to choose in the third region that

$$\lambda_i^2 = \frac{4[\kappa_0 \cdot (l - Q_i)]^2 - 2\kappa_0^2(l - Q_i)^2}{(2\kappa_0^2)^2} \quad (4.49)$$

for $\kappa_0^2(l - Q_i)^2 < 0$.

Note that the above definitions for λ_i are smooth functions of l almost everywhere, except when the denominator $\kappa_0^2 = 0$. It means the gradient of λ_i , hence the gradient of $\kappa(l)$, should be finite whenever κ_0 is not lightlike. On the other hand, the 4-vector κ_0 cannot be lightlike unless its argument l is on the collinear lines. If l does sit on the collinear singularities along one of the two lines $l = Q_i + z(Q_{i+1} - Q_i)$ and $l = Q_i + z(Q_{i-1} - Q_i)$ that meet at $l = Q_i$, both the numerator and the denominator of λ_i in any of the three regions will be zero. Naively it could easily be true that the resulting λ_i is also zero and gets picked to be λ_f since it is the smallest among λ_0 , λ_c and $\min_i [\lambda_i]$. At the same time the gradient of this λ_i , and hence the corresponding κ , could be singular. We do not want this to happen, and thus need to discuss in more details about the values of λ_i near the collinear lines we have just mentioned. However, for l on all other collinear singularities that are not included above, it does not matter if the gradient of $\lambda_i(l)$ is singular or not, because for those points the numerator of $\lambda_i(l)$ would not be zero. Therefore, λ_i will be infinitely large and cannot be chosen to be λ_f , the upper limit for $\lambda(l)$ at that point.

The optimal scenario for this issue would be that there actually is a positive and finite minimum value that λ_i can ever get as small as. If it were true, then we could choose a smooth function of l , $\lambda_0(l)$, which will always be smaller than this same minimum value for λ_i near the collinear singularities closest to Q_i . This way the gradient of λ_f will never be singular, even though in those regions that we are now considering the gradient of λ_i can be very singular. To see whether this scenario applies, we need to find out what the expressions for λ_i will become near the collinear singularities. We first rewrite the definition for κ_0 as

$$\begin{aligned}
\kappa_0 &= - \sum_{j=1}^N c_j (l - Q_j) + \tilde{c}_+(P + \bar{P}) - \tilde{c}_-(P + \bar{P}) \\
&= -C(l - Q_i) + R_i \ ,
\end{aligned} \tag{4.50}$$

where

$$\begin{aligned}
C &= \sum_{j=1}^N c_j \ , \\
R_i &= \sum_{j=1}^N c_j (Q_j - Q_i) + \tilde{c}_+(P + \bar{P}) - \tilde{c}_-(P + \bar{P}) \ .
\end{aligned} \tag{4.51}$$

Under this new notation, we can derive that

$$\kappa_0 \cdot (l - Q_i) = -C(l - Q_i)^2 + (l - Q_i) \cdot R_i \ , \tag{4.52}$$

and another term that also appears in the definition of λ_i ,

$$\kappa_0^2 = C^2 (l - Q_i)^2 - 2C(l - Q_i) \cdot R_i + R_i^2 \ . \tag{4.53}$$

The third term (also the last term), $(l - Q_i)^2$, included in λ_i can be related to the other two terms by eliminating $(l - Q_i) \cdot R_i$ from the above two equations, and then one can obtain

$$(l - Q_i)^2 = -\frac{1}{C^2} \kappa_0^2 - \frac{2}{C} \kappa_0 \cdot (l - Q_i) + \frac{1}{C^2} R_i^2 \ . \tag{4.54}$$

Through tedious but straightforward analysis, we can find out that as l moves towards the collinear singularities closest to Q_i , the term R_i^2 tends to behave like $[(l - Q_i)^2]^2$, and approaches 0 very fast. The consequence of this observation is R_i^2 can therefore be neglected in this region since it is a higher order term in the small quantity $(l - Q_i)^2$ compared to κ_0^2 and $\kappa_0 \cdot (l - Q_i)$. After making this approximation, we can have

$$2\kappa_0 \cdot (l - Q_i) \approx -C(l - Q_i)^2 - \frac{1}{C} \kappa_0^2 . \quad (4.55)$$

If we square Eq. (4.55) and divide both sides of the equation by 2, we shall get

$$\begin{aligned} 2[\kappa_0 \cdot (l - Q_i)]^2 &\approx \kappa_0^2(l - Q_i)^2 \\ &+ \frac{C^2}{2} [(l - Q_i)^2]^2 + \frac{1}{2C^2} [\kappa_0^2]^2 \\ &> \kappa_0^2(l - Q_i)^2 , \end{aligned} \quad (4.56)$$

which means l would never be in the first region defined above when it is very close to the collinear singularities along the two lines $l = Q_i + z(Q_{i+1} - Q_i)$ and $l = Q_i + z(Q_{i-1} - Q_i)$ that meet at $l = Q_i$. However, the possibility of l being in the other two regions cannot be ruled out, and it will depend on the sign of $\kappa_0^2(l - Q_i)^2$ whether l belongs to region II or III. Nevertheless, we can figure out what the global lower limit of λ_i is by studying the lower limits of the same function in two regions separately. In region II, if we replace $\kappa_0 \cdot (l - Q_i)$ in Eq. (4.47) by using the approximated relation worked out in Eq. (4.55), we can conclude

$$\begin{aligned} \lambda_i^2 &= \frac{\kappa_0^2(l - Q_i)^2 + C^2[(l - Q_i)^2]^2 + [\kappa_0^2]^2 / C^2}{4(\kappa_0^2)^2} \\ &= \frac{(l - Q_i)^2 / \kappa_0^2 + C^2 [(l - Q_i)^2 / \kappa_0^2]^2}{4} + \frac{1}{4C^2} \\ &> \frac{1}{4C^2} . \end{aligned} \quad (4.57)$$

Note that in the second line in the above equation, the first term is always non-negative, and it can vanish only when l approaches the boundary between region II and III which is $\kappa_0^2(l - Q_i)^2 = 0$. Similarly, in region III we can replace $\kappa_0 \cdot (l - Q_i)$ in Eq. (4.49) using Eq. (4.55), we will find

$$\lambda_i^2 = \frac{C^2[(l - Q_i)^2]^2 + [\kappa_0^2]^2 / C^2}{4(\kappa_0^2)^2} > \frac{1}{4C^2} . \quad (4.58)$$

Again, λ_i^2 can approach $1/4C^2$ only when l is near the boundary between region II and III. In summary, for any l near the collinear singularities along the lines that meet at $l = Q_i$, it is always true that

$$\lambda_i > \frac{1}{2C} . \quad (4.59)$$

Since we want continuous λ_f everywhere in the l space, including the region near collinear singularities, we can define

$$\lambda_0(l) = \frac{1}{4C(l)} , \quad (4.60)$$

so that λ_f will be set to be the same smooth function of l across all collinear singularities.

4.3 Numerical Results

We have developed a computer program that incorporates the contour deforming mechanism described in this thesis, using C++. The program is designed to calculate the matrix element \mathcal{M} by evaluating the integral presented in Eq. (4.7). For the corresponding virtual loop Feynman diagram with N external photons, all N external momentum p_i and photon polarizations ϵ_i will be given as inputs before the computer code is executed. Among them, 2 are incoming photons and the rest are outgoing. To start with, we choose p_1 and p_2 to be the momentum of the two incoming photons, and let their transverse components vanish. However, we are interested in more than just one diagram. Our goal is to compute the amplitude of 2 photons with fixed momentum scattering to produce $(N - 2)$ other photons also with pre-determined momentum, regardless of their relative positions around the virtual loop in the graph. As a result, for N photons we need to consider all of the non-cyclic permutations of initial labeling of photon legs. There are $(N - 1)!$ such permutations in total. After a permutation, as illustrated in Fig. 4.3, photon A and photon N will be initialized

to have the incoming momentum and polarizations. The amplitude at interest will finally be acquired by summing the graphs over all possible permutations.

We will now pick an observable \mathcal{O} that can best characterize our numerical calculation. We specify the helicities in a form $\{h_1, h_2, \dots, h_N\}$, with h_1 and h_2 being the helicity of incoming photons. According to our notation, h_1 and h_2 are actually the negative of physical polarizations because we have defined all external momentum to be outgoing for convenience. For a given set of helicities for the external photons, the phase of the matrix element \mathcal{M} actually differs for different conventions for the photon polarization vector. In practice, this phase does not have any effect since we only concern about the absolute value of the scattering amplitude, $|\mathcal{M}|$. We can choose any convention for the polarization vector $\epsilon_\mu(k, s)$ before squaring the amplitude, and the final result will be proportional to $|\mathcal{M}|$ and will not depend on where we start with. Moreover, we want to make \mathcal{O} dimensionless, since we care more about the interaction between the external momentum plus helicity configurations and the final amplitudes. As a result, we need to divide $|\mathcal{M}|$ by $(\sqrt{s})^{4-N}$, where \sqrt{s} is the center-of-mass energy of the initial photon pair. Applying the same logic, we also want to remove the effects brought by the coupling constant by including a factor of $1/\alpha^{N/2}$. As a result, we want to show

$$\mathcal{O} = \frac{(\sqrt{s})^{4-N} |\mathcal{M}|}{\alpha^{N/2}}, \quad (4.61)$$

in our subsequent plots.

In the computer code, we compute \mathcal{M} in a Monte Carlo style, and we deform the contour away from its original path in the complex plane. To achieve optimal numerical convergence, we adopt K different methods of importance sampling in regions where two or more lightcones intersect so that more points can be used where bigger fluctuations are expected. The probability for the code to execute method i is α_i , for which points are sampled according to the distribution $g_i(l)$. It

is straightforward to see that the value of the original integral will be retained as we have

$$dl = \sum_i^K \frac{\alpha_i g_i(l) dl}{\sum_i^K \alpha_i g_i(l)}, \quad (4.62)$$

where $\sum_i^K \alpha_i = 1$. The form of the distribution $g_i(l)$ depends on how lightcones intersect. Among the $(N-1)!$ graphs pertaining to the same scattering amplitude, some of them are more singular when the impact parameter b is smaller, because those graphs will have a more severe problem of double parton scattering. So instead of assigning equal weights to all graphs, we put more weights in those more singular graphs when summing them over permutations. We have documented some sampling methods at [45]. In the rest of this section we will display the numerical results of $N=6$ and $N=8$ for several helicity configurations, and then compare them with those using the Feynman parameter method.

4.3.1 N = 6

We choose to compute a group of scattering amplitudes with six photons that are all located along an one-dimensional curve in the space of external momentum. First an initial set of external momentum is given, in which momentum of the two incoming photons, p_1 and p_2 , do not have any transverse component. In our case, we let p_1 point in the $-z$ direction so that the physical direction of photon 1 points in the $+z$ direction according to our notation, while we let p_2 point in the $+z$ direction. The starting point of outgoing momentum used in our computer code is arbitrarily chosen to be

$$\begin{aligned}
\vec{p}_3 &= (33.5, 15.9, 25.0) , \\
\vec{p}_4 &= (-12.5, 15.3, 0.3) , \\
\vec{p}_5 &= (-10.0, -18.0, -3.3) , \\
\vec{p}_6 &= (-11.0, -13.2, -22.0) .
\end{aligned} \tag{4.63}$$

A specific curve can be acquired when we rotate the spatial components of all outgoing momentum in this given set of external momentum around the y-axis. If the rotation angle is θ and the momentum afterwards is called k_i , then for $i \in \{3, 4, 5, 6\}$, the x and z components will be changed to

$$\begin{aligned}
k_{ix} &= p_{ix} \cos \theta + p_{iz} \sin \theta , \\
k_{iz} &= -p_{ix} \sin \theta + p_{iz} \cos \theta ,
\end{aligned} \tag{4.64}$$

and for $i \in \{1, 2\}$ one would have $k_i = p_i$.

In Fig. 4.5, numerical results are plotted versus θ for the dimensionless observable $s |\mathcal{M}| / \alpha^3$, which is independent of the choice for the coupling constant α . The Monte Carlo integration is performed over the deformed contour specified earlier in this article. The angle θ ranges from 0 to π , and the momentum configurations at some values of angle θ will be closer to the double parton scattering singularity, of which we expect to see some effect. Also, we compare the numerical results for the helicity choice $++----$ with the analytical results given in [46], and compare the numerical results for the other helicity choice $+- - + +-$ presented in [47]. As indicated in Fig. 4.5, the numerical results agree with the analytical results within the range of inherent statistical fluctuations of Monte Carlo integrations. Through calculating the sums of transverse momentum for all possible subsets of the 4 final-state momentum, we find out the minimum sum is $(p_{T,3} + p_{T,5})^2 \approx 0.0003 s$ when $\theta \approx 2.32$, which means the most singular scattering amplitudes for six photons will probably appear when the final state momentum are rotated around the y-axis to this angle. In fact, we do see a sharp trough near this angle for the helicity $+- - + +-$.

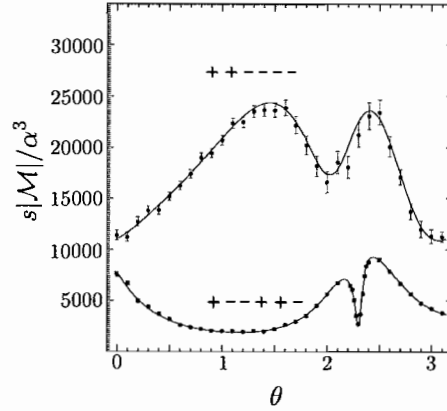


FIGURE 4.5: Numerical results for six photon scattering amplitudes. An arbitrary final state is rotated around the y-axis through angle θ . Furthermore, the results for the helicity choice $++----$ are compared to the analytical curve provided by [46]. The results for the other helicity choice $+-+-+-$ are compared to the analytical curve published in [47]. The numerical result for a specific final state is computed by assigning 10^6 points for each of the $5! = 120$ graphs. This figure is provided by [42].

It needs to be mentioned here that the six photon scattering amplitudes vanishes for $++++++$ and $+++++-$ as calculated in [46]. Our numerical results agree with this analytical prediction within errors. The plots are not shown here since they neither have any interesting structure nor display considerable numerical fluctuations.

As a comparison, we make a similar plot in Fig. 4.6 using the Feynman parameter representation of the integral. The numerical results were published in [41] for θ between 0 and 2. The Monte Carlo integration uses 1×10^6 points for each of the 120 graphs. The numerical results for θ greater than 2 but less than π are calculated later. In order to better examine the angles near $\theta = 2.32$ we use 3×10^6 points for each final state with $\theta > 2$. The running time is approximately half of that for the direct numerical integration when computing the amplitude of the same momentum configuration. Therefore, the numerical results in Fig. 4.5 and those in Fig. 4.6 are comparable. In the latter case, we observe much more severe fluctuations for those amplitudes that have helicity $+- - - -$ and are close to the double parton

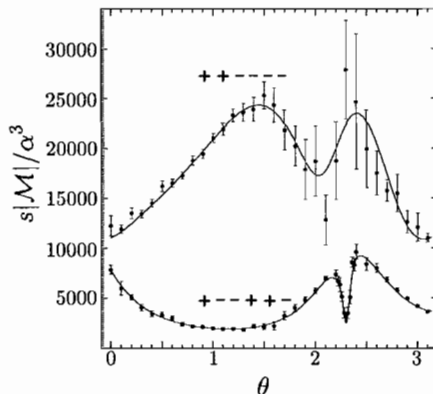


FIGURE 4.6: Results for the six photon amplitude using the Feynman parameter representation, Eq. (4.5). The labeling is as in Fig. 4.5. This figure is provided by [42].

singularity. We have considered where this difference in numerical convergence comes from and have concluded that it may be caused by the different number of powers in the denominators of divergent propagators.

4.3.2 $N = 8$

To test the numerical performance of our contour deformation scheme, we also run the computer code to calculate the eight photon scattering amplitude for final states sitting on a curve in the space of external momentum. Similar to the case of $N = 6$, we first choose an arbitrary set of external momentum. We define the two incoming photon, photon 1 and photon 2, to have only longitudinal momentum, with p_1 pointing in the $-z$ direction while p_2 pointing in the opposite direction. The final state momentum, $p_3 \sim p_8$, should conserve the initial state momentum and we arbitrarily choose them to be

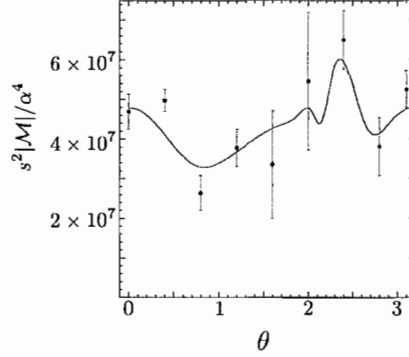


FIGURE 4.7: Numerical results for the eight photon amplitude. The points for which amplitudes are calculated are acquired by rotating an arbitrary set of final state momentum around the y-axis through angle θ . For comparison, the analytical results of [46] are also presented in the same plot. We use 2×10^5 points for each of the $7! = 5040$ graphs, except that we use four times more points, 1×10^6 points, for $\theta = 2.0$ and $\theta = 2.4$ because the external momentum configurations are closer to the double parton scattering singularity for those two sets of momentum. This figure is provided by [42].

$$\begin{aligned}
 \vec{p}_3 &= (33.5, 5.9, 25.0) , \\
 \vec{p}_4 &= (1.5, 24.3, 0.3) , \\
 \vec{p}_5 &= (-19.1, -35.1, -3.3) , \\
 \vec{p}_6 &= (28.2, -6.6, 8.2) , \\
 \vec{p}_7 &= (-12.2, -8.6, 8.2) , \\
 \vec{p}_8 &= (-31.9, 20.1, -38.4) .
 \end{aligned} \tag{4.65}$$

One can produce the entire curve by rotating the final state momentum given above around the y-axis through angle θ . We are again interested in θ in the range from 0 to π .

We follow the same rules that have been devised to deform the contour for $N = 6$ and compute a few different amplitudes for $N = 8$ whose external momentum

are all on the curve specified in last paragraph. The results for the helicity choice $++----$ are displayed in Fig. 4.7, where the dimensionless observable for $N = 8$ that is independent of the coupling constant, $s^2 |\mathcal{M}| / \alpha^4$, is plotted versus the angle θ . We notice the numerical convergence for $N = 8$ is not as good as that for $N = 6$. This can be easily explained by the fact that there are now more singular propagators and many more graphs involved in one amplitude. Nevertheless, the numerical results agree with the analytical results within the error most of the time. Again the direct numerical integration method is the more powerful and effective algorithm compared to the Feynman parameter approach, since the latter method cannot yield numerical results for $N = 8$ at all.

4.4 Conclusion

In this article we have discussed how to calculate the Feynman graph with multiple external photons and a virtual loop using a direct numerical integration method. We construct a scheme to deform the integral contour by adding an imaginary part to the original loop momentum, so that non-pinched singularities can always be avoided. This new method could be useful for the next-to-leading order calculation of two partons scattering to produce more partons in the final state, if one wants to treat the loop momentum and the final state momentum as a single point in a Monte Carlo style integration. Up until now it is not clear if this new method could outperform the more traditional method where the virtual loop is calculated as a whole before integrating over the external momentum. Nevertheless our new method makes it possible to integrate over l directly in the loop momentum space, and in this setup infrared subtractions can be constructed without too much difficulty whenever such subtractions are necessary to remove emergent singularities.

We need to keep it in mind that we have only dealt with graphs with massless fermions running in the virtual loop. Such approximations are well justified when calculating high energy interactions. It remains open how to evaluate the same

scattering amplitudes but with massive fermion loop. The surface on which the denominator of such a propagator vanishes would be hyperbolas instead of lightcones, which could possibly be rid of some or even all collinear and soft singularities. A much simpler contour deformation algorithm might be already sufficient for this scenario. However, new problems can appear such as the threshold singularity.

CHAPTER V

CONCLUSION

Through our theoretical investigations, not only have we developed new methods that can improve the efficiency and accuracy of numerical calculations based on the Standard Model, but we have also learned about what possible theories beyond the Standard Model would look like and how they would impact lab observations. We believe that there is still a lot of work that needs to be done before we can understand the physics near the terascale. In fact, we might never be able to fully grasp what could possibly happen at the LHC. However, it is not the outcome of research but the human's ultimate curiosity toward our universe that has kept science moving forward for thousands of years. We will never lose our faith in the pursuit of truth.

BIBLIOGRAPHY

- [1] Z. Nagy and D. E. Soper, “Matching parton showers to NLO computations,” *JHEP* **10**, 024 (2005).
- [2] M. Kramer and D. E. Soper, “Next-to-leading order QCD calculations with parton showers. I: Collinear singularities,” *Phys. Rev.* **D69**, 054 019 (2004).
- [3] S. Catani and M. H. Seymour, “The Dipole Formalism for the Calculation of QCD Jet Cross Sections at Next-to-Leading Order,” *Phys. Lett.* **B378**, 287–301 (1996).
- [4] X. Artru and G. Mennessier, “String model and multiproduction,” *Nucl. Phys.* **B70**, 93–115 (1974).
- [5] M. G. Bowler, “e+ e- Production of Heavy Quarks in the String Model,” *Zeit. Phys.* **C11**, 169 (1981).
- [6] B. Andersson, G. Gustafson, and B. Soderberg, “A probability measure on parton and string states,” *Nucl. Phys.* **B264**, 29 (1986).
- [7] . Kramer, Michael and D. E. Soper, “Next-to-leading order numerical calculations in Coulomb gauge,” *Phys. Rev.* **D66**, 054 017 (2002).
- [8] L. Clavelli, “Jet invariant mass in quantum chromodynamics,” *Phys. Lett.* **B85**, 111 (1979).
- [9] M. Kramer, S. Mrenna, and D. E. Soper, “Next-to-leading order QCD jet production with parton showers and hadronization,” *Phys. Rev.* **D73**, 014 022 (2006).
- [10] R. K. Ellis, W. J. Stirling, and B. R. Webber, *QCD and Collider Physics* (Cambridge University Press, Cambridge, UK, 1996).
- [11] G. Altarelli and G. Parisi, “Asymptotic Freedom in Parton Language,” *Nucl. Phys.* **B126**, 298 (1977).
- [12] J. D. Bjorken and S. D. Drell, *Relativistic Quantum Mechanics* (McGraw Hill, New York, USA, 1964).

- [13] Z. Nagy and D. E. Soper, “Parton showers with quantum interference,” *JHEP* **09**, 114 (2007).
- [14] D. E. Soper, “beowulf,” This code is available at <http://physics.uoregon.edu/~soper/beowulf/>.
- [15] C. P. Robert and G. Casella, *Monte Carlo Statistical Methods* (Springer-Verlag, New York, USA, 2004).
- [16] Y. L. Dokshitzer and B. R. Webber, “Calculation of power corrections to hadronic event shapes,” *Phys. Lett.* **B352**, 451–455 (1995).
- [17] G. Kramer and H. Spiesberger, “A new calculation of the NLO energy-energy correlation function,” *Z. Phys.* **C73**, 495–504 (1997).
- [18] G. Abbiendi et al., “Measurement of event shape distributions and moments in $e^+e^- \rightarrow j$ hadrons at 91-GeV - 209-GeV and a determination of $\alpha(s)$,” *Eur. Phys. J.* **C40**, 287–316 (2005).
- [19] P. A. Movilla Fernandez, O. Biebel, S. Bethke, S. Kluth, and P. Pfeifenschneider, “A study of event shapes and determinations of $\alpha(s)$ using data of e^+e^- annihilations at $s^{*(1/2)} = 22\text{-GeV}$ to 44-GeV ,” *Eur. Phys. J.* **C1**, 461–478 (1998).
- [20] P. A. Movilla Fernandez, O. Biebel, and S. Bethke, “Measurement of C-parameter and determinations of $\alpha(s)$ from C-parameter and jet broadening at PETRA energies,” (1998).
- [21] N. Arkani-Hamed, S. Dimopoulos, and G. R. Dvali, “The hierarchy problem and new dimensions at a millimeter,” *Phys. Lett.* **B429**, 263–272 (1998).
- [22] L. Randall and R. Sundrum, “A large mass hierarchy from a small extra dimension,” *Phys. Rev. Lett.* **83**, 3370–3373 (1999).
- [23] C. W. Misner, K. S. Thorne, and J. A. Wheeler, *Gravitation* (W. H. Freeman, San Francisco, CA, 1973).
- [24] R. Emparan, M. Masip, and R. Rattazzi, “Cosmic rays as probes of large extra dimensions and TeV gravity,” *Phys. Rev.* **D65**, 064023 (2002).
- [25] H. Yoshino and Y. Nambu, “Black hole formation in the grazing collision of high-energy particles,” *Phys. Rev.* **D67**, 024009 (2003).
- [26] P. D. D’Eath and P. N. Payne, “Gravitational radiation in high speed black hole collisions. 3. Results and conclusions,” *Phys. Rev.* **D46**, 694–701 (1992).

- [27] P. Meade and L. Randall, “Black Holes and Quantum Gravity at the LHC,” *JHEP* **05**, 003 (2008).
- [28] J. Preskill, P. Schwarz, A. D. Shapere, S. Trivedi, and F. Wilczek, “Limitations on the statistical description of black holes,” *Mod. Phys. Lett.* **A6**, 2353–2362 (1991).
- [29] L. A. Anchordoqui, J. L. Feng, H. Goldberg, and A. D. Shapere, “Inelastic black hole production and large extra dimensions,” *Phys. Lett.* **B594**, 363–367 (2004).
- [30] S. B. Giddings and S. D. Thomas, “High energy colliders as black hole factories: The end of short distance physics,” *Phys. Rev.* **D65**, 056 010 (2002).
- [31] R. C. Myers and M. J. Perry, “Black Holes in Higher Dimensional Space-Times,” *Ann. Phys.* **172**, 304 (1986).
- [32] R. Emparan, G. T. Horowitz, and R. C. Myers, “Black holes radiate mainly on the brane,” *Phys. Rev. Lett.* **85**, 499–502 (2000).
- [33] S. Dimopoulos and G. L. Landsberg, “Black Holes at the LHC,” *Phys. Rev. Lett.* **87**, 161 602 (2001).
- [34] D. M. Eardley and S. B. Giddings, “Classical black hole production in high-energy collisions,” *Phys. Rev.* **D66**, 044 011 (2002).
- [35] X. Calmet, S. D. H. Hsu, and D. Reeb, “Quantum gravity at a TeV and the renormalization of Newton’s constant,” *Phys. Rev.* **D77**, 125 015 (2008).
- [36] X. Calmet, W. Gong, and S. D. H. Hsu, “Colorful quantum black holes at the LHC,” *Phys. Lett.* **B668**, 20–23 (2008).
- [37] S. Weinberg, “Varieties of Baryon and Lepton Nonconservation,” *Phys. Rev.* **D22**, 1694 (1980).
- [38] G. Ossola, C. G. Papadopoulos, and R. Pittau, “Reducing full one-loop amplitudes to scalar integrals at the integrand level,” *Nucl. Phys.* **B763**, 147–169 (2007).
- [39] R. K. Ellis, W. T. Giele, and Z. Kunszt, “A Numerical Unitarity Formalism for Evaluating One-Loop Amplitudes,” *JHEP* **03**, 003 (2008).
- [40] C. F. Berger et al., “An Automated Implementation of On-Shell Methods for One- Loop Amplitudes,” *Phys. Rev.* **D78**, 036 003 (2008).
- [41] Z. Nagy and D. E. Soper, “Numerical integration of one-loop Feynman diagrams for N- photon amplitudes,” *Phys. Rev.* **D74**, 093 006 (2006).

- [42] W. Gong, Z. Nagy, and D. E. Soper, “Direct numerical integration of one-loop Feynman diagrams for N-photon amplitudes,” *Phys. Rev.* **D79**, 033 005 (2009).
- [43] Z. Nagy and D. E. Soper, “General subtraction method for numerical calculation of one-loop QCD matrix elements,” *JHEP* **09**, 055 (2003).
- [44] D. E. Soper, “Techniques for QCD calculations by numerical integration,” *Phys. Rev.* **D62**, 014 009 (2000).
- [45] D. E. Soper, “NPhoton,” This code is available at <http://physics.uoregon.edu/~soper/Nphoton/>.
- [46] G. Mahlon, “Use of recursion relations to compute one loop helicity amplitudes,” (1994).
- [47] T. Binoth, G. Heinrich, T. Gehrmann, and P. Mastrolia, “Six-Photon Amplitudes,” *Phys. Lett.* **B649**, 422–426 (2007).